AD-A253 689

PL-TR-92-2095

SEISMIC SURVEILLANCE - NUCLEAR TEST BAN VERIFICATION

Eystein S. Husebye
Bent O. Ruud

University of Oslo
Department of Geology
P.O. Box 1047 Blindern
N-0316 Oslo 3, NORWAY

27 March 1992

Final Report
1 January 1989-31 December 1991

92-18654
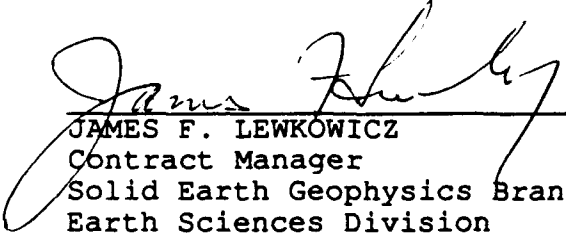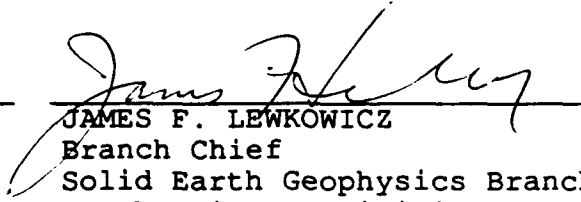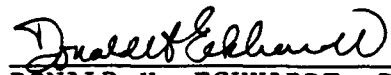
The views and conclusions contained in this document are those of the authors and should not be interpreted as representing the official policies, either expressed or implied, of the Defense Advanced Research Projects Agency or the U.S. Government.

This technical report has been reviewed and is approved for publication.

JAMES F. LEWKOWICZ
Contract Manager
Solid Earth Geophysics Branch
Earth Sciences Division

JAMES F. LEWKOWICZ
Branch Chief
Solid Earth Geophysics Branch
Earth Sciences Division

DONALD H. ECKHARDT, Director
Earth Sciences Division

This report has been reviewed by the ESD Public Affairs Office (PA) and is releasable to the National Technical Information Service (NTIS).

Qualified requestors may obtain additional copies from the Defense Technical Information Center. All others should apply to the National Technical Information Service.

If your address has changed, or if you wish to be removed from the mailing list, or if the addressee is no longer employed by your organization, please notify PL/IMA, Hanscom AFB, MA 01731-5000. This will assist us in maintaining a current mailing list.

Do not return copies of this report unless contractual obligations or notices on a specific document requires that it be returned.

REPORT DOCUMENTATION PAGE

1. AGENCY USE ONLY *(Leave blank)*	2. REPORT DATE 27 March 1992	3. REPORT TYPE AND DATES COVERED Final Report (1 Jan 1989–31 Dec 1991)

4. TITLE AND SUBTITLE
Seismic Surveillance - Nuclear Test Ban Verification

5. FUNDING NUMBERS
PE 61101E
PR 9A10   TA DA   WU AE
Contract AFOSR-89-0259

6. AUTHOR(S)
Eystein S. Husebye
Bent O. Ruud

7. PERFORMING ORGANIZATION NAME(S) AND ADDRESS(ES)
University of Oslo
Department of Geology
P.O. Box 1047 Blindern
N-0316 Oslo 3, Norway

8. PERFORMING ORGANIZATION REPORT NUMBER

9. SPONSORING/MONITORING AGENCY NAME(S) AND ADDRESS(ES)
Phillips Laboratory
Hanscom AFB, MA 01731-5000

Contract Manager: James Lewkowicz/GPEH

10. SPONSORING/MONITORING AGENCY REPORT NUMBER

PL-TR-92-2095

11. SUPPLEMENTARY NOTES

12a. DISTRIBUTION/AVAILABILITY STATEMENT

Approved for public release; distribution unlimited

12b. DISTRIBUTION CODE

13. ABSTRACT *(Maximum 200 words)* The project is aimed at seismic surveillance as part of on-going efforts for improving nuclear test ban verification capabilities. The problem is complex in the sense that underground explosions are most efficiently monitored by seismic means, but that the distinction between signals emitted by natural earthquakes and explosions remains unclear, at least at local and regional distances. In other words, seismic wave propagation in a heterogeneous Earth may easily mask specific source signatures.

In Section 2, we report on major results from a marine seismic reflection survey, in the Skagerrak Sea and the outer Oslo Fjord. The profiling area "covers" the Skagerrak Graben, the southward extension of the Oslo Rift in which vicinity both the NORSAR and NORESS arrays are located. Anyway, extensional simple shear deformation of the entire lithosphere has been postulated by Wernicke (1985) and others, but up to now unequivocal seismic evidence in support of this hypotheses has been lacking (Kusznir and Egan, 1989). Here we give evidence on well defined seismic reflectors in the recordings coda correlations seldom exceed 0.4 units. Since various kinds of homogeneous crust/lithosphere models seemingly are unable to account for
(OVER)

14. SUBJECT TERMS
Fault mapping in the crust/lithosphere; automatic seismic network bulletin; short-period Rg-observations; finite difference synthetics for inhomogeneous media; USSR event classification experiments

15. NUMBER OF PAGES
176

16. PRICE CODE

17. SECURITY CLASSIFICATION OF REPORT	18. SECURITY CLASSIFICATION OF THIS PAGE	19. SECURITY CLASSIFICATION OF ABSTRACT	20. LIMITATION OF ABSTRACT
Unclassified	Unclassified	Unclassified	SAR

prominent, observational coda features the crust/lithosphere system were described in terms of self-similar von Karman inhomogeneous media with correlation distance of 10 km and velocity perturbations of 2-4 per cent. Here, Moho undulations were represented as a 1D von Karman function. Synthetics computed for such kinds of inhomogeneous media quantitatively accounts for major coda features like relative high amplitudes, long duration and poor coherency beyond a sensor spacing of a few kilometres. Also, P-to-S or S-to-P conversions in the source vicinity are relative efficient for inhomogeneous media as compared to homogenous media. The other work presented in Section 4 deals with fundamental mode Rayleigh (Rg) wave propagation in the uppermost part of the crust. The observational data comprise recordings from 7 arrays located on 4 continents. The inversion of the individual phase velocity observations were considered for one layer and two layers models above halfspace. In the latter case, the layer thicknesses were fixed at 0.5 km and 1.0 km. Unknowns were layer and half space shear velocities and in case of Model 1 also layer thickness. The average of estimated halfspace velocities was 3.56 kms^{-1} and array differences were small here. Also the Model 1 layer shear velocity estimated were rather consistent between the various arrays and the average was 2.87 kms^{-1}. In contrast the Model 1 layer shear thicknesses varied considerably with extreme values of 0.12 km for Yellowknife and 1.6 km for Alice Springs. The two layer model gave a slightly poorer fit to the observations in comparison to the one layer model. In order to provide a better insight in Rg-propagation in an uppermost crust low velocity layer (LVL) of thickness 1.4 km we generated 2D FD synthetics both for homogenous and inhomogeneous media. In the former case, rather classical surface wave trains were produced including a prominent Airy phase at c. 1.1 sec. period. For the inhomogeneous media multiple scattering became pronounced with S-scattering wavelets interfering with the Rg-waves. Also, the Airy phase was considerably less distinct while Rg excitation was dramatively reduced for focal depths below 2-3 km.

Our first attempt on seismic discrimination between earthquakes and underground nuclear explosions is documented in Section 5. This problem is formulated as an exercise in pattern recognition approach analysis. An advantage of our procedure is flexibility, by combining both adaptive noise suppression and event classification incorporating feature selection criteria. The procedure has been applied to a learning set of 44 nuclear explosions (8 test sites) and 35 earthquakes in Eurasia recorded at the NORESS array. The signal features considered were the normalized power in 8 spectral bands in the 0.2-5.0 Hz range of the P-wave (6 sec) and the P-coda (30 sec). Physically, it means that we exploit potential differences in the shape of earthquake and explosion spectra, respectively. Other features included are peak P and P-coda amplitude frequencies and relative P/P-coda power. These 19 features were extracted either from conventional array beam traces or optimum group filtered traces (OGF-removal of coherent low-frequency noise). Using the feature selection algorithm, based on estimates of the expected probability of misclassification (EPMC), only 2 to 4 features were needed for optimum discrimination performance. The dominant features were coda excitation and P- and P-coda power at lower signal frequencies. Furthermore, feature parameters extracted from the OGF traces had a slightly better performance in comparison to those extracted from beam traces. Finally, there were no misclassifications for OGF-derived features when the explosions population was limited to E. Kazakh events, while including events from the other test sited lead to a decrease in discrimination power.

Skagerrak Sea which are interpreted as major low angle shear zones (The Bamble Fault - BF) also underlying the Skagerrak graben segment of the Oslo Rift. A few of them can be traced almost continuously from mid-crust through the lower crust, off-setting Moho and continuing downwards to 50-60 km depth (16 sTWT). This and similar results from 1730 km of deep seismic lines in the Skagerrak Sea indicated that the crust and mantle did inherit a pronounced structural fabric from the earlier Proterozoic Sveconorwegian orogeny. Reactivation of such weakness zones surfaced during the rifting may explain the occurrence of simple shear in the lower crust below Skagerrak.

In another study, based on the same R/V Mobil Search profiling records, we focused on mapping faults in the upper, presumed brittle part of the crust. The northeastern area of the Skagerrak Sea appeared most suitable for this undertaking because the sediment coverage here is very thin or absent. Close inspections of our high quality sections, reprosessed to full commercial exploration standard, gave strong evidence of seismic images of an abundance of moderately steep (20 - 40 deg) faults in the crystalline basement. The fault geometry could be inferred at profile intersections, and moreover was found to coincide with the general tectonic imprints observed on land and along the rim of the Skagerrak Graben. Fault interspacing was ca. 3-5 km and depth penetration 10-15 km.

In a seismic surveillance context, the above results are considered important on two accounts; firstly an extensively cracked crust is likely to generate considerably amount of shear wave energy even for simple P-type explosive sources. Observational evidence stem from quarry blast recordings where often the largest signal amplitude is found on the transverse component. This is attempted synthesized by putting P-sources in inhomogeneous media (Section 4). Secondly, earthquake occurrence is often related to faults and lineaments derived from satellite images of the Earth surface. This could be a dubious undertaking in view of an epicenter determination accuracy seldom better than 5-10 km and that projection of "surface" faults deep into the crust is not well constrained as demonstrated for the Skagerrak Sea.

In previous work under this contract we have presented novel schemes for epicenter locations and signal detections using 3-component observations. In section 3 an experiment is described by which we use the detector described in Ruud and Husebye (1992) for automatically picking P- and S-arrivals in local event records stemming from the Norwegian Seismic Network. For automatic epicenter determination a robust grid-search method well suited for estimation problems with non-Gaussian observational errors is introduced in order to handle outliers. Even several large arrival time outliers did not prevent solutions close to the "true" epicenter. In our experiment, 38 local events from the August 1991 bulletin were located. The number of detecting stations varied from 3 to 10 out of a total of 15 stations. P- and S-picking errors were small, mostly within 0.5 sec for both P and S. Phase identification errors, causing severely wrong P- and S-arrivals were more frequent. Decent epicenter determinations were obtained even for events with 30-50 per cent outliers. The RMS location difference of our "automatic" solutions compared to those in the manually produced bulletin were about +/- 15 km.

In Section 4 we present two works addressing the problem of seismic wave propagation in inhomogeneous media. Firstly, details are given on the methodology used for computing synthetic seismograms from 2D finite difference (FD) solutions of the elastic wave equation. The principal aim of this study was to explore the range of crust/lithosphere structural models which were capable of producing strong and persistent coda waves commonly observed at local and regional distances. The starting model was homogenous but included a Moho bump like that associated with the Oslo Rift in the vicinity of the NORESS siting area. The corresponding synthetics were similar to those obtainable using ray tracing methods or in other words no significant coda waves were generated. Introducing crustal velocity gradients in the crust neither contributed much to the synthetic record complexity. In contrast, a model with a sinusoidal shaped Moho (λ = 8 km, Amp = 1 km) produced an abundance of multiple reflected and scatlered P- and S-phases giving the appearance of strong and persistent P- and S-wave codas. The corresponding coda correlations over a line array length of 5-10 km were rather high (around 0.5 - 0.7 units) while for real

CONTENTS

FINAL REPORT

1 Jan 1989 - 31 Dec 1991

ARPA Order:	# 5299, Amendment 18
Program Code:	
Name of Grantee:	University of Oslo, Norway
Effective Date of Contract:	01 Jan 1989
Contract Expiration Date:	31 Dec 1991
Grant Number:	AFOSR-89-0259
Principal Investigators:	Eystein S. Husebye 47-6-817121 Bent O. Ruud 47-2-856615
Program Manager:	James F. Lewkowicz (617) 861-3028
Short Title of Work:	Seismic Surveillance - Nuclear Test Ban Verification

University of Oslo
Department of Geology
P.O. Box 1047, Blindern
N-0316 Oslo 3
Norway

List of publications supported by this contract

This contract covers a 3 year period so the publications are listed in annual order.

Papers included in Scientific Report #1 (1990):

1. Bannister, S.C., Husebye, E.S., and Ruud, B.O. (1990). Teleseimic P-coda analyzed by three-component and array techniques — deterministic location of topographic P-to-Rg scattering near the NORESS array. *Bull. Seism. Soc. Am.*, **80**, 1969-1986.

2. Bannister, S.C., Ruud, B.O., and Husebye, E.S. (1991). Tomographic estimates of sub-Moho seismic velocities in Fennoscandia and structural implications, *Tectonophysics*, **189**, 37-53.

3. Cassidy, F., Christoffersson, A., Husebye, E.S., and Ruud, B.O. (1990). Robust and reliable techniques for epicentre locations using time and slowness observations, *Bull. Seism. Soc. Am.*, **80**, 140-149.

4. Kinck, J.J., Husebye, E.S., and Lund, C.-E. (1991). The South Scantinavian crust: Structural complexities from seismic reflection and refraction profiling, *Tectonophysics*, **189**, 117-134.

5. Ruud, B.O. (1990). Teleseismic epicentre locations from arrival times at regional networks, *Geophys, J. Int.*, **100**, 515-519.

6. Ruud, B.O., and Husebye, E.S. (1991). Exploring the upper crystalline crust: A combined interpretation of 3D imaging and reflection profiling in the NORESS array, *Tectonophysics*, **189**, 109-115.

Papers included in Scientific Report #2 (1991):

7. Kinck, J.J., Husebye, E.S., and Larsson, F.R. (1991). The Moho Depth Distribution in Fennoscandia and the Regional Tectonic Evolution from Archean to Permian Times, *Lithos*, in press.

8. Lokshtanov, D.E., Ruud, B.O., and Husebye, E.S. (1991). The crustal transfer function in seismic 3-component slowness estimation, *Geophys. Res. Lett.*, **18**, 1343-1396.

9. Lokshtanov, D.E., Ruud, B.O., and Husebye, E.S. (1991). The upper crust low velocity layer; a Rayleigh (Rg) phase velocity study from SE Norway, *Terra Nova*, **3**, 49-56.

10. Ruud, B.O., and Husebye, E.S. (1992). A new three-component detector and automatic single station bulletin production, *Bull. Seism. Soc. Am.*, **82**, 221-237.

Papers included in Scientific Report #3 (1992, this report):

11. Tsvang, S.L., Pinsky, V.I., and Husebye, E.S. (1992). Enhanced seismic source discrimination using NORESS array recordings from Eurasian events, *Geophys. J. Int*, in press.

12. Lie, J.E., and Husebye, E.S. (1992). Seismic imaging of upper crustal basement faults in the Skagerrak Sea, *Tectonophysics*, in press.

13. Lie, J.E., and Husebye, E.S. (1992). Simple shear deformation of the Skagerrak lithosphere: implications for the Oslo Rift formation, m/s submitted for publication.

14. Ruud, B.O., Lindholm, C.L., and Husebye, E.S. (1992). An exercise in automatic seimic record analysis and network bulletin production, m/s submitted for publication.

15. Ruud, B.O., Husebys, E.S., and Hestholm, S.O. (1992). On crustal, short period Rg-propagation using array records from 4 continents, m/s in preparation.

16. Hestholm, S.O., Ruud, B.O., Husebye, E.S., and Rosland, B.O. (1992). Synthesizing 2D wave propagation in a heterogeneous lithosphere using finite difference techniques, m/s in preparation.

Report summary

Task objectives:

- Very detailed crust/lithosphere mapping by seismic profiling means

- Automatic analysis of seismograph network data and bulletin production

- Seismic wave propagation in the lithosphere using 2D finite difference solutions of the elastic wave equation

- Enhanced seismic source discrimination at teleseismic distances using NORESS array data

Technical and Scientific Problems

In 1987 one of us (E.S. Husebye) had at his disposal the seismic ship R/V Mobil Search (Courtesy of Mobil Exploration Inc (Norway)) for 30 days of profiling in the Skagerrak Sea. The profiling area includes the southern extension of the Oslo Rift in which vicinity the NORESS array is located. Use of the seismic reflection data (totalling 1730 km) have enabled us to image crust and lithosphere structures in exceptional detail, including Moho disruptions. Likewise, a large number of minor and major faults have been mapped both within the crystalline crust and also in the sub-Moho part of the lithosphere. Two of the report works deal with this kind of seismic mapping.

In previous reports we have addressed problems related to more efficient signal detection and also robust techniques for epicenter locations. This kind of methods are essential for automating seismograph network operations including that of bulletin production without analyst interference. In this report we demonstrated that the latter problem is solvable in practise using observational data from the Norwegian Seismograph Network.

The nature of seismic wave propagation at local and regional distances are important for the optimum design of seismic source classification criteria. In this context, we have explored the usefulness of 2D finite difference solutions of the elastic wave equation in combination with varying degrees of structural complexities in the crust and lithosphere. The major problem is to generate synthetics which at least approximately match typical observational features like strong coda waves of extended duration. In this respect, self-similar scattering media of von Karman type proved far more efficient for coda generation that classical stratified media. In a Rg-study, based on recordings from 7 arrays on 4 continents, we also used synthetics for gaining a better insight in Rg-propagation in complex media.

The major challenge in seismic surveillance in the context of a potential test ban treaty, is that of classifying events as either an earthquake or man-made explosion. This kind of problems were formulated as an exercise in pattern recognition approach analysis. Using NORESS array recordings of teleseismic Eurasian events, our analysis procedure combined both adaptive noise suppression and event classification incorporating feature selection criteria. The signal features considered were the normalized power in 8 spectral bands in the 0.2 - 5.0 Hz range of the P-wave (6 sec duration) and the subsequent P-coda (30 sec duration). Additional features were peak P and P-coda amplitude frequencies and relative P/P-coda power. Out of these 19 features only a subset of 2-4 features were needed for optimum discrimination performance when tested on 44 presumed nuclear explosions and 35 presumed earthquakes.

Methodology used in the seismic data analysis

The seismic profiling data used in crustal structure imaging were processed using commercial "oil prospecting" software. The final, refined data processing were performed at BIRPS, Cambridge Univ., UK which expertise in the particular field of signal processing is recognized world-wide. Regarding automatic network operation, a novel, robust "grid search" epicenter location scheme has been introduced. It has been tested on local network data, and provided decent location estimates even in cases of up to 40 per cent gross errors in the input parameters like P- and S-arrival 'mes and/or azimuth.

x

Regarding our synthetics seismogram analysis, 2D finite difference techniques were used by geophysicists more than two decades ago. However, a unique feature of our approach is that the model sizes used enable us to simulate real recording at local distances (out to 3-400 km). The event classification techniques used, albeit reflecting a pattern recognition approach, proved to be both flexible and powerful due to the incorporation of feature selection criteria.

Major Scientific Results

In Section 2 works bearing on imaging (1-3 km resolution) of crust/lithosphere structures are presented. We were here able to map many faults in the upper, brittle crust with dip angles in the range 20-40 deg., depth extent 10-15 km and (horizontal) spacing of 3-5 km. The most spectacular finding was the socalled Bamble Fault which could be traced through the brittle crust, continuing into the presumed lower ductile crust, off-setting Moho and continuing further down to 50-60 km depth (16 sTWT). Note, seemingly only seismic reflection profiling can provide such detailed structural image, definitely not using other geophysical means nor from geological mapping. Clearly, an explosive source in a "cracked" upper crust would generate a considerable amount of shear waves thus quantitatively explaining the observational fact that for this type of sources the strongest signals are often found on the transverse component.

A long standing goal in the seismological community is that of automating seismograph network operation. This problem, dealt with in Section 3, has become more acute in recent years simply because modern, highly sensitive seismometers record daily a very large number of man-made local explosions. Our novel weighted "grid-search" epicenter location schemes was tested on Norwegian Seismograph Network (NSN) recording for Aug. 1991. The input parameters here, P- and S-arrival times and occasionally P-azimuth were extracted from records using the Ruud and Husebye (BSSA 1992) detector. The location scheme proved robust enough to handle partly faulty input parameters. The most common detector errors were associated with faulty phase identifications; for example by missing a weak, first arriving P-phase the subsequent and often strong S-phase would be denoted P. Phase picking as such appeared to be accurate: +/- 0.5 sec and +/- 1.0 sec for P- and S-phases respectively. A detail comparison with analyst epicenter solutions (HYPO 71) for 38 events, gave that the average difference in epicenter coordinates were 2 km (lat, long) with a std. deviation of 15 km. Important, with this kind of epicenter accuracy is would be easy to introduce advanced signal processing schemes in the post-detection state simply because potential phase arrivals like Pn, Pg, PmP, pP, Sn, Sg, SmS etc can be accurately predicted within time frames of at most a few seconds.

In Section 4 two work bearing on synthesizing crust/lithosphere seismic wave propagation are described. A basic problem is strong P- and S-codas, a typical observational feature at local distances, are not reproducible using conventional stratified crust/lithosphere models. For our synthetics calculations we have used 2D finite difference technique which can handle very complex structures. In the latter case we have experimented with self-similar von Karman media, an uppermost crust low-velocity layer and a corrugated (1D von Karman representation) Moho boundary. Major results here is that a "scatter" medium with RMS velocity variations of c. 3-6 per cent are essential for strong coda generation. Corrugations on major discontinuities are important in this context. When a P-source is embedded in a complex medium, P-to-S conversion close to the source is efficient. This explains why we see so much shear wave energy in local quarry blast records.

Rg-synthetics for propagation in the uppermost crust low velocity layer (LVL) are instructive for a better understanding of the observational recordings. For example, for focal depths below 2-3 km handly any Rg-waves would be excited. Thus Rg-observations could be an important discriminant for source classification. However, introducing scatters in the LVL tend to attenuate the Rg besides generating an abundance of interfering s-scattering wavelets. In this way we can quantitatively explain the relative elusivness of Rg-phases at least for stations located in hilly areas. The Rg-observations used in analysis comes from 7 arrays on 4 continents, and the estimated LVL shear velocity and half-space velocity estimates were remarkedly consistent despite the large separations between siting areas. Average velocities were 2.87 kms^{-1} amd 3.56 kms^{-1} respectively. For the one layer over halfspace model used in inversion of the dispersion observations the LVL layer thickness varied considerably from 0.12 km at Yellowknife (Canada) to 1.60 km at Alice Springs (Australia).

In section 5, we address the problem of event classification in the teleseismic distance range and using P-and P-coda observations only. Using our novel discriminant technique we were able to successfully (no misclassifications) classify all presumed nuclear tests in the E. Kazakh area. However, including presumed explosions from many other parts of exUSSR in the learning set, a slight increase of 6.5 per cent in the classifications error was observed. This imply that for teleseismic events (read explosions) upper mantle

propagation paths do not much weaken a source discriminant. However, for events with Mb-values below 4.0 to 4.5 the events become explosion-like simply due to poor SNR for the coda waves. Since we used NORESS observations which detectability is excellent for Eurasia we take the above results to imply that Mb 4.0 - 4.5 represent lower limits for teleseismic event classification capabilities.

Concluding Remarks

During the contracting period we had observed problems related to:
- Structural mapping of the crust/lithosphere
- Signal detection, event location and automating the seismic bulletin production
- Wave propagation in complex media for realistically synthesizing wave propagation in the crust/lithosphere system.
- Extensive experiments with event classification at teleseismic distances have also been undertaken.

Extensive documentation of our research efforts under said research contract, are presented in the 3 mandatary annual science reports (including this one). Complementary purely scientific presentations are in form of 16 publications listed on page 2 in this report.

Implications for Further Research

The need for a better understanding of crust/lithosphere wave propagation complexities is essential for the design of flexible event discriminants for use at local and regional distance ranges. Also important is automating seismograph network operation so available resources can be focused upon a few relative problematic events instead of wasted on numerous man-made explosions in un-interesting areas.

SIMPLE SHEAR DEFORMATION OF THE SKAGERRAK LITHOSPHERE; IMPLICATIONS FOR THE OSLO RIFT FORMATION

J.E. Lie

Department of Geology, University of Oslo, Norway

E.S. Husebye

NTNF/NORSAR, Kjeller, Norway

1

Extensional simple shear deformation of the entire lithosphere has been postulated by Wernicke (1) and others but up to now unequivocal seismic evidence in support of this hypotheses has been lacking (2). Here we report on well defined seismic reflectors in the Skagerrak Sea which are interpreted as major low angle shear zones (The Bamble Fault - BF) also underlying the Skagerrak graben segment of the Oslo Rift. A few of them can be traced almost continuously from mid-crust through the lower crust, off-setting Moho and continuing downwards to 50-60 km depth (16 sTWT). This and similar results from 1730 km of deep seismic lines in Skagerrak indicate that the crust and mantle did inherit a pronounced structural fabric from the earlier Proterozoic Sveconorwegian orogeny. Reactivation of these surfaces during the rifting may explain the occurence of simple shear in the lower crust below Skagerrak. Conventional rifting scenarios incorporating magmatic underplating of Moho is not considered tenable in our reconstruction of the Oslo Rift formation.

The Permian Oslo Rift is centrally located in the Sveconorwegian province of the Baltic Shield (3,4)(Fig. 1). The tectonic fabric of the crust appears to reflect alternating E-W compressional and extensional regimes with the Grenvillian-Sveconorwegian orogeny (1.2-0.9 Ga) as the most prominent one (5). For example, the Skagerrak Sea block appears to have been upthrusted and ductily sheared against the cratonized Telemark block to the west during this orogeny (6,7) (Fig. 1). The development of the much later Oslo Rift remains a puzzle despite much "on land" geological research effort (3,8). We have been able to adress this old problem with new seismic reflection data stemming from the R/V Mobile search cruise in Skagerrak in 1987 (9, Fig 1). The entire deep seismic grid (16 s TWT) has

recently been reprocessed using the computer facilities at Bullard Labs, Cambridge, UK which greatly improved the resolution of the seismic sections.

The lines having the most direct baring on the rift area are displayed in Fig.2. The sharp reflector in Fig. 2a is outstanding, cutting through the entire crust, offsetting Moho 2-4 km and continuing in the upper mantle. It is clearly seen on both OG-8 and OG-12. This reflector is observable for over 130 km and is intact below the Skagerrak rift segment. We denote this reflector the Bamble Fault (BF). Its landward extrapolation coincides with the PKF-fault separating the Telemark block and Bamble sector in Fig. 1 and 2b. On all N. Skagerrak profiles a prominent reflective feature can be observed originating in the lower crust and dipping into the mantle (Fig 2) . It is underlying the Skagerrak Graben, has a highly reflective character and its upper `surface` in the mantle is mapped out in Fig. 3a. We interpreted it as the remains of the underthrusted crustal segment of the Telemark craton. It is clearly shown on both intersecting profiles OG-8 and OG-2 (Fig. 2b,c). The structural style of this segment is similar to the crust/mantle imbrications that are observed below young orogenic zones like the Pyrenees and the Alps (10). The Moho disruption in the southwest on profile OG-2 (Fig. 2c), coincides with the Fjerritslev fault zone (FFZ; Fig. 1).

Pronounced crustal thinning coincides with the Oslo Rift axis except in the south where the Skagerrak graben axis is shifted slightly westward (Fig. 3b).

Dextral movements (ca. 3 km) are reported along the PKF-fault, bounding the Bamble sector, part of which took place in Permian times (4). Palaeozoic sediments have been reported in the entire Oslo Rift (11), presumed deposited in an older pre-rift basin. Outside the Skagerrak Graben only post-rift sedimentary strata are found (Fig. 3c). In our tectonic scenario the Skagerrak block was, during the Sveocnorwegian orogeny, fragmented with eastward parts being slightly overthrusted the westward ones (Fig. 2b). this is similar to the observations of the crustal shortening along the contemporary Grenvillian front in eastern Canada

(12,13).

In summary, the general Oslo Rift area was in Precambrian times subject to both compressional and extensional deformations thus weakening the lithosphere. The observed thinned crust of this area (Fig 3a) cannot alone be ascribed to the moderate Permian extension. Dyke and granite intrusions of 1000 Ma and younger in the Skagerrak coastal areas (8,14) also imply a lithosphere weakening.

During the early Permian extension the landward and seaward parts of the Oslo Rift apparently responded very differently. According to the numerical extension models of Dunbar and Sawyer (15) the continental lithosphere is analogue to a composite material of alternating high- and low-strength layers. A weak lower crust would act as a detachment zone relatively to a strong upper crust and a strong upper lithosphere. For a region being subjected to extensional forces , initial rifting would be located in areas having pre-existing weaknesses. In the northern onshore segment of the Oslo Rift vertical faulting dominated, cracking the weakened lithosphere with subsequent influx of basaltic magmas in the initial stages of 10-20 Ma (3,8). Stretching was very modest (ß approx. 1.1) and no pre-rift dooming (16). In the N.Skagerrak simple shear deformation apears to have taken place along the Bamble Fault (Fig.2b) and with the crust / lithosphere acting as a uniform block. Extensional reactivation of old Sveconorwegian compressional shear zones in the upper and lower crust would explain the favoured motion along a localized faultplane through the lower crust (15). The lower crust is otherwise by rheological and temperature considerations presumed to deform by distributed plastic stretching and thus not to accomodate simple shear deformation. The survival of the Precambrian "Telemark" underthrust beneath the Skagerrak Graben is taken in support of this view. Further south deformations may have taken place by pure shear along detachment zones in the lower crust and also in the lower lithosphere (2,17). For deep detachment zones in the lowermost crust, the corresponding crustal thinning would be small and shifted relative to the graben

axis as actually observed (Fig 3b,c). Likewise, geometry of the post rift sedimentary basin is also observed to be shifted (Fig. 3c). Our Oslo Rift models are cartoonized in Fig. 4.

Dominance of simple shear deformation would give rise to rotation, for which there, as mentioned, is evidence along the Bamble sector (Fig. 3b). The Skagerrak block is detached along the FFZ (18) (Fig.1 and 2c) where Permian magmatic activity has been reported (29,20). Finally, substantial parts of the lithosphere cannot have been distorted too much as deep reflectors down to around 100 km were reported for the OG-13 line in Fig.1 (21).

We have outlined the major trends in the Oslo Rift formation while on a smaller scale length secondary deformation features in Skagerrak have also been reported (22). We find no evidence of Moho magmatic underplating in Skagerrak a phenomenon often postulated for rift zones. The outstanding observational features are the tracing of the BF down to at least 60 km and the remains of the underthrusted Telemark craton beneath the graben. We conclude that our observations strongly indicate that simple shear deformation of the lithosphere occured below the N. Skagerrak and that the mode of lithosphere deformation is influenced by pre-existing structural fabric.

REFERENCES

1) Wernicke, B., Can. J. of Earth Sci., 22, 108-125, (1985).

2) Kusznir, N.J. & Egan, S.S. in Extensional tectonics and Stratigraphy of the North Atlantic Margins, (Eds: A.J. Tankard & H.R. Balkwill). AAPG Memoir 46, 305-322 (1989)

3) Ramberg, I.B. and Speldnes, N. in Tectonics and Geophysics of continental Rifts (eds Ramberg, I.B. and Neumann, E.R.). Nato ASI Series C, 37, Reidel, Dordrechts, Holland, 167-194, (1978).

4) Brøgger, W.C. Skr. Vitnsk. Selsk., I Mat.-Naturv., 6: pp 377, Christiania, Norway (1889)

5) Gaal, G. and Gorbatchev, R. Precambrian Res., 35, 15-52, (1987).

6) Falkum, T. in The deep Proterozoic Crust in the North Atlantic Provinces, (eds Tobi, A.C. and Touret, J.L.R.), Nato ASI Series 158, D.Reidel Pub. co.,309-322, (1985).

7) Starmer, I. C. in The deep Proterozoic Crust in the North Atlantic Provinces, (eds Tobi, A.C. and Touret, J.L.R.), Nato ASI Series 158, D.Reidel Pub. co.,269-290, (1985).

8) Bjørlykke,A., Ihlen, P.M., and Olsrud, S., Tectonophysics, 178, 109-126 (1990).

9) Husebye, E.S., E.S. , Ro, H.E., Kinck, J.J., and Larsson, F.R. Nor. geol. unders., Special Publ. 3, 14-20, (1988).

10) Bois, C. Geophys. J. Int. , 105, 55-69 (1991).

11) Bjørlykke, K., Nor. geol. unders., No. 380, 159-172 , (1983).

12) Rivers, T., et al., Tectonics, 8, 63-84 (1989)

13) Green, A.G. et al. Geology, 16, 788-792 (1988).

14) Kinck, J.J., Husebye, E.S. and Lund, C.E. Tectonophysics, 189, 117-133, (1991).

15) Dunbar, J. A. & Sawyer, D.S. J. of Geophs. Res., 94, 7278- 7292, (1990)

16) Wessel, P. and Husebye, E.S., Tectonophysics, 157; 39-58 (1987).

17) White, R.S. and McKenzie. D.P., J. Geophys. Res., 94, 7695- 7729 (1989).

18) Klemperer, S,L, and Huric, C.A., in Tectonic evilution of the
     North Sea Rifts (eds Blundell, D.J. and Gibbs, A.), Oxford   University
     Press 37-59 (1990).

19) Åm, K., Nor. Geol. Undrs., 287, 1-25 (1973).

20) Mikaelsen, O. and Nielsen, L.H., D.G.U Series A, No. 29, 37pp,
     (1991).

21) Lie, J. E., Pedersen, T. and Husebye, E.S. Nature, 346, 165-168,
     (1990).

22) Lie, J.E. and Husebye, E.S. Tectonophysics In press. (1992).
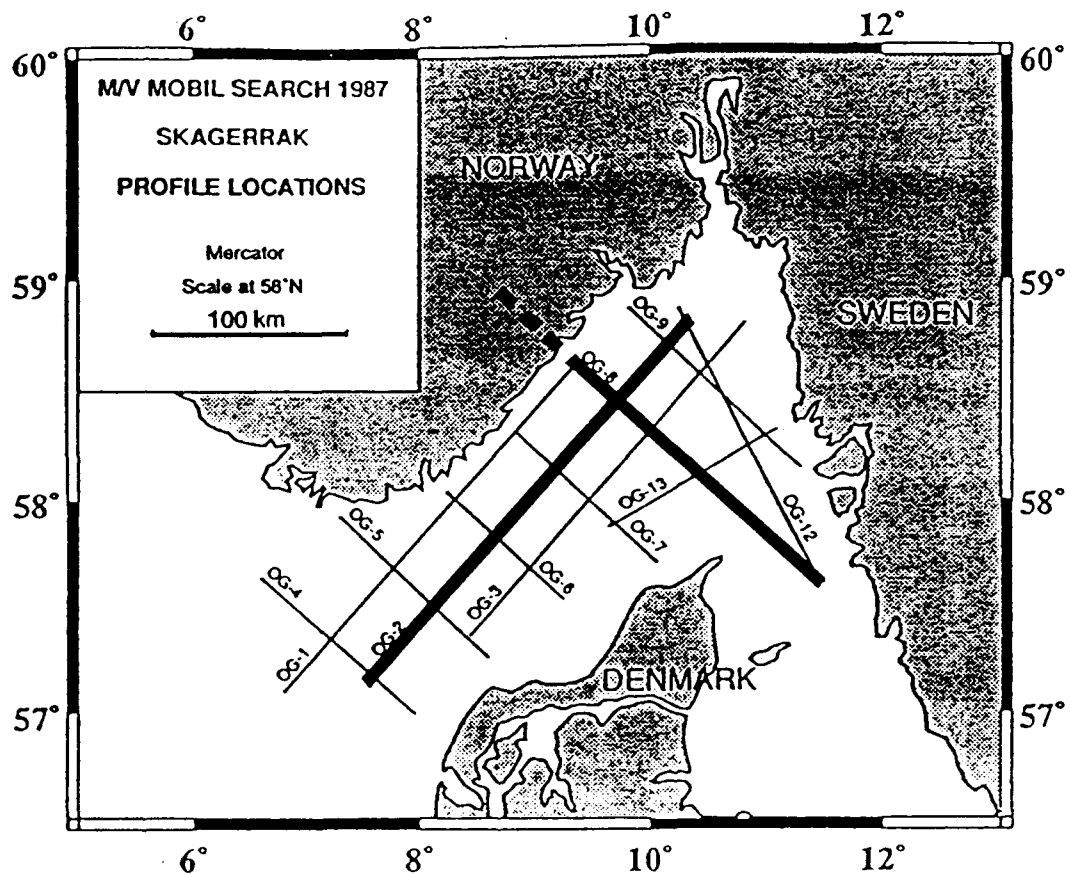
Fig 1a. Profiling grid - R/V Mobil Search cruise in Skagerrak, 1987. Aquisition parameters:7000 cu inch airgun array, 50 m shotpoint interval, 4500 m long streamer with 50 m group spacing and 4 ms samplerate.
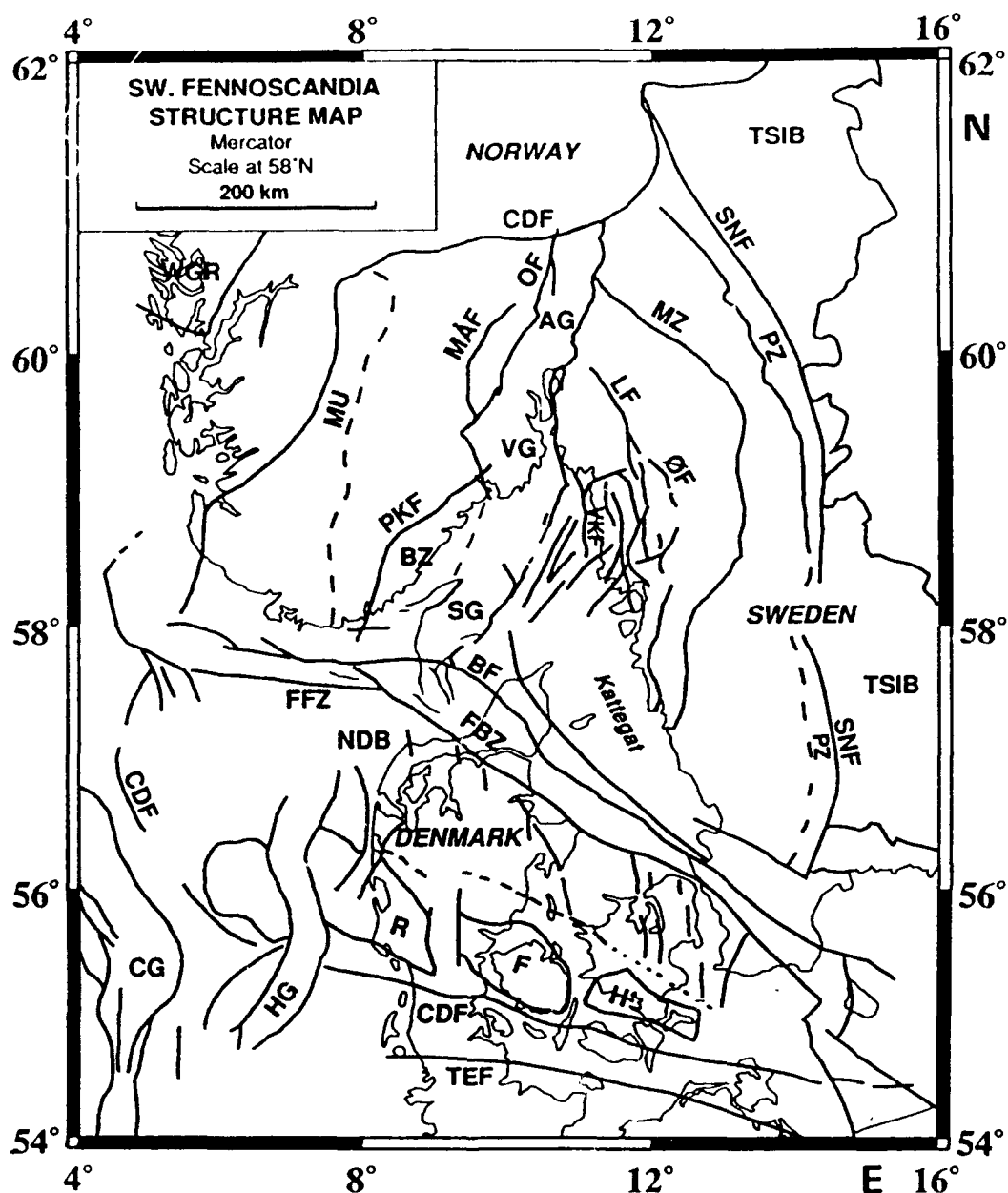
Fig 1b Tectonic map of the southwestern part of the Baltic Shield based on works of Gaal and Gorbatschev (5)and Kinck et al (14). AG: Akershus Graben, BF: Børgum Fault, BZ: Bamble Zone, CDF: Caledonian Deformation Front, FBZ: Fennoscandian Border Zone, FFZ: Fierritslev Fault Zone, LF: Løten Fault Zone, MZ: Mylonite Zone, MÅF: Meheia-Ådal Fault Zone, NDB: Norwegian-Danish Basin, OF: Oppland Fault Zone, PKF: Porsgrunn-Kristiansand Fault Zone,PZ: Protogine Zone, SG: Skagerrak Graben, SNF: Sveconorwegian Front, TSIB: Trans-Scandinavian Ignious Belt, VG: Vestfold Graben, WGR: Western Gneis Region, ØF: Øymark Fault.

10

Fig 2
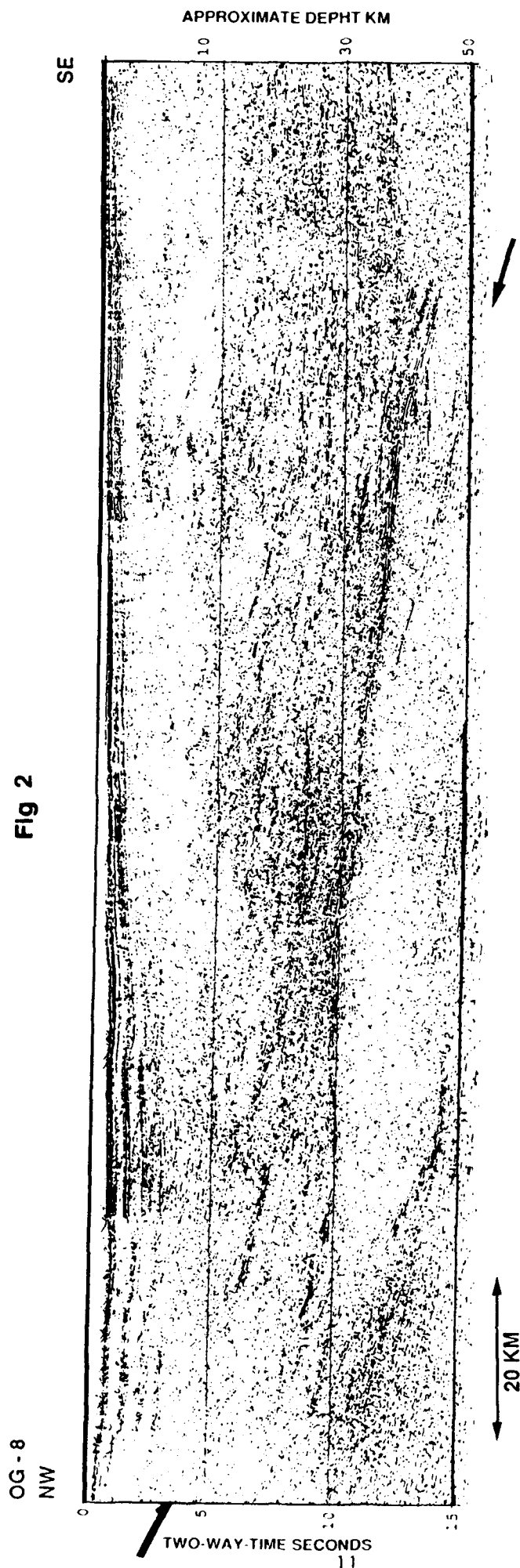
2a) Migrated section of profile OG-8 (Fig 1a). Notice the narrow reflective lineament, marked with an arrow, dipping through the crust and mantle from NW (6 s TWT) to SE (16 sTWT) on the section. The Skagerrak graben is partly masked by strong water bottom multiples, but is clearly identified on the gravity profile.

Fig 2
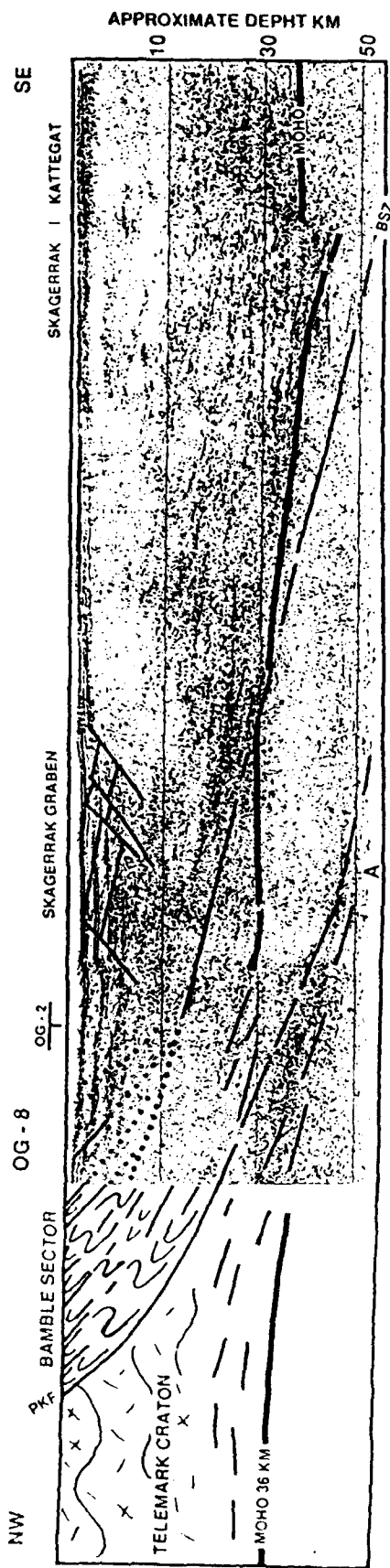
2b) Interpretation of profile OG-8 (Fig2a) related to the onshore geology of SE Norway (Fig.1). The onshore Bamble Sector is a high grade metamorphic terrain which is interpreted to have been ductily sheared and upthrusted against the Telemark Craton during the Sveconorwegian orogenesis (6,7). The east dipping mantle feature (A) is interpreted to be remains of a underthrusted crustal segment of the Telemark craton. BF marks the interpreted low angle Bamble fault, cutting the crust and mantle.
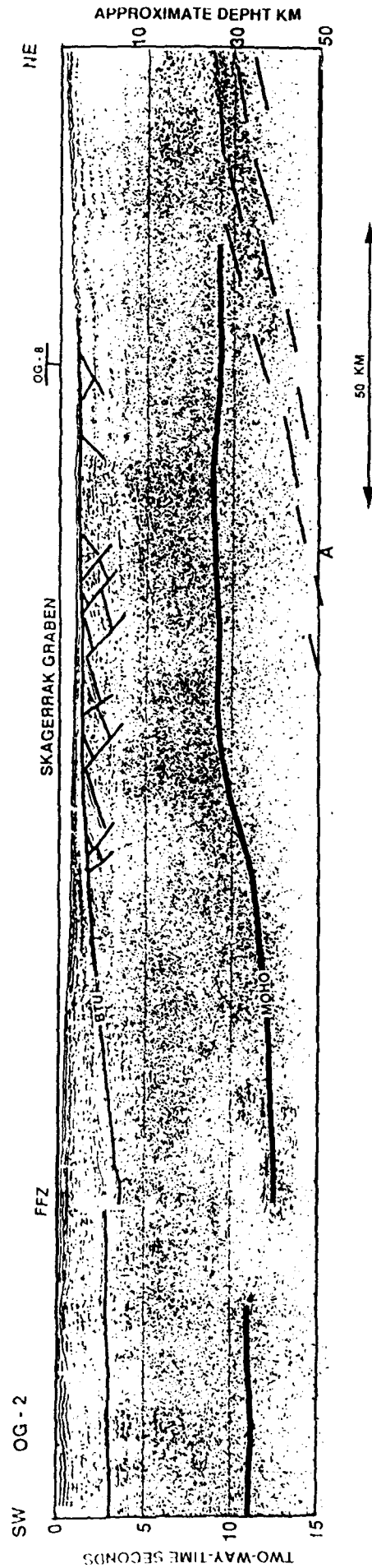
2c) Interpreted migrated section of profile OG-2 (Fig 1). Note the 4-5 km offset in Moho directly below the Fjerritslev Fault Zone (FFZ) indicating vertical faulting cutting the entire crust. Base Triassic unconformity (BTU), Skagerrak graben and Moho is marked. In the notheast the underthrusted segment of the Telemark craton is marked with (A), as on Fig 2 a,b.

Fig 3
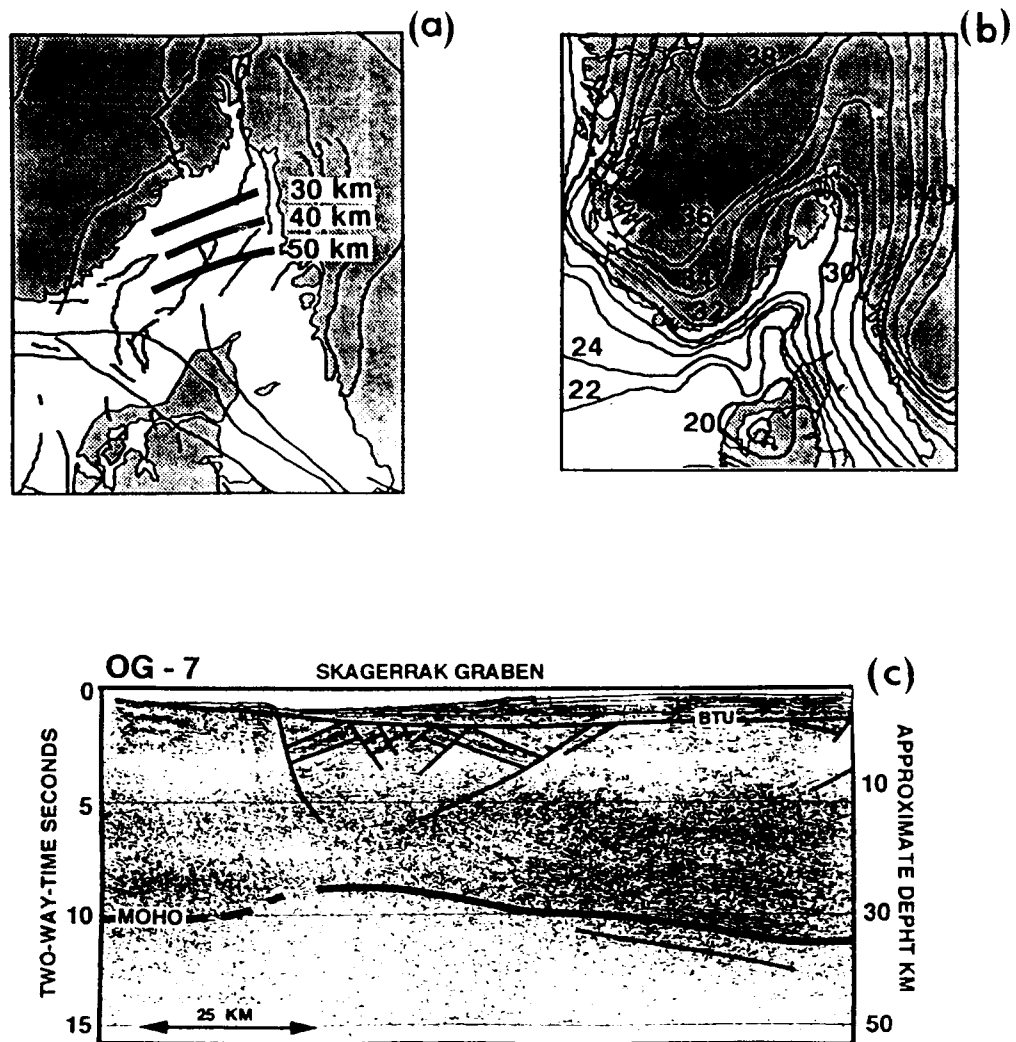
3a) Contours of the upper surface of the underthrusted segment of the "Telemark Craton" in the mantle shown in Fig. 2 marked (A).

3b) Thickness of crystalline crust in Scandinavia (6). Contour interval 2 km, the Skagerrak Graben contours are indicated.

3d) Interpreted migrated section of line OG-7; note that the post-rift sediments are here shifted eastward relative to the graben axis.

| Northern rift segment, landward | Central rift segment, N. Skagerrak | Southern rift segment, S. Skagerrak |
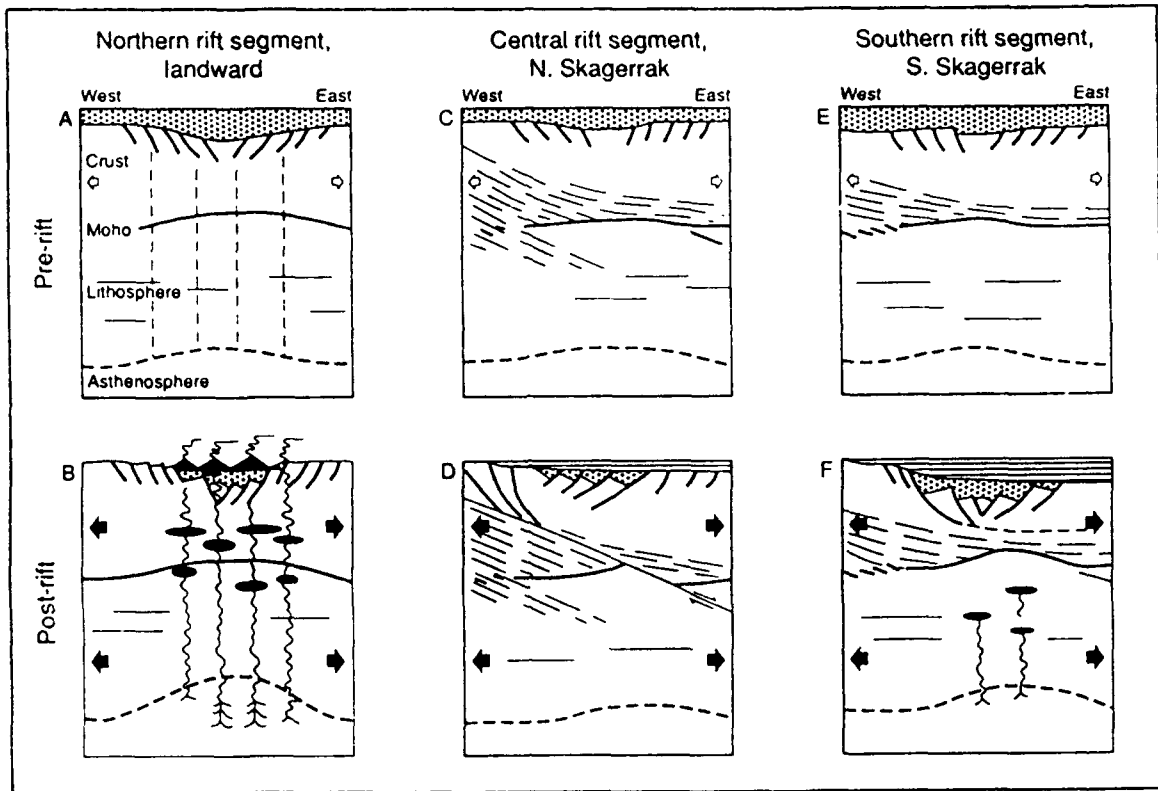
Fig 4 Schematic view of the Oslo Rift evolution for its northern, central and southern graben segments. Dimensions not to scale. The upper figures reflect the pre-rift stages and the lower reflect the post rift stages. Shading indicate upper/lower crust and likewise for the mantle lithosphere.

Northern segment, (Fig 4 a): Paleozoic pre-rift sedimentary basin implying thinned crust and weakened lithosphere. (Fig 4b): Rifting with graben formation and extensive magmatism. Moderate stretching. Pre-rift sediments only preserved within the graben due to base Tertiary erosion. Central segment, (Fig 4c) The pre-rift crustal fabric dominated by the Sveconorwegian crustal shortening. (Fig 4d) Simple shear deformation of the entire lithosphere. No magmatism observed, less dominant graben formation. Post-rift sedimentation and maximal crustal thinning slightly shifted to the east. Southern segment, (Fig 4e) Weakened Precambrian crustal imprint relative to the central segment (Fig 2 a,b) observed. (Fig 4f) Deformation by pure shear in the lower crust with detachment slightly offset to the east, explaining asymmetry between graben axis and general crustal thinning and post-rift sedimentation. Well developed graben formation with no clear indications of magmatism. Magmatism is however reported further to the south along the FFZ (Fig.1 and Fig 2c).

14

SEISMIC IMAGING OF UPPER CRUSTAL BASEMENT FAULTS IN THE SKAGERRAK SEA

J.E. Lie

Department of Geology, Oslo University, Norway

E.S. Husebye

NTNF/NORSAR, Kjeller, Norway

15

Abstract

In general, the continental upper crystalline crust appears almost nonreflective on many deep seismic reflection profiling sections. Only major faults and lithological boundaries can be localised, while smaller scale faults are usually not identified. A deep seismic survey covering the Skagerrak sea was undertaken in 1987 by the R/V Mobil Search - depth range 0 -16 s TWT. Although the north-eastern part of the Skagerrak has only thin or no sediment coverage, the data in the depth range 0 - 6 s TWT were still reprocessed to commercial exploration standard. Close inspection of these high quality sections provides evidence of seismic images of an abundance of moderately steep (20-50 deg) faults that can be traced to depths of 10-13. Fault geometry can be inferred at profile intersections, and coincides with the general tectonic fabric observed on land and beneath the Skagerrak Sea. These areas were deformed during the Proterozoic Sveconorwegian orgenyin and the formation of the Permian Oslo Rift. Due to the post-Permian flattening of the Skagerrak Sea proper, the relative age and movements of the basement faults could not be given. This study shows that faults in the upper crystalline crust are mappable by seismic means under favourable conditions. Such measurements have the potential of resolving such problems as block geometries with depth and recent seismotectonic movements.

Introduction:

Deep seismic reflection profiles from the continents often show a reflective lower crust and Moho. In comparision ,the upper crystalline basement (down to 10-20 km depth) usually lacks coherent reflections and in turn is dominated by scattered energy. This statement does not exclude presence of upper crustal reflectors which typically are observed in areas of major crustal deformation such as the Grenvillian province in eastern Canada. (Green et. al., 1989) Similarly, large scale faults in the upper crystalline crust are easily identified in seismic reflection profiles (Klemperer and Hurich, 1990, Bois, 1991, Brewer et. al. 1980) This paper addresses seismic identification of relative small-scale faults in basement rocks, which may be related to those observed in exposed rocky terrain.

In 1987 a deep seismic survey was conducted in the Skagerrak Sea by the R/V Mobil Search (Fig.1, acquisition details in Table 1). The original onboard processed seismic sections revealed numerous lower crustal and upper mantle features (e.g. see Husebye et al.1988, Larsson and Husebye 1991, Lie et al., 1990 and Pedersen et al. 1990). The original onboard stacked data (0-16 s TWT) were subjected to a new extensive post-stack processing sequence including FK-migration (details in Table 3) as a part of a cooperative study with the British Institutions Reflection Profiling Syndicate (BIRPS). To utilize the full information potential of the collected seismic data the upper 6 sec. of the sections, limited to 0-6 sTWT, were reprocessed to commercial exploration standard including DMO and post-stack migration (processing details in Table 2).

The enhanced quality of the reprocessed seismic sections has enabled us to investigate some fundamental aspects of marine seismic

profiling resolution such as the extent to which faults in the crystalline basement are seismically mappable. Commercial exploration seismic surveys have rarely been attempted in areas with marginal sediment cover, as in the northern Skagerrak Sea. On the following high-quality profiles , seismic images of subtle but consistent faulting in the upper crystalline crust are described.

The Skagerrak tectonic setting

The Skagerrak Sea is considered to be a continental platform area between the Sveconorwegian terrains of the stable Baltic Shield to the northwest and the mobile belts of north-western Europe to the southwest. The separation of the two tectonic units is along the Fennoscandian Border Zone (FBZ) as shown in Fig.1. The landward Sveconorwegian rocks are of Proterozoic age (1.7 -1.4 Ga) and the youngest are the Permian volcanics of the Oslo Rift (Gaal and Gorbatchev, 1987, Bjørlykke et. al., 1990). The Sveconorwegian-Grenvillian orogeny (1.25-0.85 Ga) affected the southern part of Norway and Sweden with extensional and compressional forces mainly acting in the E/W-direction (Falkum, 1985). The onshore Bamble zone, a high grade metamorphic terrain, is hypothesized to have been uplifted an estimated 15-20 km relative to the westward Telemark block along the Porsgrunn-Kristiansand fault zone during the above orogeny (Falkum and Starmer, pers. comm.). On the deep seismic profiles major structural elements can be identified in the crust and mantle under the N. Skagerrak Sea which correlate well with the geometry of the tectonic boundaries mapped on land to the northwest (Lie and Husebye, 1992, Lie et al. 1992b).

There is little evidence of tectonic activity in the late Precambrian , but probably the general area was of low relief (Ramberg and Spjeldnæs, 1978). The Permian graben formation of the Oslo Rift was preceeded by the formation of narrow sedimentary troughs in Cambro-Silurian times

18

(Bjørlykke, 1983). Extensive volcanism within the landward part of the Oslo Rift (the Vestfold and the Akershus grabens) is obvious but the rift appears to lack a significant volume of volcanics in its seaward extension. the Skagerrak Graben (Fig. 1)(Lie et al., 1992b). Erosion in Late Permian / Early Triassic times has affected the entire Skagerrak Sea proper with Paleozoic sediments preserved only within the Oslo Rift system.

The major faults in the Skagerrak Sea are shown in Fig. 1. The general tectonic trend direction is N/S (NNE and NNW in the coastal areas to the east an west, respectively) (Ramberg and Gabrielsen, 1977). The major onshore faults appear to have formed prior or during the middle Proterozoic Sveconorwegian orogeny (Starmer, 1985) but some have clearly been reactivated at much later times, especially during the Permian rift phase (Spjeldnæs, pers. comm.). The landward faults are well established as major structures on geological grounds, but fault geometries at depths greater than a few kilometres are uncertain. In the northeast Skagerrak Sea, faults have been mapped essentially on the basis of bathymetric and shallow seismic (sparker) data (Floden, 1973). In the southern Skagerrak Sea the OG-profiles and other exploration seismic profiles have been used to map the Skagerrak Graben (e.g. see Husebye et al., 1988, Lie and Husebye, 1992, and Kinck et. al., 1991 among others).

Seismic identification of faultplanes in the crystalline crust.

The deep seismic profiles from Skagerrak (Table 2) provide clear crustal cross-sections as shown in Fig. 2. The bounding faults of the Skagerrak Graben (Fig.2) form strong, dipping reflections that are easily recognized seismically, similar features documented from many other places in the world.(e.g. see Leven et al., 1990). However, the smaller scale faults that outline the basement blocks on the surface of rocky terrain are not easily identified (Fig. 2, line OG-13).The seismic signature of the upper crystalline

19

crust (say above 5 sTWT) is often dominated by scattered energy and somewhat chaothic reflections. Close inspection of the migrated sections, reveals dipping, weak seismic features in the upper crystalline crust (fig. 2-5). These examples are acquired from areas where the sediment cover is less than 1-2 km. We interpreted these features as moderately dipping faults. Supportive evidence for this interpretation is that these presumed faults can be identified jointly at both sections at intersecting profiles as demonstrated in Fig. 4. Their strike generally coincides with the main tectonic lineaments of the surrounding onshore area, and also with the inferred fault trends from early bathymetry and seismic sparker data (Floden, 1973). The faults in the crystalline basement are in places observed to coincide with offsets in the overlaying sedimentary cover (Figs. 4 and 5). The fault planes can be mapped down to 4-5 s on the time sections equivalent to approximately 10-13 km depths and their appearent dip angles are in the range 20-50 deg. (Fig. 6).

Steep fault planes are generally attenuated in a stack which emphasizes horizontal reflectors. In sedimentary strata such faults are indirectly identifyed through abrupt offsets in the stratification, and not as a direct image of the fault plane itself. Similarly, in the chaotic pattern of the upper crust, steep faults are not only imaged as reflections from the fault plane, but indirectly as aligned terminations of short diffractive "events" against the fault. The fault planes are barely visible, if only viewed as offsets in the uncorrelated "noise" at one "time-sample level", but as alignments across the section they are more easily identified. The fault signature discussed above is subtle and can easily be overlooked especially when the quality of the seismic sections is not optimum. In either version of the reprocessed sections (Table 2 and 3), the post-stack migration of the data has had a major positive effect on bringing out fault plane images, although some also appear on the unmigrated sections. Reflections from minor faults

20

in crystalline basement have also been reported from Sweden where the observations later were confirmed by drilling (Juhlin, 1990). The bore-hole log information showed that the thin layers of fractured granite gave adequate impedance contrasts to provide observable reflections.

Many of the above described dipping crustal features have weak signatures, so alternative explanations for these observations have been considered. The most obvious candidates are diffractions and reflected refractions (Young et. al.,1990). We tested this hypothesis by using models of zero-offset diffraction hyperbolas based upon representative velocity functions (Fig. 7). These in turn were compared to the interfered faults but did not coincide. Out-of-plane diffractions are more difficult to verify or exclude as they may appear within a much wider dip range. Potential reflect-refraction events were also modelled (Fig 7) but did not provide a likely alternative to the fault interpretations in Figs 2-5. To summarize, we claim that the above seismic sections / structural examples are probably not attributable to diffractions or processing artefacts. In essence, we consider it feasible to identify by seismic means faults in the upper crystalline crust given good profiling data in areas with sparse sedimentary coverage.

Basement Fault Mapping

Crystalline basement faults are most commonly observed in the northern Skagerrak Sea where the sediment cover is less than 1-2 km. Hence our mapping efforts were limited to the profiles OG-8, OG-9, OG-12, OG13 and the northern segments of OG-2 and OG-3. The results are shown in Fig 6 in the form of time-to-depth converted line drawings using a representative velocity-depth function. The fault density is relatively high with a separation distances amounting to a few kilometres. Fault intersections are frequently observed, albeit the dominant trend is towards the Skagerrak Graben.

21

Implicit in the later statement is that the identified faults are roughly parallel to this dominant structural feature. Evidence for this in terms of determined strike and dip of fault planes is only available around line-crossings like the OG-13/OG-8 as demonstrated in Fig. 4. Similar strike directions were found at all other line crossings in the northeastern Skagerrak Sea.

The relative movements along the mapped basement faults are difficult to assess because the late Permian / early Triassic erosional event post-dates the latest tectonic deformation episode. This erosional event, following the Permian rifting, removed the Paleozoic sediment cover in the Skagerrak Sea proper and 'flattened' the basement topography except in the Oslo Rift (Fig. 2). The overlying thin Mesozoic and Cenozoic sediment cover in the northern Skagerrak Sea is relatively undeformed. However, in the southern Skagerrak Sea which has a thick sedimentary cover, we were unable to identify basement faults. An exception here is the low angle bounding faults of the Skagerrak Graben (Fig 2) where Cambro-Silurian and syn-rift sediment thickness may exceed 3-4 km. Note, in the latter case these faults where observed even in the original stacked sections.

Discussion

In the preceeding sections we have, in our opinion, provided evidence moderately dipping faults can be imaged. Beneath the Skagerrak Sea one precondition for this is that the sediment cover does not exceed a few kilometres which would lower the signal-to-noise ratio. The data resolution can be adversely effected by scattering effects in areas with a hard uneven sea floor with no sediments (Larner et. al., 1983, Lie et. al., 1990). Our interpretation of these fault signatures is supported by the fact that in places they do coincide with offsets in the sediments and sea floor. Fault planes can

also be mapped on crossing profiles and their infered strike and dip coincides well with the overall tectonic trend of the surrounding area.

Floden (1973) and others have on basis of sparker profiles and bathymetric mappings "identified" a few prominent faults in the northeastern Skagerrak Sea (Fig. 1). These hyothesized faults are not uniquely recognized in our results (Fig. 6). This may be due to the relatively long source-near trace offset on the Mobil Search lines which in shallow waters yields poor resolution in the uppermost part of the section. This in turn makes correlation to detailed bathymetric data difficult.

The northern Skagerrak sea results may be used to resolve tectonic evolution problems. For example, most of the graben cross-sections, with exception of profile OG-7 (Fig 2), show asymmetric half-grabens with prominent bounding faults. The main strike of these faults is mostly to NNE which roughly coincides with the infered strike directions of the mapped basement faults. On the basis of our findings we conclude that the extensional deformation during the Permian rift phase has not been limited to the narrow Skagerrak Graben per se. but probably was absorbed along the many basement faults mapped in the entire NE Skagerrak. This has importance for properly estimating the crustal extension during the rifting (Pedersen et al., 1991). Note, the Permian Oslo Rift is located in an `inherited` Sveconorwegian structure implying that basement faults could either be the same ageas the rift or most likely considerably older (Ramberg and Spjeldnaes, 1978, Falkum, 1985).

Finally, we want to address the so-called seismotectonic concepts popular in earthquake hazard analysis (eg. see Gregersen and Basham, 1989). These kinds of problems are of interest in the Skagerrak Sea as the largest Fennoscandian earthquake in modern times (Husebye et al., 1978) took place in the outer Oslo Fjord in 1904. Occasionaly we observe that

23

basement faults offset the present day Mesozoic/Cenozoic sediment cover in the northern Skagerrak Sea implying that the area has not remained tectonically quiscent. In a seismotectonic context fault candidates are numerous; the graben bounding faults , one of the many faults outside the graben or the prominent low angle Bamble shear zone extending from the Bamble sector towards the the Swedish west coast (Lie et al., 1992a). Although the epicentre of the 1904 earthquake is not well constrained, the point is that under favourable conditions it should be possible to map seismically active faults with reflection seismic profiling. High resolution profiling systems are needed to resolve fault offset in the youngest sedimentary strata.

Concluding remarks

We have reported on observations of moderately dipping faults within the upper crystalline crust on reflection profiles. Such faults are not generally recognized seismically because full exploration standard marine seismic surveys are not often undertaken in areas with little sedimentary cover. The subtle fault signatures documented here are therefore easily overlooked or dismissed as artifacts. As conventional seismic profiling strategy and data processing are not focused on non-horizontal structural features our interpretatoins may be somwhat uncertain because of this basic limitation. In a later paper we will address this problem in terms of generating synthetic reflection seismograms and using commercial software for stacking and migration The usefulness of such approaches have been demonstrated by Blundell and Raynaud (1986) , Raynaud (1988) and Cao et al. (1990) among others.

Acknowledgements

references

Bjorlykke, K. (1983) Subsidence and tectonics in late Precambrian and Paleozoic sedimentary basins. Nor. Geol. Unders., 380, 159-172.

Bjorlykke, A., Ihlen,P.M. and Olsrud,S. , Metallogeny and lead isotope data from the Oslo Paelorift, Tectonophysics, 178,109-123.

Blundell, D.J. and Raynaud, B.A. (1986) Modeling lower crustal reflections observed on BIRPS profiles. In: Reflection Seismology: A Global Perspective (ed. by M. Barazangi) Am. Geophys. Union, Geodyn. Ser. ,13, 287-295.

Brewer, J., Smithson, S., Oliver, J. Kaufman, S. and Brown, L. 1980,The laramide orogeny: Evidence from COCORP seismic reflection profiles in the Wi d River Moutains, Wyoming. Tectonophysics, 62,165-189.

Cao, S., Kennet, B.L.N., Goleby, B.R. (1990) 3D isochronal modelling of reflections from the deep crust: application to reflection profiling in central Australia, Tectonophysics, 173, 119-128.

EUGENO-S Working Group (1988) Crustal structure and tectonic evolution of the transition between the Baltic Shield and the North German Caledonides (the EUGENO-S Project) Tectonophysics, 150, 253-348.

Falkum, T. (1985) Genetic evolution of Southern Scandinavia in light of a Late-Proterozoic plate-collision, in: The deep Proterozoic Crust in the North Atlantic Provinces, (ed. by A.C. Tobi and J.L.R. Touret), D.Reidel Publ co, Dordrecht, NATO advanced Science Institutes Series, ser. C, 158, 309-322.

Floden, T., (1973) Notes on the bedrock of the eastern Skagerrak with remarks on Pleistocene deposits. Stockholm Contrio. geol., XXIV; pp 79-102.

Gaal, G. and Gorbatchev, R., (1987) An outline of the Precambrian evolution of the Baltic Shield, Precambrian Res., 35, 15-52.

Green, A.G., Milkhereit, B., Davidson, A., Spencer, C., Hutchinson, D. R., Cannon, W.F., Lee, M.W., Agena, W.F., Behrendt, J.C., & Hinze,W.J., 1988 Crustal structure of the Grenville front and adjacent terranes, Geology, 16, 788-792.

Gregersen, S. and Basham, (editors) (1989) Earthquakes at North-Atlantic Passive Margins: Netectonics and Postglacial rebound. Kluwer, Dordrecht, pp. 716.

Husebye, E.S., Bungum, H., Fyen, J. and Gjosdal, H. (1978) Earthquake activity in Fennoscandia between 1497 and 1975 and intraplate tectonics. Nor.Geol. Tidskr., 58, 51-58.

Husebye, E.S., E.S. , Ro, H.E., Kinck, J.J., and Larsson, F.R., (1988) Tectonic studies in the Skagerrak province: the Mobil Search Cruise. Nor. Geol. Unders., Special Publ. 3, pp14-20

Juhlin, C. (1990) Interpretation of the reflections in the Siljan Ring Area based on results from the Gravberg-1 borehole. Tectonophysics, 173, 345-360.

Kinck, J.J., Husebye, E.S. and Lund, C.E., 1991. The south Skandinavian crust: Structural complexities from seismic reflection and refraction profiling. Tectonophysics, v 189, pp 117-133.

Larner et al., 1983. Geophysics, 48, 854-886.

Larsson F.R. and Husebye, E.S. (1991) Crustal reflectvity in the Skagerrak Sea. Tectonophysics, 189, 135-148.

Leven, J.H. Finlayson, D.M., Wright, C., Dooley, J.C., and Kennet, B.L.N. (eds) (1990) Seismic probing of continents an their margins. Tectonophysics, 173, pp 641.

Lie, J. E., Pedersen, T. and Husebye, E.S. (1990) Observations of seismic reflectors in the lower lithosphere beneath the Skagerrak. Nature, vol. 346, 165-168.

Lie, J.E. and Husebye, E.S. (1992) Deep crust and mantle structures related to rifting and basin formation in Skagerrak; New results from reprocessing of deep seismic profiles. m/s submitted for pulication.

Lie, J.E. and Husebye, E.S. (1992a) Simple shear deformation of the skagerrak lithosphere; implications for the Oslo rift formation. m/s submitted for pulication.

Lie, J. E., Kinck, J.J., E.S. Husebye and Larsson, F.R. (1992b) Cambro-Silurian sediments and basement geology in N.Skagerrak - New evidence from seismic profiling. Submitted Stockholm Contrio. geol.

Lind, G. (1982) Gravity Interpretation of the Crust in South-Western Sweden. PhD thesis, Geologiska institusjonen, Publ. A 41, Gøteborg.

Pedersen, T., Pettersen, S.E. and Husebye, E.S. (1991) Skagerrak evolution derived from tectonic subsidence. Tectonophysics, 189, 149-163.

Ramberg, I.B. and Speldnes, N., (1978) The tectonic history of the Oslo Region. In: Tectonics and Geophysics of continental Rifts. (ed. by I.B. Ramberg and E.R. Neumann) D.Reidel Publ co, Dordrecht, Nato advanced Study Institutes Series C, no 37, 167-194.

Raynaud, B.A. (1988) Diffraction modeling of 3-D lower-crustal reflectors. Geophys. J. 93, 149-161.

Starmer, I. C. (1985) The evolution of the South Norwegian Proterozoic as revealed by the major and mega-tectonics of the Kongsberg and Bamble sector, in: The deep Proterozoic Crust in the North Atlantic Provinces, (ed. by

A.C. Tobi and J.L.R. Touret), D.Reidel Publ co, Dordrecht, NATO advanced Science Institutes Series, ser. C, 158, 259-290.

Young, R.A., Stewart, S.C., Seman, M.R., and Evans, B.J. (1990) Fault-plane reflection processing and 3D display: the Darling Fault, Western Australia, Tectonophysics, 173, 107-117.

RECORDING PARAMETERS,
R/V Mobil Search survey Skagerrak 1987

RECORDED BY:	MOBIL E&P SERVICES INC
INSTRUMENT TYPE:	TI DFS 5.5
RECORD LENGTH:	16 000 MSEC
SAMPLE RATE:	4 MSEC
TRACES/RECORD:	180
FIELD FILTER:	LOWCUT 5.3 HZ
	HIGHCUT 90 HZ
SLOPE:	LO - 18 DB/OCT
	HIGH - 72 DB/OCT
HYDROPHONES PR GROUP:	32
GROUP INTERVAL	25 M
NUMBER OF GROUPS:	180
ACTIVE STREAMER LENGTH:	4499 M
STREAMER DEPTH:	15 M
OFFSET:	262 M
TUNED WIDE AIR GUN ARRAY	
ARRAY DIMENTIONS:	59 M LONG X 75 M WIDE
NO. OF SUB-ARRAYS:	4 X (12 GUNS OVER 59 M)
SUB-ARRAY SPACING:	25 M BETWEEM STRINGS
PRESSURE/CAPASITY:	1800 PSI/7200 CU IN
TOWING DEPT:	10 M
SHOTPOINT INTERVAL:	50 M
CDP SPACING:	12.5 M
FOLD:	45

Table 1. Recording parameters during the R/V Mobil Search seismic profiling cruise in Skagerrak Sea, 1987.

PROCESSING SEQUENCE, R/V Mobil Search survey Skagerrak 1987, Reprocessed 0-16 s TWT, 1990/1991

```
(1987, ONBOARD R/V MOBIL SEARCH)

1. INSTRUMENT DEPHASE FILTER
2. TRACE MUTE
3. GAIN CONTROL
4. TRACE COMPOSITE, 5 TO 1, SEVEN WINDOWS
5. GAPED DECONVOLUTION
        GATE 200-6000 s      LENGTH 248 ms
        GAP = 32 ms
        GATE 6000-13000 s    LENGTH 352 ms
        GAP = 64 ms
6. CDP GATHER
7. NMO
        Velocity analysis every 3 km
8. TRACE MUTE
9. MEAN STACK       43 FOLD
        with spike rejection

(1990/1991 Post stack reprocessing, BIRPS, Cambridge, UK)

1. RESAMPLE          16 ms
2. TRACE-SUMATION
        2 adjacent traces
3. GAIN BALANCING
        varying design and application
4. GAPED DECONVOLUTION
        GATE 1400-5000 s     LENGTH 248 ms
        GAP = 36 ms
        GATE 6000-13000 s    LENGTH 600 ms
        GAP = 85 ms
5. FK DIP-FILTER
        polygone rejecting steeply dipping events
6. AGC SCALING
        window, 250 ms      gate 50 - 4000 ms     pct 20
        window, 1000 ms     gate 50 - 6000 ms     pct 30
        window, 5000 ms     gate 50 - 16000 ms    pct 40
7. FK-MIGRATION
        estimated velocity time function
8. BANDPASS FILTER
        lo      slope        hi      slope
        [Hz]    [db/oct]      [Hz]    [db/oct]
        6       18           24      18
9. DISPLAY
        bias 67          gain 2
```

Table 2. Processing sequence, for the reprocessing of the 0-6 s TWT seismic data from R/V Mobil Search cruise in Skagerrak Sea, 1987.

31

PROCESSING SEQUENCE, R/V Mobil Search survey
Skagerrak 1987, Reprocessed 0-6 s TWT, 1989

1. FK-FILTERING ON SHOT RECORDS
   Dips   rejected: +14 to - 5 ms/trace
           passed :   + 8 to -1 ms/trace
2. SPHERICAL SPREADING COMPENSATION
3. DBS
   Gaped deconvolution
   Gap: 32 ms   Filter length: 240 + 32 ms
4. CDP SORT
   45 fold. 12.5 m CDP distance
5. VELOCITY ANALYSIS
6. SCALING
   AGC scaling pre DMO, Window : 400ms
7. DIP MOVEOUT
   NMO with stacking velocities
   correction on 45 offset planes
8. DESCSCALE
   Removal of previous 400ms AGC after unNMO
9. NMO WITH STACKING VELOCITIES
10. INNER AND OUTER TRACE MUTE
11. SCALING
    AGC scaling pre stack, window: 250 ms
12. STACK
    45 fold stack, 12 5 m CDP distance
13. MIGRATION
    Finite-difference time migration
    migration layer thickness 40 ms
14. DIP FILTER
    Rejected + 3.5 to -3.5 ms/trace
    Passed   + 2 to -2 ms/trace
15. DAS
    Gaped deconvolution
    gap: 32 ms   Filter length: 240 + 32 ms
16. LINEAR GAIN
    Varying design and application
17. TIME VARIANT FILTER

TIME [ms]	LC [hz]	SLOPE [db/oct]	HC [hz]	SLOPE [db/oct]
0 500	18	72	70	48
750 1000	12	48	70	48
4000 4200	8	48	40	72
5000 6000	8	48	30	72

    interpolation between filterzones
18. SCALING
    50 ms robust AGC
19. DISPLAY

Table 3. Processing sequence,for the reprocessing of the 0-16 s TWT seismic data from R/V Mobil Search cruise in Skagerrak Sea, 1987.
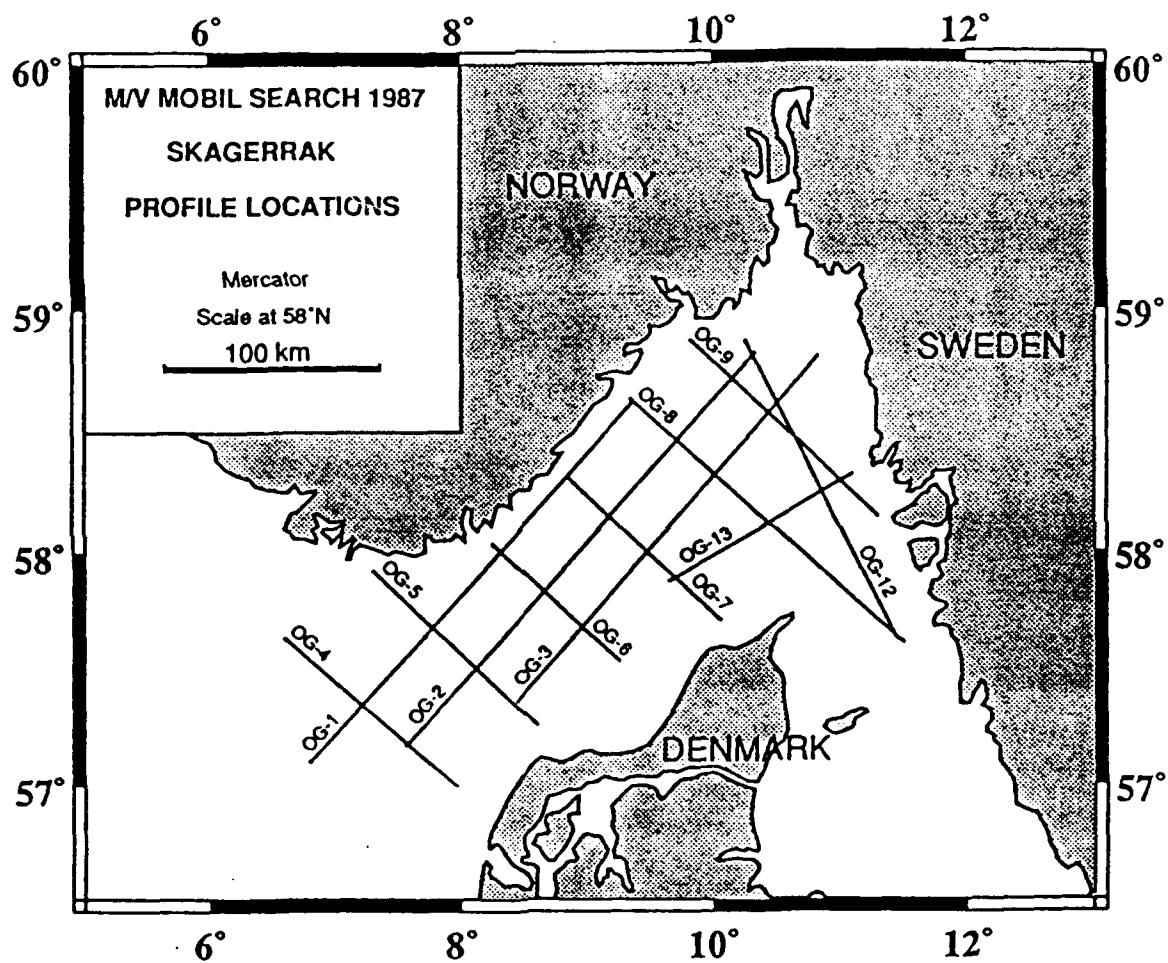
Fig 1a. Profiling map, R/V Mobil Search cruise in Skagerrak, 1987.
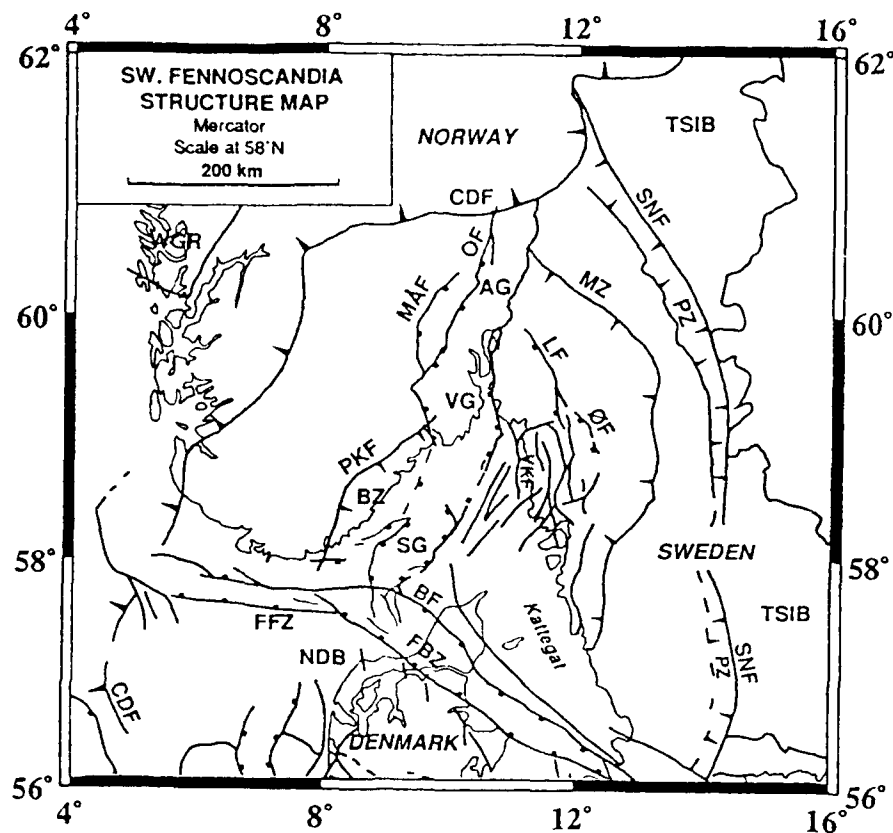
Fig 1b. Tectonic map of the southwestern part ot the Baltic Shield based on works of Gaal and Gorbatschev (1987), EUGENO-S Working Group (1988), Lind (1982) and Floden (1973). AG: Akershus Graben, BF: Børgum Fault, BZ: Bamble Zone, CDF: Caledonian Deformation Front, FBZ: Fennoscandian Border Zone, FFZ: Fierritslev Fault Zone, LF: Løten Fault Zone, MZ : Mylonite Zone, MÅF: Meheia-Ådal Fault Zone, NDB: Norwegian-Danish Basin, OF: Oppland Fault Zone, PKF: Porsgrunn-Kristiansand Fault Zone,PZ: Protogine Zone, SG: Skagerrak Graben, SNF: Sveconorwegian Front, TSIB: Trans-Scandinavian Ignious Belt, VG: Vestfold Graben, WGR: Western Gneis Region, ØF: Øymark Fault. Note, the Oslo Rift comprises the Skagerrak, Vestfold and Akershus Grabens.
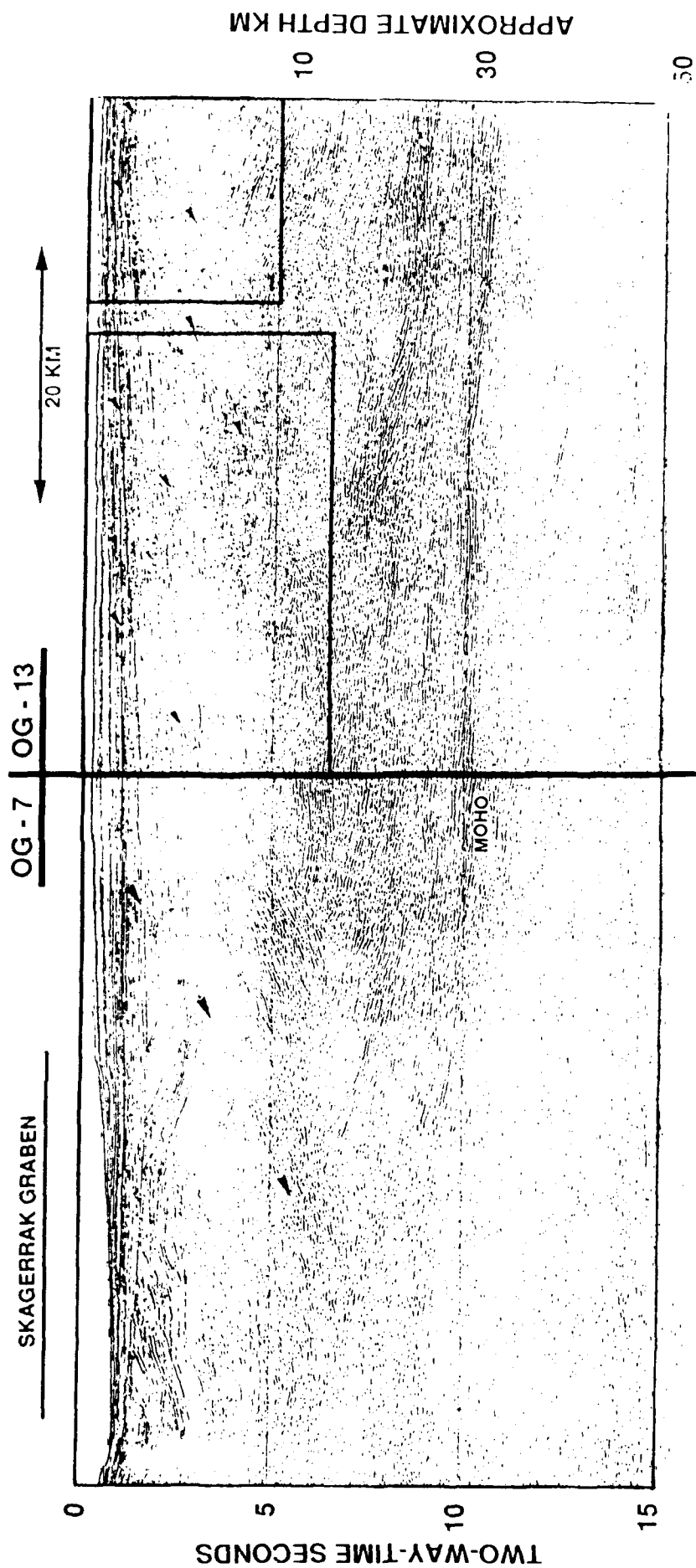
Fig. 2 Migrated seismic sections from intersecting profiles OG-7 and OG-13   OG-7 section East of the graben the Moho is extremely well defined. The

arrows identify fault planes in the upper crystalline crust. Blow-ups of the two   sub-Moho lithosphere is seismically non-reflective though the lower mantle

framed boxes (A and B) are shown in Figs 3 and 4. Note the rotated crustal   lithosphere appears to be reflective in this area (analysis of 40 s TWT

blocks inside the Skagerrak graben where the boundary fault to the east can   reflection data (e et al. 1990)

be traced down to 6 s or a depth of approximately 17 km as marked in the
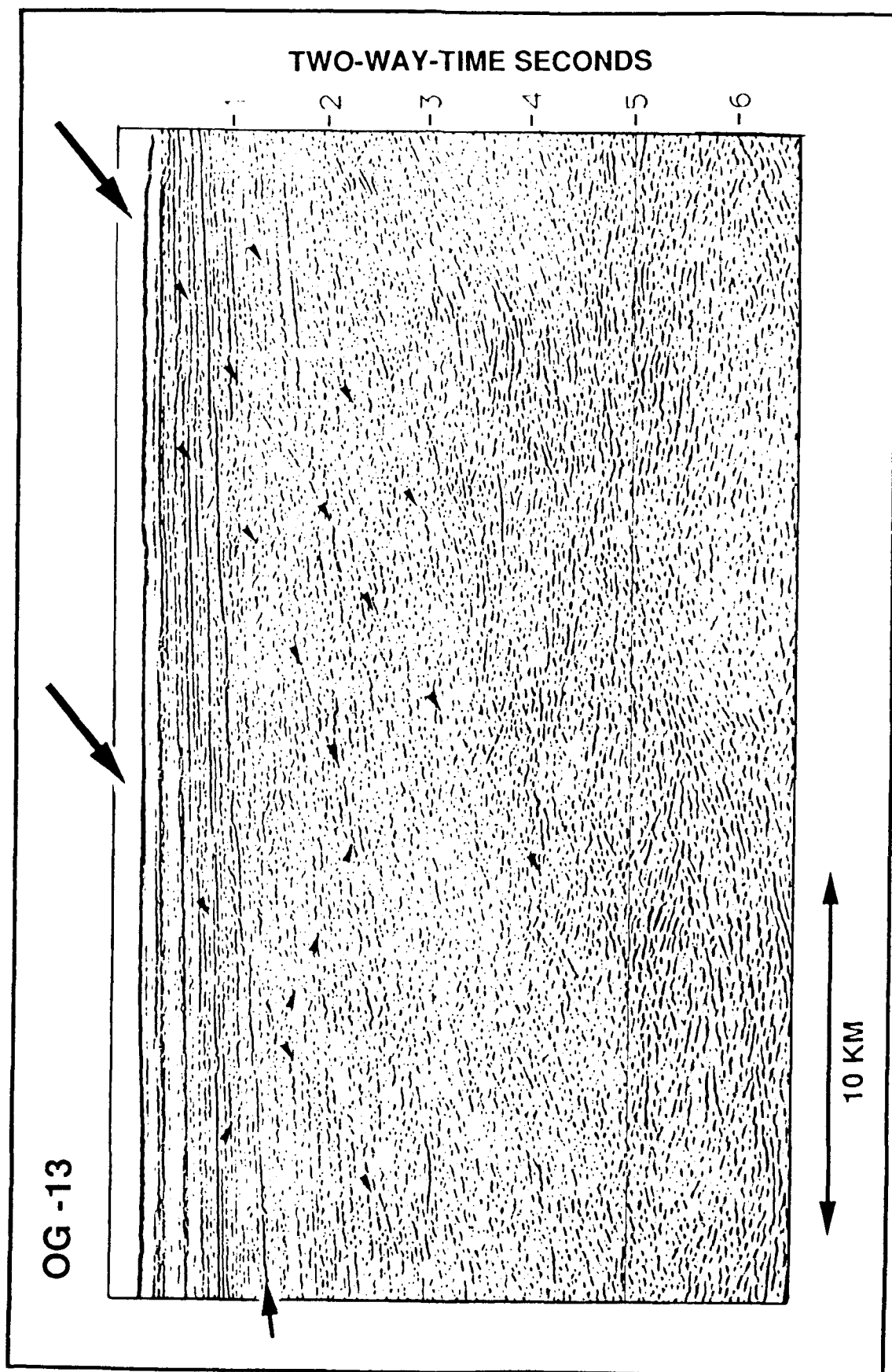
Fig 3 Detail A of profile OG-13 shown in fig 2. The most prominent faults in also marked with an arrow at 1.5 s and horizontal events below are water the crystalline basement are marked with arrows. Top basement ref... column multiples
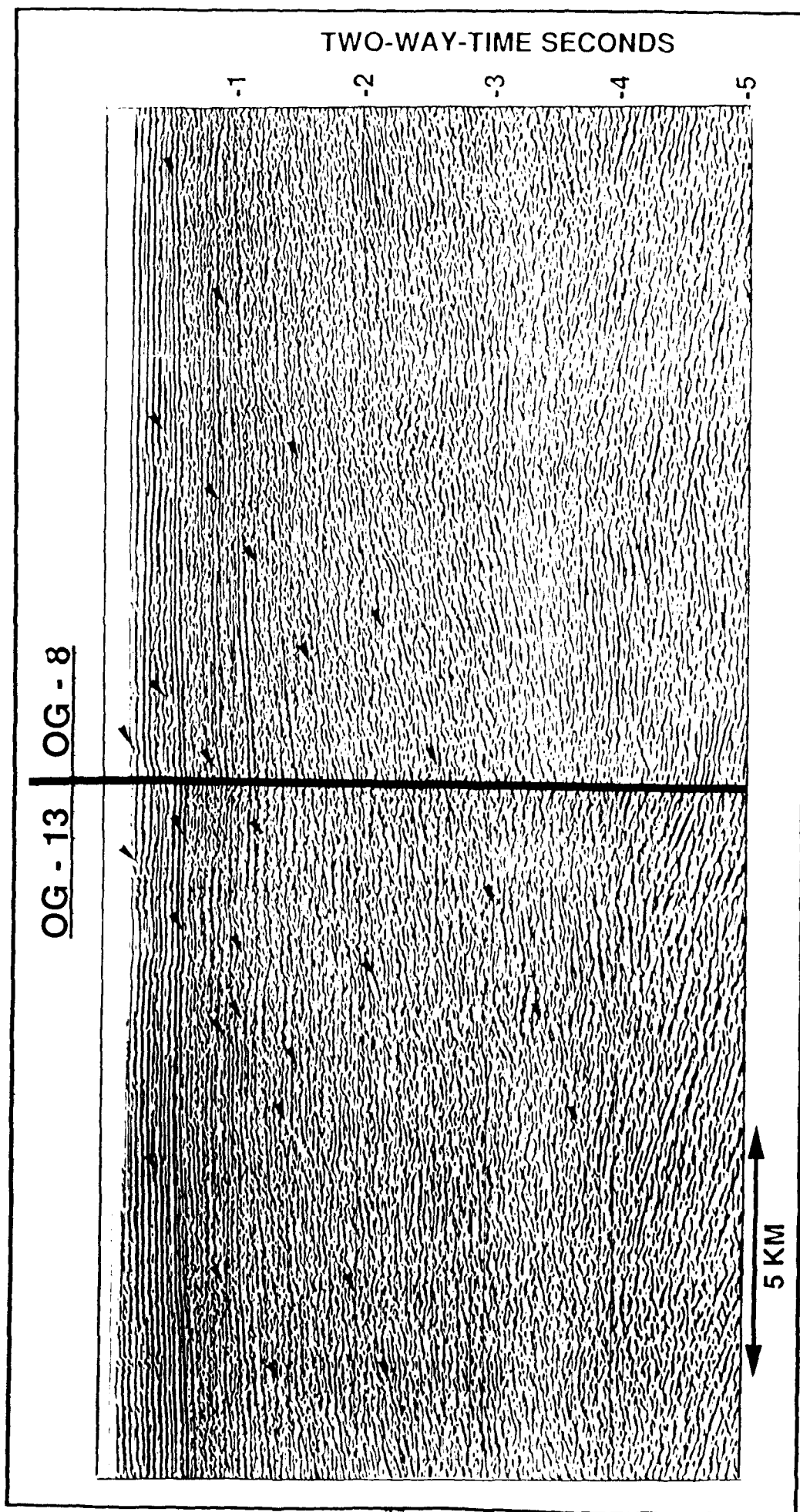
Fig 4 Details of migrated crossing profiles OG-13 (B) and OG-8 with NW on profile OG-8 Some of the basement faults coincide with offsets in the processing details in Table 2 Events interpreted as faults in the crystalline sediment layering Fault planes can be correlated between the two crossing basement are dipping mainly towards the SW on profile OG-13 and towards profiles
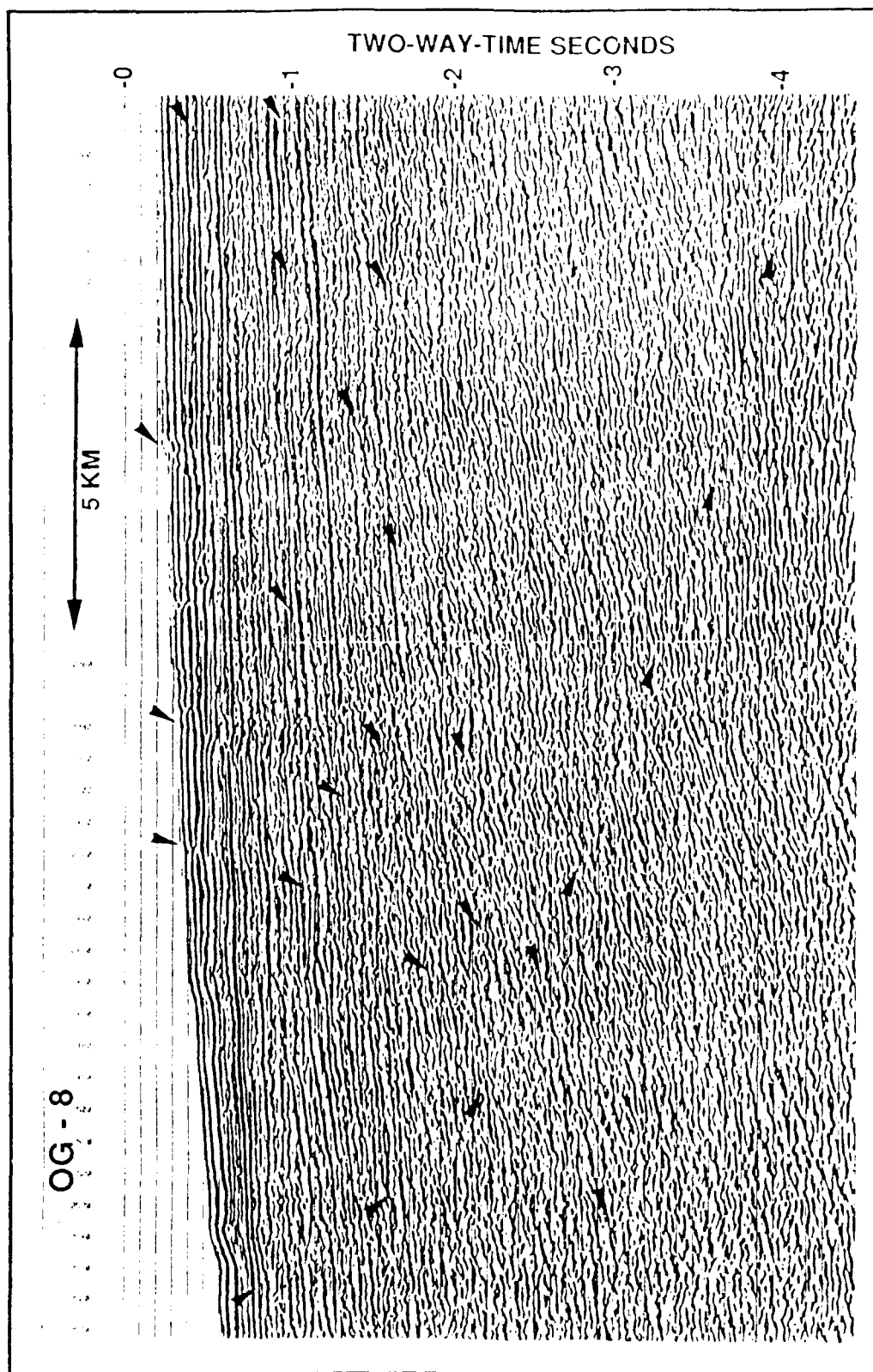
Fig. 5 Detail of migrated section OG-8 The most prominent basement faults   the Mesozoic/Cenozoic sediments and the seabed are marked with arrows. The normal-fault system is associated with offsets in
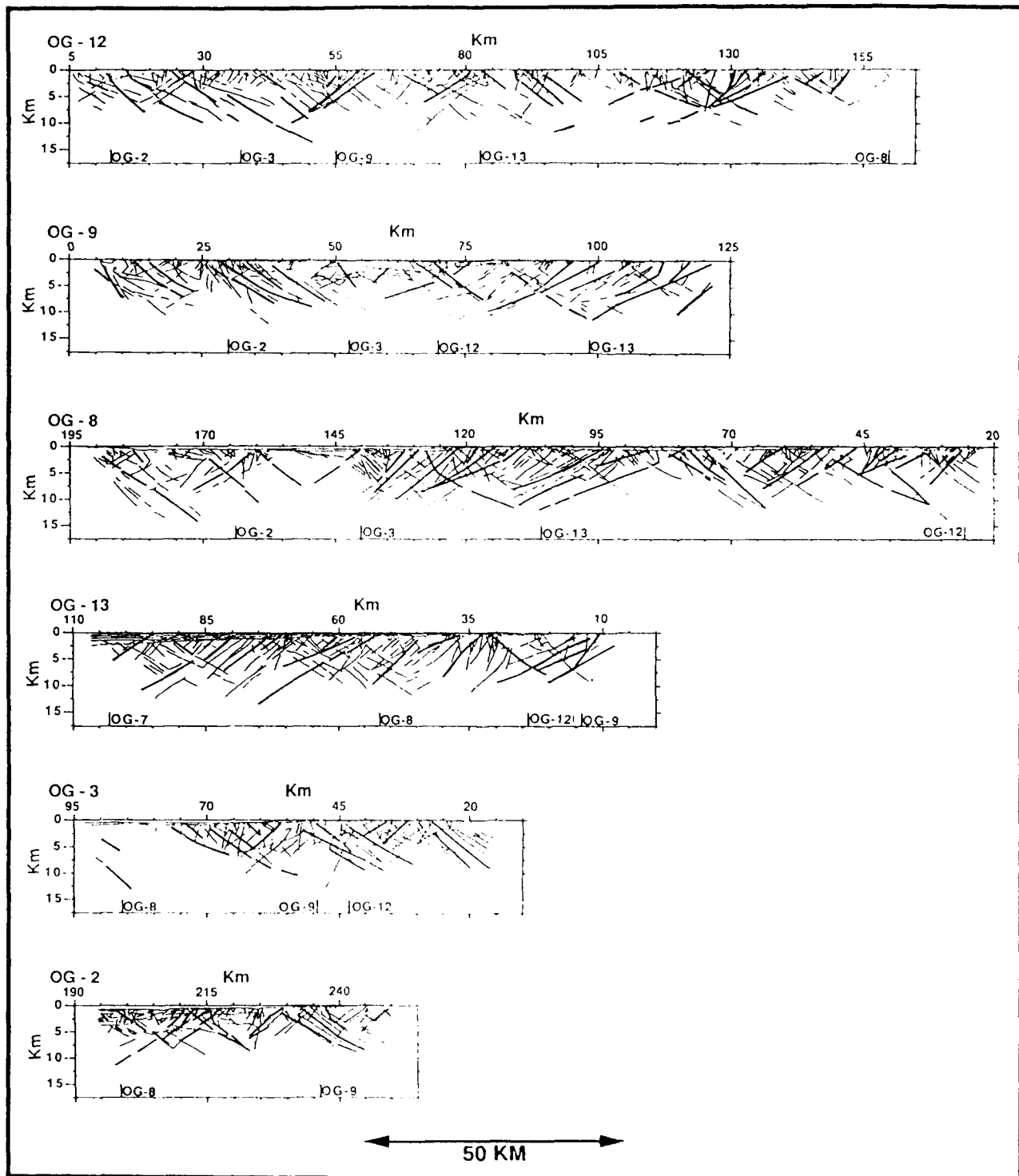
Fig. 6 The mapped faults on the migrated strike lines OG-12, OG-9, OG-8
and the crossing profile lines OG-13, OG-3 and OG-2. The line drawings are
time-to-depth converted using an estimated velocity-depth function. Thick
lines mark the most prominent faults on acount of continuity and deth
penetration.
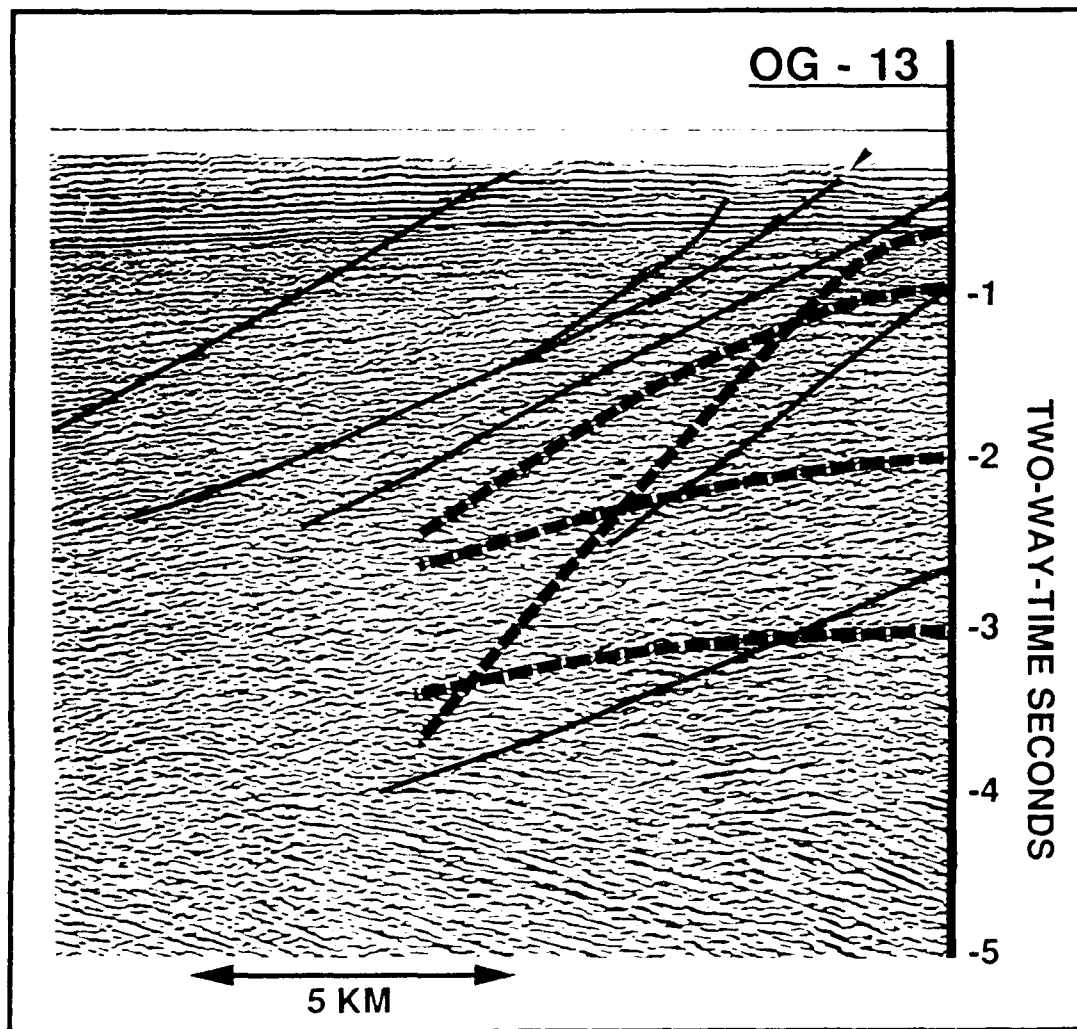
Fig.7   Parts of modelled zero-offset diffraction hyperbolas (broken lines) inserted on a OG-13 seismic section (left segment of Fig 4). Velocity-depth functions derived from N-Skagerrak profiling lines (Lic et al, 1992b). The hypothesis that our inferred faults (solid lines) should represent diffraction hyperbola artefacts is not considered tenable.

An exercise in automating seismic record analysis and network bulletin production

B.O. Ruud[1], C.D. Lindholm[2] and E.S. Husebye[2]

[1] Dept. of Geology, Oslo Univ., Oslo, Norway
[2] NTNF/NORSAR, Kjeller, Norway

Abstract

A long-standing problem in observational seismology is that of automating network oper-ation. In this study we report an experiment by which we use the detector described in Ruud and Husebye (1992) for automatically picking P- and S-arrivals in local event records stemming from the Norwegian Seismic Network. For automatic epitcenter deter-mination a novel, robust grid-search method well suited for estimation problems with non-Gaussian observational errors is introduced in order to handle outliers. Even several large arrival time outliers did not prevent solutions close to the "true" epicenter. In our experi-ment, 38 local events from the August 1991 bulletin were located. The number of detect-ing stations varied from 3 to 10 out of a total of 15 stations. P- and S-picking errors were small, mostly within 0.5 sec for both P and S. Phase identification errors, causing severely wrong P- and S-arrivals were more frequent. Decent epicenter determinations were obtained even for events with 30-50 per cent outliers. The average location difference of our "automatic" solutions compared to those in the manually produced bulletin were about 15 km.

1 Introduction

The most outstanding feat in observational seismology was the creation of the Jef-freys-Bullen tables in 1937. This was achieved on the basis of eminent analysis of analog

records from low-gain, mechanical seismometers in combination with novel statistical schemes for event location and travel time analysis (Jeffreys, 1932, 1967). Such an achievement would hardly be possible today, given the same type of recordings, in view of the deteriorating state of routine seismogram analysis at many observatories around the world. In an effort to correct this situation, the seismological community through IASPEI has launched the ISOP-project (International Seismological Observation Period) under NEIC/USGS management for re-establishing past skills in seismogram analysis and reportings to international agencies like NEIC and ISC.

The basic role of the seismological observatories is to provide data for *all* kinds of seismological research, and an important product in this respect is the daily event bulletin. The mentioned deterioration of routine seismogram analysis is tied to a curtailing of funding for such work while the workload is ever-increasing due to deployment of more and more modern, high-gain digital seismometers. As in similar situations, a viable solution might be to automate, to the extent possible, all aspects of the seismogram analysis including the bulletin production. This is the problem dealt with in this paper, and our observational data stem from the Norwegian Seismograph Network (NSN) operated by the University of Bergen. We note that several novel developments in seismic network operations have been published in recent years(Bache et al, 1990; Bratt et al, 1990; Boschi et al. 1990, 1991; Masse and Person, 1991).

2 Network configuration, instrumentation and data acquisition

The NSN configuration is shown in Fig. 1. The network Hub is physically located at the University of Bergen (station BER) where the routine data processing takes place. Note that KONO and the NORESS and ARCESS arrays do not constitute an integral part of the NSN, although their detection logs and associated waveform data are accessible. A comprehensive description of the field data acquisition is given elsewhere (Havskov et al.

1992), so here only the essential features of the system are given. The NSN is divided in a southern and a northern segment along latitude 62°N (Table 2). The main difference in network operation is that the southern stations transmit their recordings continuously in analog form to the HUB via leased telephone lines, while for the northern stations a simple STA/LTA detector is run on the site and only event recordings are transmitted in digital form to the HUB. Correct timing is ensured by radio clocks at each independent station (accuracy 1 ms). The principal features of the data acquisition are as follows (this applies both to field and Hub processes):

- The seismometer, Kinemetrics SS-1 Ranger, "raw" trace is subject to an analog, 5-10 Hz bandpass filter (12 dB per octave roll-off) and then transformed to digital form (50 Hz sampling rate) via a 12 bits A/D converter with an equivalent dynamic range of 72 dB.

- Signal screening via a conventional STA/LTA detector; STA window is 4 sec; LTA recursively updated and threshold setting varies from 3-6 units. This initial signal detection is performed only on one vertical trace for each station (irrespective of whether a station has 3C instrumentation or a cluster of sensors). System status parameters are also extracted (Havskov et al, 1992).

- If triggering occurs, detection information (STA/LTA, trigger time and duration) plus corresponding waveform data are stored in specific files. A ring buffer contains 20-45 hours (dependent on disk capacity and numbers of sensors) of continuous recordings of data for all seismometer traces at a station.

- Event definition and subsequent data retrieval is handled by the Hub computer.

The design of the field data acquisition system dates back to 1985/86. Planned upgrade will include 16 bits A/D converters with gain ranging (140 dB), increased CPU

43

power and disk storage in the field and more stations will have 3-component instrumentation.

3 Hub network detection screening – event data retrieval

Bihourly the Hub retrieves detection and status information from the individual stations in the network. Presuming no faulty instrumentation, the event definition task is resolved in the following way (see Havskov et al. for more details):

- Minimum 3 stations triggered within a 120 sec time window for either the southern or the northern NSN subnets. For each declared event, the retrieved record segments start 30 to 60 sec prior to the earliest station signal detection time and ends 30 to 60 sec after the latest detection state cancellation.

- The Hub retrieves the waveform files of uniform length from the ring buffers for *all* SP components for all stations in the field (backup files are used if ring buffer is overwritten). All waveform data is merged into an event file which constitute the base for the automated record analysis and the subsequent epicenter determination.

- The system is extensively parameterized, leading to a high degree of flexibility.

On a daily basis, an average of 4-6 seismic events are declared, including quarry blasts and mining explosions.

4 Automatic processing of event waveform data at the Hub

We have here adapted the signal detector procedures detailed in Ruud and Husebye (1992), hereafter referred to as Paper 1, for processing the single vertical component and the 3C station records of the NSN network. The process is parameterized, and thus providing some flexibility in most of the parameters.

- *Signal quality check:* Stations exhibiting relatively weak signals are deleted from further analysis according to a simple criterion. The maximum and minimum powers in a 5 sec moving time window are computed and if the max/min ratio is less than 3 the station is skipped.

- *Signal parameter extraction:* The records are prefiltered in 3 passbands, parameter setting details in Table 1. For each of these an STA/LTA detector is applied except for the first 10 sec which is used to initialize the LTA values. For 3C stations P-wave polarization statistics are used in combination with the STA/LTA power detector, and P-slowness parameters are also estimated (Roberts et al, 1989; Paper 1).

- *Signal parameter screening -- phase identification:* The detections within the different passbands are compared and the surplus (overlapping) ones are deleted with basis in a set of decision rules (for details see Paper 1). The earliest detection is presumed to be a P wave while the second one, the S wave (Sg or Lg), is associated with the strongest phase detection in the time interval 3 to 100 sec after P onset (illustrations in Figs. 2 and 3).

- *Coda duration -- local magnitude estimation:* The duration is reckoned from P onset time and until the subsequent coda power level in a window of length 5 sec is less than a factor of 1.6 of the initial LTA power.

Note that for local events P-S differential arrival times provide accurate epicenter distance estimates, and this, in combination with back-azimuth estimates from individual 3C stations, gives decent epicenter locations (e.g., see Ruud et al, 1988; Li and Thuber, 1991; Paper 1).

Automatic signal parameter extraction is not error-proof, and with basis in Paper 1 analysis we estimate that the probability of picking both P and S phases correctly at a sin-

45

gle station to be around 0.8. For the NSN-network (Fig. 1) there are typically 3-7 reporting stations for individual events, which implies that less than 30 per cent of the events would have "correct" P and S phase pickings at all detecting stations. Gross errors here could adversely affect the event location and the corresponding arrival time residuals might be "smeared" onto the other stations in the network and thus hide the erroneous phase picks. This so-called circular problem -- a good event location requires that outliers have been removed while outliers cannot be properly identified unless we have a good location -- has to be resolved to ensure automatic network operation.

5 Evaluation of the extracted signal parameters

The parameters used for epicenter locations at local distances are P and S arrival times and the P slownesses (that is, back-azimuth) for individual stations. Before attempting epicenter determinations, we undertook an appraisal of the quality of the signal parameters extracted automatically. In this respect 38 events (Table 3) from the NSN bulletin for August 1991 were analyzed. The "selection" criteria used were that an epicenter location existed in the manual bulletin and that digital records from at least 3 stations were at hand for the automatic analysis. Details on network performance is given in Tables 2 and 3 and in Fig. 4. and 5.

Arrival time pickings

Various kinds of errors were found in the automatically extracted signal parameters. The most frequently occurring ones were those due to interference with "alien" events or signals stemming from very local blasting. The arrivals could be picked correct in time but assigned wrong phase identification. For very local events it is often difficult to separate P- and S-phases ($\Delta < 40$km), so only P would be reported. In Figs. 2 and 3 the above-mentioned problems are illustrated in terms of waveform displays including our automatically picked P- and S-phase arrival times. The relative frequency of occurrence of such errors

can be judged from Tables 2 and 3. For example, for Event 1 the (manual) NSN bulletin gives 4 P readings and 3 S-readings, while the automatic phase-picker indicated 5 P- and 4 S-readings. However, during the location process, we find that 2 P and 2 S-readings from the automatic pickings were wrong (rejected) as indicated in the RP and RS columns to the right in Table 3. It also happened that the detector picked all P- and S-phases for a given event correctly; for our event population this happened for 12 out of 38 events (c. 30 per cent). Also, station reporting frequency varies considerably as indicated in Table 2. For example, the northern stations report mostly events in the Kiruna mining district in northern Sweden (67.7°N, 20.2°E) (Figs. 3 and 6).

Automatic P and S phase arrival time picking results are displayed in Fig. 4. The agreements between analyst and automatic pickings are very good, in particular for P phases. There are few outliers, as we have manually corrected for phase identification errors of the kinds discussed above. For S phases the residual average is non-zero, that is, positively biased a few tenths of a second. This reflects late triggering due to increased LTA after P-onset. We consider the automatically picked P and S arrival times to be satisfactorily precise compared to analyst pickings, and hence accurate event locations should be attainable.

Azimuth estimation

The NSN-network had 5 operative 3C stations during August 1991 (Fig. 1). For these stations the detector reported back-azimuths of assumed P-phases plus a phase identification measure, the so-called PS-parameter (details in Paper 1). This parameter indicates whether the particle motion is P-type (PS = 10 -- pure P) or S-type (PS = 0 -- pure S). In Tables 2 and 3 and Fig. 5 the performance of azimuth observation is indicated. The accuracy of the accepted azimuth estimates at the NSN station were close to 3C azimuth observations from NORESS, ARCESS and Finnish stations (Paper 1; Suteau-Henson, 1991; Tarvainen, 1992) and could apparently be improved by correcting for a bias at some sta-

tions. However, many P-wave azimuth determinations failed to meet our PS-criterion, (Table 1). Estimation stability would probably improve with instrumentation having relatively better dynamic range and bandwidth. Also scattering from the rough topography near the NSN stations (compared to for instance NORESS and ARCESS) might corrupt P-wave polarization properties.

Signal amplitude (STA) and coda duration measures

The detector extracted both these parameters for each event detected. For 3C stations the STA ratio between different components is rather unstable and was not found useful for phase identification. In contrast, the STA of S-phases is almost always larger than STA of P for local events. The coda duration parameter as estimated was rather unstable; small disturbances in the late coda could change their value by a factor of 2. This parameter was therefore not used in magnitude estimation. Magnitude estimation based amplitude (time or frequency domain) is feasible, but not yet implemented. However, we consider local magnitude (M_L) estimation an important task, which can be resolved (Alsaker et al., 1990; Båth, 1981; Michaelson, 1990). For example, the M_L parameter may serve as an important measure for flagging local events of marginal interest, that is, the numerous small ($M_L \leq$ 1.0) man-made chemical explosions.

Comments

The outcome of our analysis of 200 station records from the NSN-network, displayed in Tables 2 and 3 and Fig. 4 and 5 are considered gratifying. In most cases 4 or more *reliable* signal parameters would be available for epicenter locations. This would suffice for estimating the 3 unknowns origin time, latitude and longitude for a fixed focal depth.

6 Robust earthquake location methods and results

For a long time it has been known that errors in earthquake arrival times follows a non-Gaussian distribution (Jeffreys, 1932). Consequently, least square estimation techniques (e.g., Geiger, 1910 and numerous modifications) cannot yield optimal hypocenter estimates (Buland, 1986). Still, least square algorithms remain the most commonly used method for locating seismic events. The reason for this is probably that the theory behind least squares is well known and that the method is computationally attractive. However, when applied to non-linear problems, convergence is not necessarily ensured unless a good trial solution is known.

Anderson (1982) considers a class of estimators particularly suitable for data sets with large errors. He suggested an iterative algorithm with weights dependent on "current" residuals to minimize the objective function. Sambridge and Kennett (1986) and Nelson and Vidale (1990) also investigated robust hypocenter location methods but used a grid-search technique to find the minimum of the objective function. Besides that grid-search methods are better suited for highly non-linear optimization problems, they are also useful for illustrating the "resolution" of the estimated epicenter. Buland (1976) made contour maps of the sum of squared residuals and also derived their relation to corresponding confidence regions assuming Gaussian errors. Prugger and Gendzwill (1988) produced similar maps using average absolute residuals. They recommended using the Simplex step algorithm (Nelder and Mead, 1965) to solve the non-linear minimization problem.

In our experiment, back-azimuth estimates were available from some 3-component stations so we also wanted to include these in the location scheme, that is, in addition to the P- and S-readings. The input data for our location algorithm thus consist of different kinds of physical quantities so it was necessary to define normalized residuals by dividing by a priori estimates of the standard error of each observation, i.e.,

$$r_i = \frac{do_i - dc_i}{\sigma_i}$$

where do_i and dc_i are observed and calculated data respectively, and σ_i is the corresponding standard error. The calculated residuals are functions of the hypocenter coordinates (latitude, longitude, depth and origin time), the coordinates of the observing station and the kind of observation (azimuth, or in case of arrival times a phase designation, see examples in Table 4).

Initial experiments with both L_2 (least squares) and L_1 (absolute errors) norms showed that a few large errors could heavily bias the epicenter estimate, i.e., pull it away from the "true" epicenter. Our next step was to try an objective function of the form

$$f(r) = \sum_i w_i \frac{r_i^2}{r_i^2 + 1}$$

(as compared to $\sum w_i r_i^2$ for the L_2 norm and $\sum w_i |r_i|$ for the L_1 norm). Here w_i are weights that depend on the confidence we have in each observation and the summation is over all observations (both arrival times and azimuths for all stations). This estimator is very similar, although not identical, to some of the estimators considered by Anderson (1982). The advantage of this objective function is that it is practically flat (insensitive) for $|r_i| > \; > 1$, while for $|r_i| < \; < 1$ it behaves like the L_2 norm.

The hypocenter location problem now becomes very non-linear as compared to least square methods and a grid search approach is necessary to find the global minimum of the objective function. As most of the events were explosions and the remaining earthquakes were relatively shallow (within the crust), we used a fixed zero focal depth and searched over a grid of latitude and longitude lines. An initial set of 51 x 51 points covering an area of about 1000 x 1000 km^2 surrounding the detecting stations proved sufficient for all the local events. For each grid point an additional search over time was performed to find the

50

best origin time. Typical execution times were about 1 minute per event on a SUN Sparc station. A simple crustal model consisting of two horizontal layers over a halfspace was used with travel times calculations for every point in the grid. Tabulated travel times could be used to save time, especially if more complex models were to be considered (see Nelson and Vidale, 1990). In the location experiment we presumed that the automatically picked P- and S-phases were the first arriving phase of each kind. Specific secondary phases like Pg and Lg (at distances beyond 200 km) are sometimes observed and can be allowed for in the location algorithm, but were not used in the automatic processing. Our observational data indicated that P-pickings were more reliable than S-pickings, so that the former were given greater weight (2.0 for P; 1.0 for S and P-azimuth). The a priori standard deviations were set rather high to compensate for the coarse initial grid: 2.0 sec for P, 3.0 sec for S and 15 deg for the P-azimuth.

The results presented here (Table 3) were computed with the rather coarse initial grid, but if desiered a more refined "final" hypocenter estimate could be found in several ways: (i) identify outliers given a cutoff criteria and proceed with one of the commonly used location programs (HYPO71 or variants hereof, e..g., Lienert et al, 1986), (ii) restart the search using a denser grid, or (iii) proceed with an iterative algorithm and the same objective function (convergence should not be a problem when sufficiently close to the global minimum).

Practical demonstrations of the above epicenter location method are illustrated in Figs. 6 and 7 and Table 4 for the two events in Figs. 2 and 3. The full scale test here was to locate 38 events using the signal parameters automatically derived at the Hub. The differences between the analyst derived locations (HYPO71) and ours have a standard deviation of 18 km in the south-north direction and 14 km in east-west (Table 3).

7 Discussion

We have here demonstrated automatic network operation in the sense that a daily bulletin can be produced which would not be much inferior to that of an analyst. With the data used the success rate of our automatic event analyser to extract reliable P- and S-arrivals was around 70-80 per cent for each station. This entails that only around 30 per cent of the processed events would have correct arrival times and phase identification for all contributing stations.

With more operational experience (and possibly system upgrading), the performance of the automatic analysis is likely to be improved. However, as we cannot safeguard against gross observational errors, a robust epicenter location scheme is required. The method introduced here fulfills such requirements even for rather adverse cases where faulty observations could reach nearly 50 per cent of the total (see Table 2).

The main results from this study is condensed in Figs. 5-7 and Table 2 and 3, but we would like to give a few comments on the somewhat problematic mining explosions in the Kiruna area. Firstly, Event 19 is interesting in view of the relatively large mismatch between the bulletin solution in the northern Bothnian Bay and ours. A comparison with the Helsinki bulletin gave that the latter was approximately correct, that is, a Kiruna mining explosion. The bulletin mislocation was simply due to the use of the Pg notation for some of the first arrivals. Another somewhat problematic Kiruna event was no. 23, where neither the bulletin nor our solution is particularly good. The advantage of the latter is that with our scheme for epicenter determinations we can obtain a visual measure of the epicenter resolution, as demonstrated in Figs. 6 and 7. In the latter case the resolution becomes relatively poor, particularly in the NW-SE direction (Fig. 6). In general, the NSN network geometry is far from ideal because it is (for geographical reasons) restricted to a very elongated area. For accurate locations of the many events outside the network area it is crucial to have good S-phase readings (Buland, 1976; Comberg et al, 1990).

52

The events in Table 3 are local in the sense that all station-epicenter distances are less than 750 km. In cases of regional and teleseismic events the above location scheme would be inconvenient, and should instead be used in combination with those presented by, for example, Bratt and Bache (1988), Cassidy et al (1989) and Ruud (1990).

Finally, we want to discuss our results here in the context of generalized seismological network operation. Firstly, in the current NSN operation event detection is a two-step process. A rather crude STA/LTA detector is used in the field, while the detector described in Paper 1 is used for extracting signal parameters from segmented waveform data at the Hub. The latter detector could naturally be installed at the individual stations in the field given sufficient CPU capacity. The advantage here is that for very many events it would suffice to transmit on a routine basis only parameterized (signal parameters) event data to the Hub.

We have earlier discussed a few "restart" schemes for more refined event locations. Better results here would be obtained if such undertakings were combined with reprocessing and reanalysis of the original records (e.g., see Roberts and Christoffersson, 1990). For example, given preliminary epicenter coordinates this information would facilitate pickings of individual P- and S-phases like Pg, Pn, Sg (Lg) and Sn, which in turn could help us to provide decent focal depth estimates (Ruud et al, 1988; Thurber, 1989). Further refinements would be feasible if access to a priori seismicity information, similar to the knowledge-based analysis system introduced for arrays (Bache et al, 1990; Bratt et al, 1990). An illustrative example here is the time-space stability of many of the Kiruna mining explosions (events 3,8,15,23,27,31 and 37 in Table 3).

The NSN network comprises relatively few stations (Fig. 1), while in operational terms we distinguish between a southern and a northern subnet. The rationale here is two-fold: namely, i) to facilitate the event association problem and ii) little overlap in event populations between the two subsets. In the latter case another example is that the event

overlap between the NORESS and ARCESS arrays (Fig. 1) is only about 10 per cent. The reason for this is that the numerous man-generated events are of ML magnitudes less than 2.0, and thus in general are not recorded at epicenter distances beyond 500 km (Paper 1; Suteau-Henson, 1991). Regarding event association, that is, the problem of determining which of the detected phases stem from a specific event, its severity increases with increasing station separations. For network subsets of aperture 3-500 km, event association is not much of a problem. For networks much larger than the NSN subdivision into several subsets of the mentioned size could well be done.

There is a growing interest to utilize 3C data more extensively in the seismological community. It is therefore interesting to investigate the importance of the additional information provided by the 3C stations compared to the single, vertical component (1C) stations. In this study we could not fully test performance differences between 3C and 1C stations since the analysed data were restricted to the NSN event selection based on 1C station detection. For this experiment most P- and S-arrival times could be picked relatively accurate for both type of stations. In a "true" detector environment, with many low SNR events, we would expect 3C stations to have better detection and time picking abilities than a single component station due to lower threshold for P-phase detection and because S-phase often are stronger on the horizontal components.

Regarding the use of azimuth information we found that when a sufficiently large number of stations and correct arrival times (at least 3 stations and 5 arrival times) were available the azimuth information did not contribute much to the epicenter location. However, azimuth is a crucial parameter when locating events for a single station and is also very important with two detecting stations. For high-frequency "local" signals, P-phases are not necessarily well polarized and in many cases the 3C stations failed to provide azimuth estimated (Table 2). Also with respect to P/S phase discrimination the results from the NSN network were less impressive than earlier results at NORESS (Paper 1). The

most likely reason for the deteriorated P-wave polarization is scattering (from P to surface waves) due to the very rugged topography near most of the NSN stations. This illustrates that polarization information can be difficult to utilize in an on-line detection environment.

The full advantage of 3C recordings is probably better realized in a post-processing stage when a preliminary event location is available. When an approximate arrival time is known more complex particle motion models can be introduced for wavefield decomposition analysis. This could enable us to identify secondary arrivals which are important for focal depth estimation.

8 Concluding remarks

The results of this study implies that seismic network operation in terms of daily bulletin generation to a large extent can be automated. This would enable the analyst to concentrate on more in-depth analysis of real earthquake recordings, which is a principal goal of the ISOP project. Today, it appears that far too much analyst effort is spent on analysis of local explosions which are of marginal scientific value.

Strictly speaking, the conclusions drawn here are restricted in the sense that they are based on our experience with recordings from the Norwegian Seismograph Network (NSN). To what extent our results applies to other seismic networks and stations sited in different tectonic environments remains partly an open question. However, based on our experience with analysis of various data we anticipate that similar results can be obtained at most networks by adjusting the detector parameter settings and by modifications of the associated decision rules.

Acknowledgments

References

Alsaker, A, L.B. Kvamme, R.A. Hansen, A. Dahle, H. Bungum (1991). The ML scale in Norway, Bull. Seism. Soc. Am., 81,. 379-398.

Anderson, K.R. (1982). Robust earthquake location using M-estimates, Phys. Earth Planet. Inter., 30, 119-130.

Bache, T.C., S.R. Bratt, J. Wang, R.M. Fung, C. Kobryn and J.W. Given (1990). The intelligent monitoring system, Bull. Seism. Soc. Am., 80, 1833-1851.

Baer, M. and U. Kradolfer (1987). An automatic phase picker for local and teleseismic events. Bull. Seism. Soc. Am., 787, 1437-1445.

Boschi, E., A. Basili, R. Console, F. Mele and G. Smriglio (1990). Seismological analysis with automatic processing for the Italian telemetered network. Publ. No. 518, Istituto Nazionale di Geofisica, Rome, Italy, 14 pp.

Boschi, E., D. Giardini and A. Morellie (eds.) (1991). Workshop Proceedings re MED-NET: The broad-band seismic network for the Mediterranean; Spec. Publ., Istituto Nazionale di Geofisica, Rome, Italy, 514 pp.

Bratt, S.R. and T.C. Bache (1988). Locating events with a sparse network of regional arrays. Bull. Seism. Soc. Am., 78, 780-798.

Bratt, S.R., H.J. Swanger, R.J. Stead, F. Ryall and T.C. Bache (1990). Initial results from the intelligent monitoring system, Bull. Seism. Soc. Am., 80, 1852-1873.

Buland, R. (1976). The mechanics of locating earthquakes. Bull. Seism. Soc. Am., 66, 173-187.

Buland, R. (1986). Uniform reduction error analysis, Bull. Seism. Soc. Am., 76, 217-230.

Båth, M. (1981). Earthquake magnitude -- recent research and current trends, Earth Science Reviews, 17, 315-398.

Cassidy, F., A. Christoffersson, E.S. Husebye and B.O. Ruud (1990). Robust and reliable techniques for epicenter location using time and slowness observations, Bull. Seism. Soc. Am., 80, 140-149.

Geiger, L. (1910). Herbsbestimmung bei Erdbeben aus den Ankunfzeiten, K. Gessel Wiss. Goett., 4, 331-349.

Gomberg, J.S., K.M. Shedlock and S.T. Roecker (1990): The effect of S-wave arrival times on the accuracy of hypocenter estimation, Bull. Seism. Soc. Am., 80, 1606-1628.

Havskov, J., L.B. Kvamme, R.A. Hansen and C.D. Lindholm (1992). The Northern Norway seismic network: Design, operation and results, Bull. Seism. Soc. Am., 82, in press

Jeffreys, H. (1932). An alternative to the rejection of observations. Proc. R. Soc. (London), Ser. A, 137: 78-87.

Jeffreys, H. (1967). Theory of Probability (3rd Ed.), Oxford Univ. Press, UK.

Li, Y. and C.H. Thurber (1991). Hypocenter constraint with regional seismic data: A theoretical analysis for the Natural Resources Defense Council Network in Kazakhstan, USSR.

Lienert, B.R., E. Berg and L.N. Frazer (1986). Hypocenter: An earthquake location method using centered, scaled and adaptively damped least squares, Bull. Seism. Soc. Am., 76, 771-783.

Masse, R.P. and W. Person (1991). Seismograph networks and the National Earthquake Information Center; In: E. Boschi, D. Giardini and A. Morelli: Workshop Proceedings re MEDNET: The broad-band seismic network for the Mediterranean; Spec. Publ., Istituto Nazionale di Geofisica, Rome, Italy, 514 pp.

Michaelson, C.A. (1990). Coda duration magnitudes in central California: an empirical approach, Bull. Seism. Soc. Am., 80, 1190-1204.

Nelder, J.A. and R. Mead (1965). A simplex method for function minimization, Computer J., 7, 308-313.

Nelson, G.D. and J.E. Vidale (1990). Earthquake location by 3-D finite-difference traveltimes, Bull. Seism. Soc. Am., 80, 395-410.

Prugger, A.F. and D.J. Gendzwill (1988). Microearthquake location: A nonlinear approach that makes use of a simplex stepping procedure. Bull. Seism. Soc. Am., 78, 799-815.

Roberts, R.G. and A. Christoffersson (1990). Decomposition of complex single-station three-component seismograms. Geophys. J. Int., 103, 57-74.

Roberts, R.G., A Christoffersson and F. Cassidy (1989). Real time event detections, phase identification and source location estimation using single-station three-component seismic data, Geophys. J. Int., 97, 471-480.

Ruud, B.O. (1990). Teleseismic epicenter locations from arrival times a regional networks. Geophys. J. Int., 100, 515-519.

Ruud, B.O., E.S. Husebye, A. Christoffersson and S.F. Ingate (1988). Event location at any distance using data from a single three-component station. Bull. Seism. Soc. Am., 78, 308-325.

Ruud, B.O. and E.S. Husebye (1992). A new three-component station detector and automatic single station bulletin production. Bull. Seism. Soc. Am., 82, in press.

Sambridge, M.S. and B.L.N. Kennett (1986). A novel method of hypocentre location, Geophys. J. R. Astr. Soc., 87, 679-697.

Suteau-Henson, A. (1991). Three-component analysis of regional phases at NORESS and ARCESS: Polarization and phase identification. Bull. Seism. Soc. Am., 81, 2419-2440.

Tarvainen, M. (1992). Automatic seismogram analysis: statistical phase picking and locating methods using one-station three-component data, Bull. Seism. Soc. Am., April 92.

Thurber, C.H., H. Given and J. Berger (1989). Regional seismic event location with a sparse network: Application to eastern Kazakhstan, USSR. J. Geophys. Res., 94, 17767-17780.

	Filter band (Hz)		
	1 - 4	4 - 8	8 - 16
STA window (sec) :	1.00	0.60	0.40
Step length (sec):	0.25	0.15	0.10
LTA delay (sec) :	15.00	9.00	6.00
Threshold_1 :	1.70	1.80	1.90
Threshold_2 :	2.55	2.60	2.75
Pc_min :	0.40	0.40	0.40
K-parameter :	4	4	4

Table 1. Most entries are self-explanatory and otherwise detailed in Paper 1. Step length or STA updating interval is 1/4 of STA window length. LTA delay is the time gap between the STA and LTA windows. The two thresholds are for linearly polarized (1) and for unpolarized (2) signals. Pc_min is a threshold for polarization (predicted coherence limit). K-parameter gives the minimum number of consecutive windows that must be triggered before the detection is accepted (duration limit).

STA	OP	RP	OS	RS	OAZI	RAZI
KMY	12	1	8	1	-	-
ODD1	12	2	9	0	-	-
EGD	24	6	14	2	-	-
BER	11	2	2	1	-	-
ASK1	25	8	16	4	16	4
SUE	25	1	21	1	-	-
HYA	24	2	18	2	-	-
FOO	6	0	6	0	6	1
FRO	6	0	6	0	-	-
MOL	16	5	11	0	-	-
NSS	4	1	3	2	-	-
MOR1	6	2	2	0	5	2
LOF	11	3	10	3	5	0
TRO	10	0	9	3	8	0
KTK1	10	0	10	3	-	-

Table 2. The Norwegian Seismograph Network (NSN) station listing. In the table the columns OP, RP, OS and RS give numbers of observed (O) and rejected (R) (during epicenter location) P- and S-pickings. The same applies to the two rightmost OAzi and RAzi columns conserning azimuth observations.

Table 3. Event tabulations and analysis results. The columns to the left give origin time, epicenter coordinates and focal depths as taken from the Bergen seismological bulletin for August 1991. The next three columns give the number of observing stations and the number of reported P- and S- arrival times. The slashes (B/A) separate reportings in the bulletin (B) and in the automatic detector log (A). The NA column indicates the number of reported azimuths. The next 3 columns give the differences between the bulletin listed origin times (dOT) and epicenter coordinates (dLat; dLong). The 3 rightmost columns (RP, RS and RA) give the number of P- and S-phase pickings and azimuth estimates which were rejected (neutralized) by our epicenter determination scheme. Note, when averaging the location errors, events no. 19 and 23 were deleted as obviously the bulletin solutions here are not very good (text). Likewise. dOT averaging was exclusive of events for which the bulletin gave focal depth in excess of 3 km -- we use zero depth as default value. In the bottom line, sums and averages are given for various parameters. The standard deviation in dLat and dLong were 0.18 and 0.14 respectively.

Table 3

No.	Day (Aug 91)	Origin Time	Lat (deg N)	Long (deg E)	H (km)	NSTA (B/A)	NP (B/A)	NS (B/A)	NA (A)	dOT (sec)	dLat (degN)	dLong (degE)	RP (A)	RS (A)	RA (A)
1	1	13:37:39.8	60.51	5.30	0	4/5	4/5	3/4	1	7.70	0.51	0.90	2	3	1
2	2	07:21:29.3	61.51	4.18	0	5/6	5/6	5/6	1	0.9	0.01	0.08	1	-	-
3	2	22:35:14.1	67.67	20.25	0	3/5	2/5	3/4	2	4.5	-0.13	-0.25	2	-	-
4	5	12:32:31.3	72.76	4.23	17	5/4	5/4	3/3	1	3.9	0.01	-0.07	-	-	-
5	6	13:13:30.8	58.22	6.27	0	6/7	6/7	4/5	1	2.5	0.02	-0.33	-	-	1
6	6	16:56:46.3	60.52	4.70	6	4/4	4/4	3/3	-	1.1	0.07	0.10	-	-	-
7	7	07:19:52.2	60.90	6.36	0	7/5	7/5	2/3	-	0.6	0.00	-0.04	-	-	-
8	7	22:37:51.1	67.86	20.12	0	3/3	3/3	3/3	2	-0.6	0.01	-0.38	-	-	-
9	8	07:14:13.2	60.35	5.13	0	10/9	10/9	6/6	2	0.6	0.00	-0.07	-	-	1
10	8	10:59:12.7	64.43	15.39	13	4/4	4/4	1/3	-	-3.1	-0.02	0.59	-	1	1
11	8	15:23:24.3	59.79	8.87	23	3/3	3/3	2/2	-	7.2	0.11	-0.53	1	-	-
12	9	13:26:25.0	60.71	5.58	0	6/5	6/5	5/2	1	-1.9	-0.14	-0.02	1	-	-
13	10	15:35:50.4	60.88	5.85	0	5/5	5/5	3/4	1	0.4	0.03	-0.05	1	-	-
14	11	22:07:47.2	60.38	1.95	-	7/7	7/7	7/7	2	1.1	-0.07	-0.15	-	2	1
15	12	22:34:03.6	67.83	20.07	0	3/3	2/3	3/2	1	-1.6	-0.12	-0.43	-	-	1
16	13	06:21:08.5	60.37	5.20	2	5/6	5/6	5/3	-	1.3	0.02	0.00	1	-	-
17	13	16:47:59.5	59.81	6.17	3	6/5	5/5	4/4	-	0.7	0.01	-0.03	-	3	-
18	14	14:00:16.2	62.26	7.28	13	6/4	4/4	6/3	3	2.0	-0.19	0.58	-	-	1
19	14	15:38:25.5	65.99	23.01	16	5/5	5/5	2/5	1	-14.5	-1.11	2.21	-	2	-
20	15	13:13:11.5	59.76	8.91	16	5/6	3/6	5/4	-	4.8	0.06	-0.29	4	-	1
21	16	07:33:35.4	60.29	5.43	16	4/4	4/4	2/2	-	2.3	0.09	-0.17	1	-	-
22	16	14:18:48.2	60.09	5.47	8	5/6	5/6	5/5	-	0.7	-0.01	-0.13	2	2	-
23	16	22:35:19.1	68.39	21.36	25	4/5	4/5	0/3	1	-6.0	-0.41	2.76	2	2	1
24	17	06:36:26.3	68.07	21.01	25	4/4	4/4	0/3	1	3.8	0.12	0.01	-	3	1
25	18	17:05:44.5	61.07	4.47	14	8/9	5/9	8/5	1	1.1	0.02	0.07	4	-	-
26	20	11:30:36.1	60.45	5.35	10	4/4	4/4	3/0	1	-1.0	-0.05	-0.05	-	-	-
27	20	22:35:25.1	67.62	20.49	0	3/3	2/3	3/2	2	-2.8	-0.38	0.01	1	1	-
28	21	05:11:56.1	60.70	5.58	3	6/5	5/5	6/2	1	1.7	0.00	0.08	3	-	1
29	23	04:07:47.4	58.88	5.77	0	12/9	8/9	10/8	2	3.4	0.18	-0.03	1	1	1
30	24	07:02:55.0	62.08	2.07	31	9/9	9/10	9/9	2	1.1	0.28	-0.28	1	-	-
31	27	22:34:44.1	67.83	20.14	0	3/3	2/3	3/3	2	-0.9	-0.07	-0.36	-	-	-
32	28	16:05:11.9	59.38	6.02	0	7/7	6/7	7/7	1	3.8	0.18	-0.38	-	-	-
33	28	16:09:14.7	60.89	5.86	0	5/5	5/5	2/4	1	0.6	0.04	-0.04	-	-	-
34	29	13:19:43.2	59.10	5.66	3	6/6	6/6	4/3	-	4.3	0.20	0.06	-	-	-
35	30	06:45:30.5	60.39	5.21	1	5/5	5/5	2/1	-	1.6	0.09	-0.09	2	2	-
36	30	09:31:39.4	60.38	5.26	1	7/7	7/7	4/5	0	1.3	0.09	-0.09	1	-	-
37	30	22:32:15.0	67.65	20.19	0	3/3	2/3	3/3	2	-3.8	-0.40	-0.11	1	-	-
38	31	15:53:13.6	60.37	4.97	1	5/6	4/6	3/4	1	3.1	0.17	0.57	2	2	-

Sum: NP(A),NS(A),NA,RP,RS,RA;

Average: dOT,dLat,dLong:

| | | | | | | | 202 | 145 | 40 | 1.1 | 0.02 | -0.03 | 33 | 23 | 7 |

Event 19

Origin time (sec) : -19.99
Latitude (deg N) : 67.10
Longitude (deg E): 20.80
Fixed depth (km) : 0.00

		Obs	Res	Wei
NSS	P	49.40	0.55	2.00
NSS	S	121.90	22.78	1.00
KTK1	P	16.50	-0.30	2.00
KTK1	S	45.00	1.35	1.00
TRO	P	24.00	0.17	2.00
TRO	S	58.50	2.69	1.00
TRO	Az	170.00	6.11	1.00
LOF	P	27.30	-1.00	2.00
LOF	S	74.90	11.35	1.00
LOF	Az	110.00	2.93	1.00
MOR	P	22.40	-0.24	2.00
MOR	S	60.10	6.34	1.00
MOR	Az	83.00	15.61	1.00

Event 25

Origin time (sec) : 43.36
Latitude (deg N) : 61.05
Longitude (deg E): 4.40
Fixed depth (km) : 0.00

		Obs	Res	Wei
ODD1	P	92.49	20.65	2.00
MOL	P	106.70	26.43	2.00
SUE	P	47.40	0.84	2.00
HYA	P	58.30	-1.02	2.00
HYA	S	70.80	-0.15	1.00
BER	P	68.78	10.72	2.00
EGD	P	28.94	-32.00	2.00
EGD	S	71.60	-2.16	1.00
ASK	P	55.82	-0.13	2.00
ASK	S	65.58	0.45	1.00
FRO	P	57.30	0.32	2.00
FRO	S	67.30	0.39	1.00
FOO	P	55.80	0.92	2.00
FOO	S	63.60	0.32	1.00
FOO	Az	241.00	31.30	1.00

Table 4. Listing of results from the of automatic processing of events 19 and 25 in Table 3. All times are in seconds relative to 15:39:00 for event 19 and 17:05:00 for event 25. Azimuths are in decimal degrees. The column labels "Obs" means observed values, while "Res" gives the residuals (observed - calculated). "Wei" are the weights assigned to each observation. For event 25 the outliers are ODD1 (P), MOL (P), BER (P), EGD (P), and FOO (Az), while for event 19 the NSS (S), MOR(S) and LOF(S) are outliers. The same events are shown in Figs. 3 and 4.
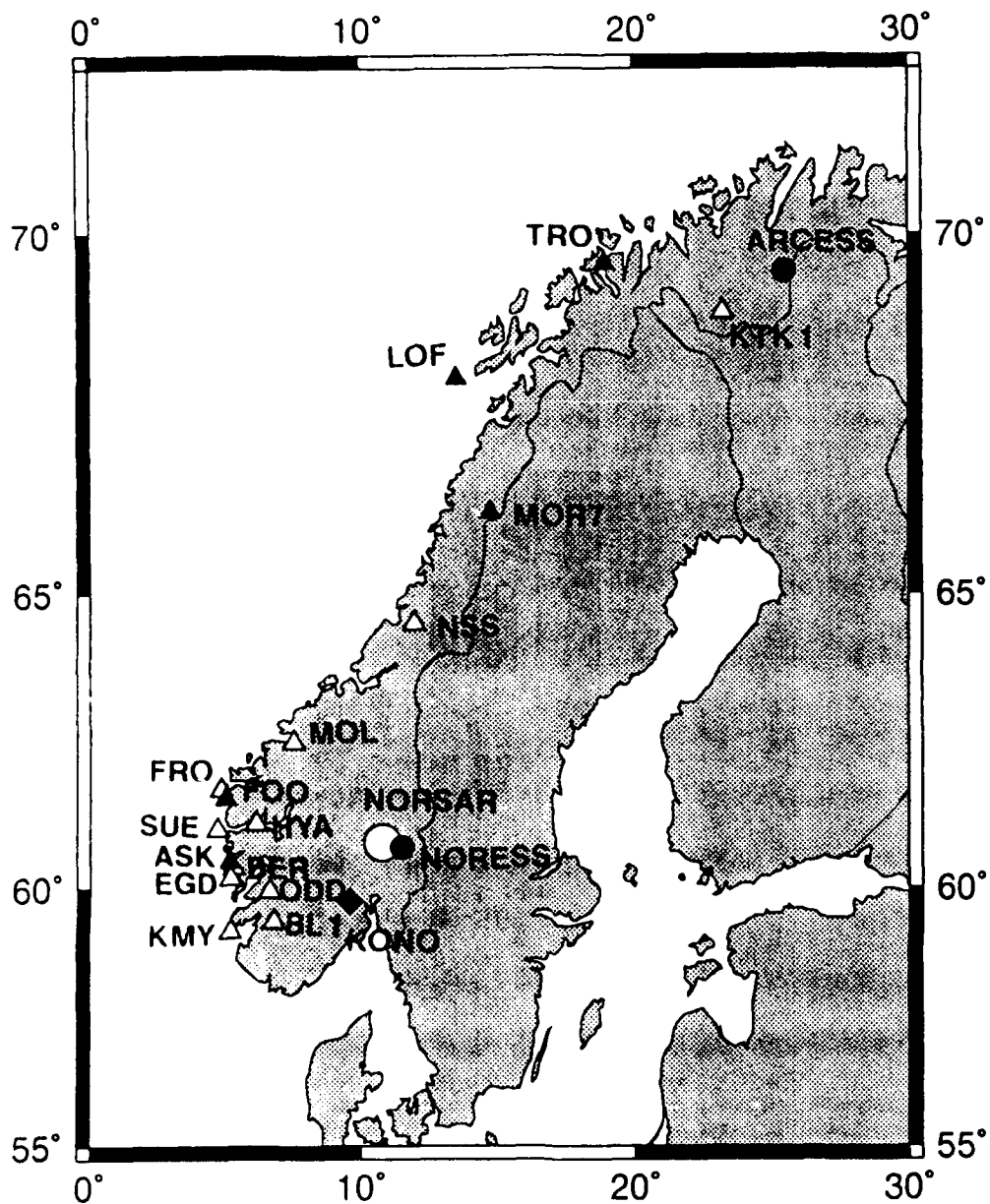
Fig. 1. The Norwegian Seismograph Network (NSN) as of August 1991. Differences in instrumentation are indicated: Open triangle - NSN single or cluster (MOR and KTK) of vertical component stations, filled triangle - NSN 3-component statio, filled diamond - KONO broad band 3-component instrument, open circle - NORSAR large aperture array of short period instruments. filled circles - small aperture arrays (NORESS and ARCESS) of short period vertical and 3-component instruments. KONO and the NORSAR, NOR-ESS and ARCESS arrays are not a part of NSN, although their data are accessible.
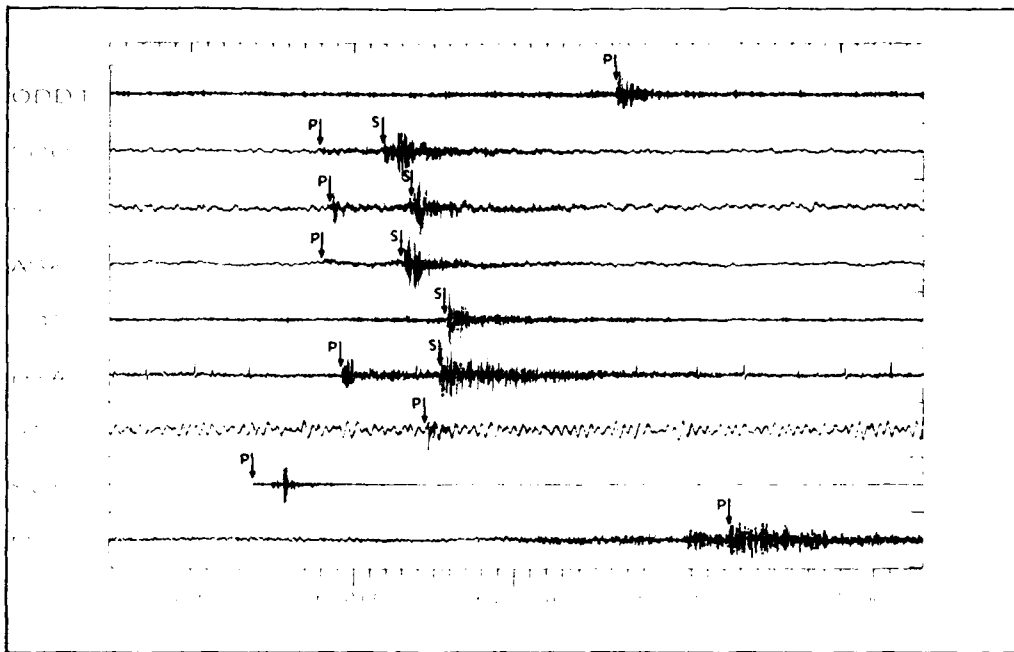
Fig. 2. Event records from the southern segment of the NSN -- Event 25 in Table 3. The time axis shows minutes and seconds after 17:00. Four of the P-phase pickings of the detector were rejected during the epicenter determination, namely, ODD, EGD, BER and MOL. This event illustrates typical problems in automatic phase pickings. For example, for ODD, BER and MOL the P-phase is missed by the detector and as a consequence the secondary, clear S-arrivals are denoted P-phases. For EGD, a weak preceding signal (outside plot at 17:05:28.9) triggers a "wrong" P-arrival while the S-phase is correctly detected and identified. For some reason the detector missed the S-phase for station SUE. Although four P-phase arrivals were rejected from the subsequent epicenter analysis, the difference relative to the bulletin solution is small indeed (see Table 3).
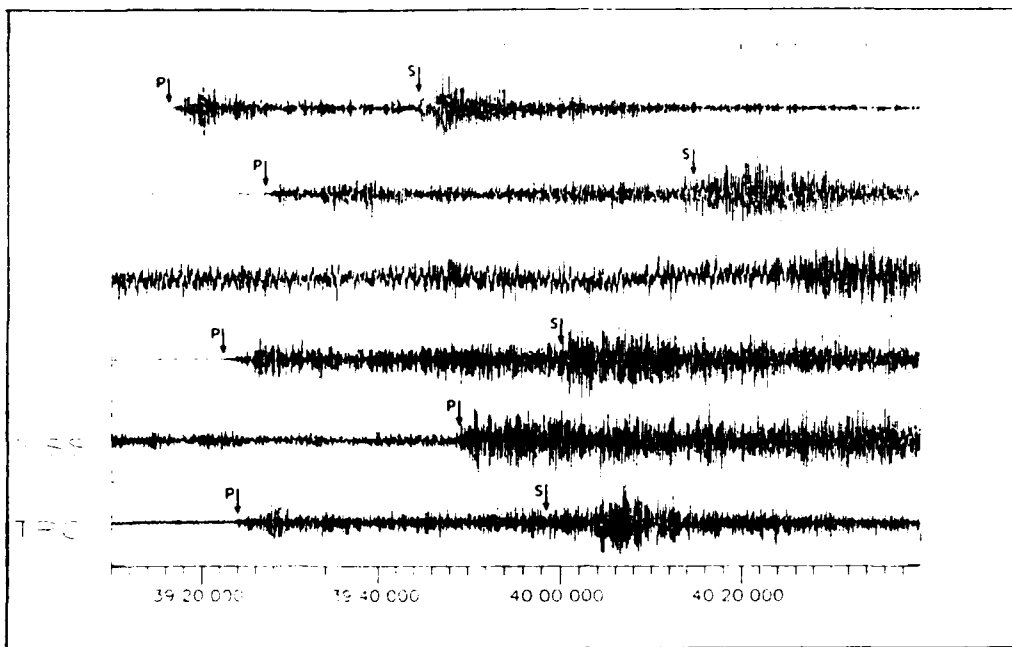
Fig. 3. Kiruna mining blast as recorded by stations in the northern segment of the NSN --
Event 19 in Table 3. The time axis shows minutes and seconds after 15:00. The P-phase
pickings coincide with those of the analyst, while some S-phase pickings are too late (NSS
outside plot at 15:41:01.9). The bulletin epicenter solution in Table 3 is erroneous relative
to ours and reflects the analyst decision to give a Pg-notation for all first arrivals and to
reject all S-phases.

P phase picking errors
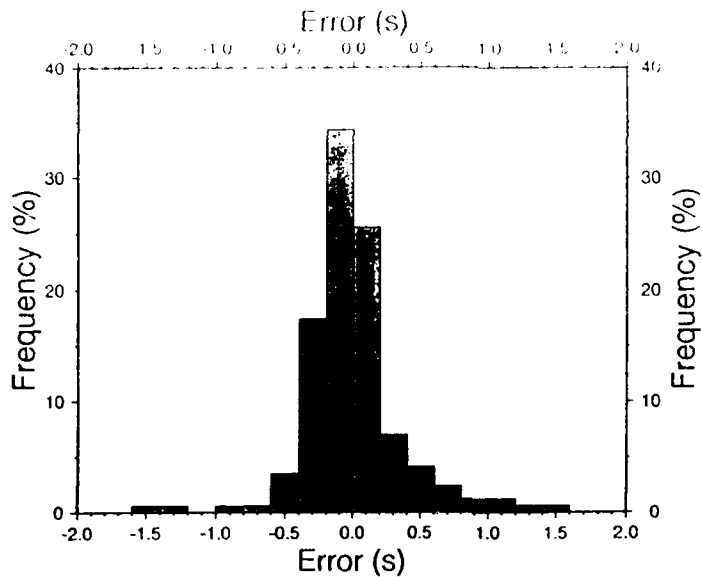
S phase picking errors
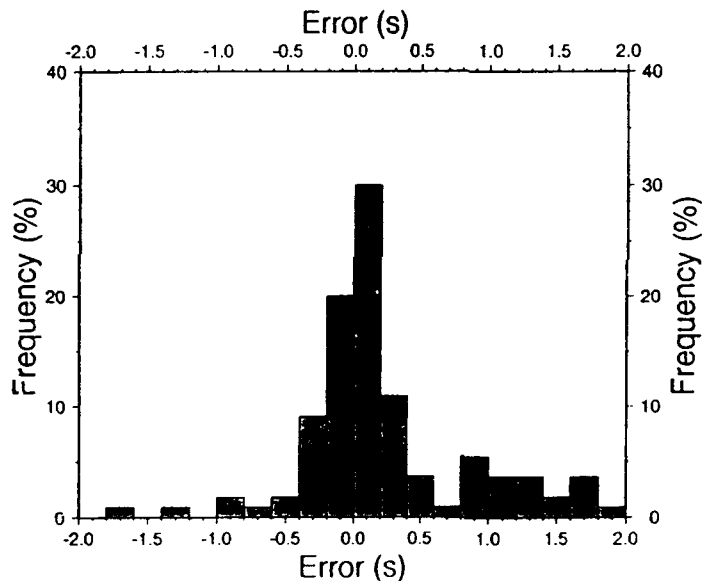
Fig. 4. Histogram plots of P- and S-residuals. The time residuals are the differences between the detector picked phase onset times and those picked by the analyst (in the bulletin). Errors due to wrong phase identification have been removed. The P-residuals consists of 173 observations including one outside the displayed interval. For S-pickings there are 120 observations with 10 outliers (all with positive residuals). The P-residuals are small and besides of the same order as reported by Baer and Kradolfer (1987) for similar experiments using recordings from the Swiss network. S-residuals are larger and exhibit a small positive bias of around 0.4 sec.

67
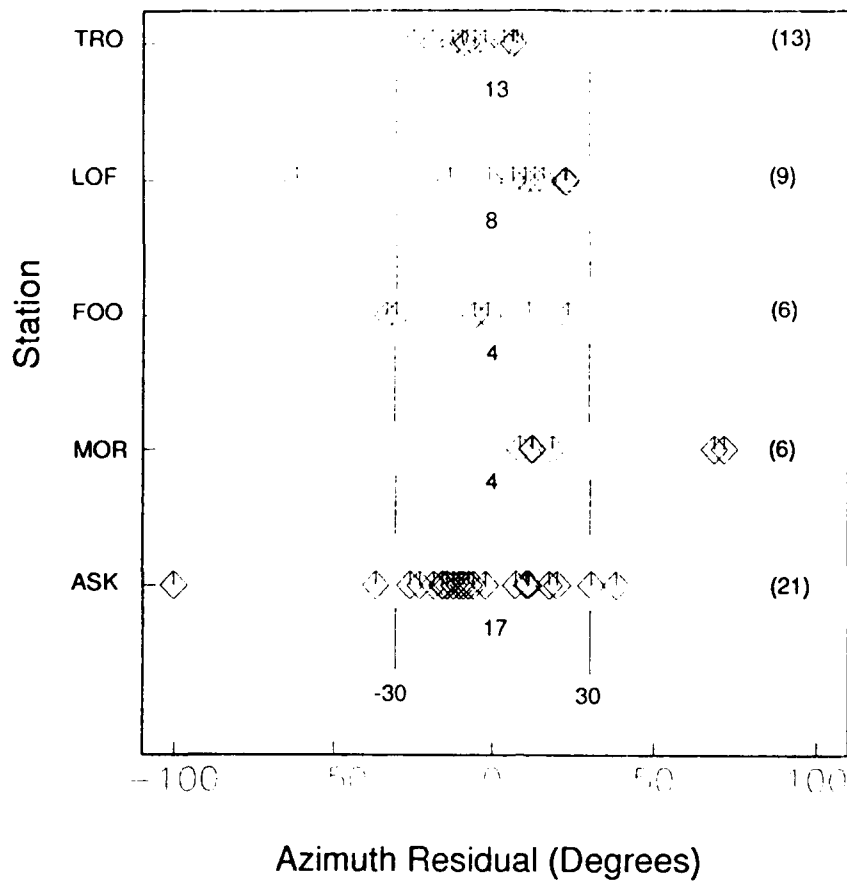
Fig. 5. Azimuth residuals for all 3C stations. The numbers to the right is the total number of observations and the number in the midle is number of observations with residual less than 30 degree. The residuals were calculated as the difference between the observed azimuth and the azimuth computed from the bulletin event locations. (As the residuals were calculated from a larger set of event, the total number of observations is different from Tables 2 and 3.)
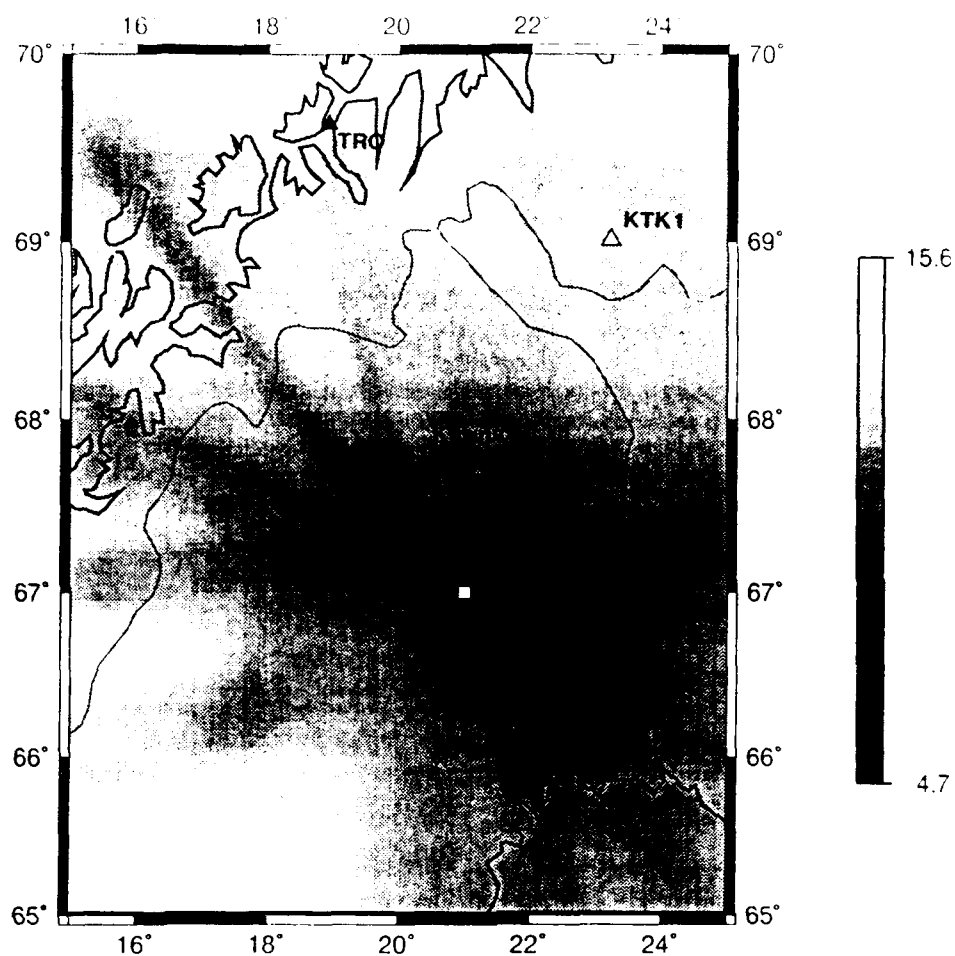
Fig. 6. Epicenter solution for Event 19 in Table 3 and with station records displayed in Fig. 4. The geometry of the recording stations gives relatively poor resolution in the NW/SE direction. Grid steps were 0.05 degrees in latitude and 0.10 degrees in longitude. The greyshades shows the value of the objective function (eq. 2) for fixed zero depth and for the best origin time at each grid point.

Fig. 7. Epicenter solution for Event 25 in Table 3 and with station records displayed in Fig.
3. The network geometry is relatively symmetric for this event, hence a more circular res-
olution area. Grid steps were 0.05 degrees in latitude and 0.10 degrees in longitude. The
greyshades shows the value of the objective function (eq. 2) for fixed zero depth and for
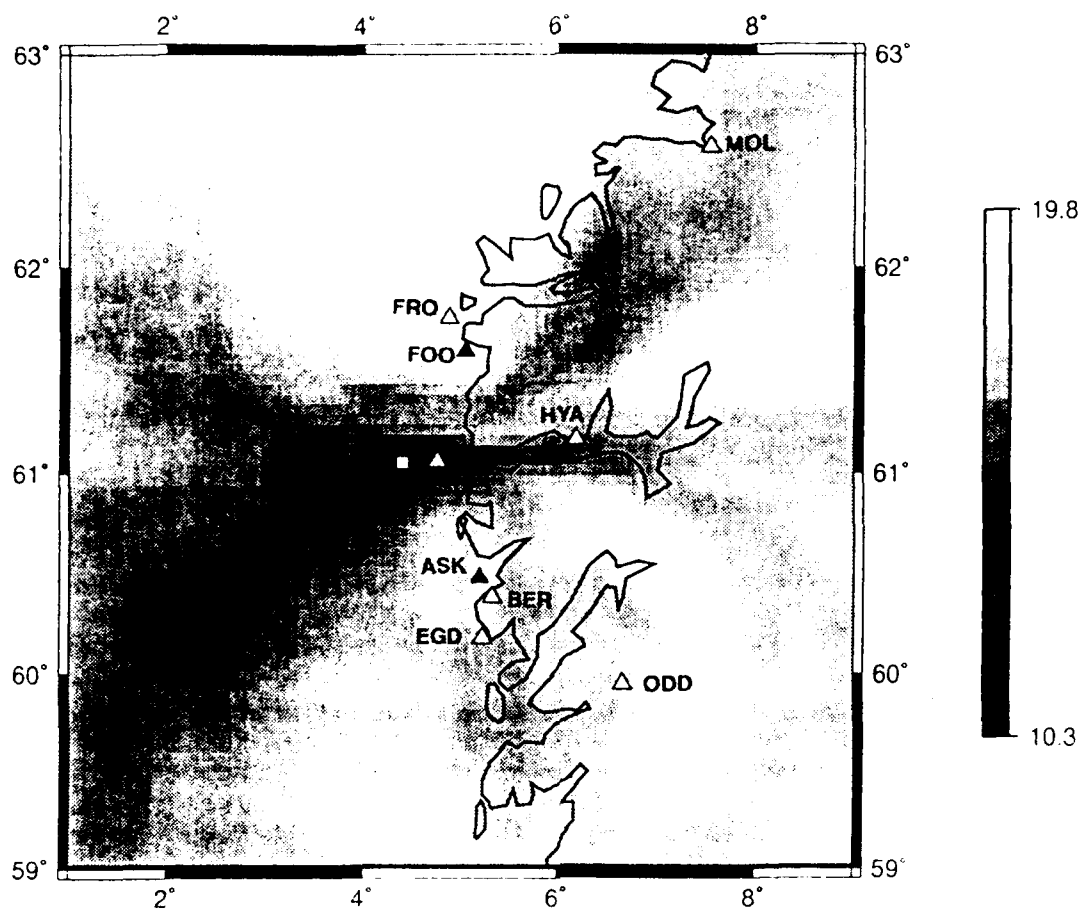the best origin time at each grid point.

On crustal, short-period Rg-propagation using array records from 4 continents

B.O. Ruud[1], E.S. Husebye[2] and R.S. Hestholm[3]

[1] Dept. of Geology, Oslo University, Oslo, Norway
[2] NTNF/NORSAR, Kjeller, Norway
[3] IBM Bergen Scientific Centre, Bergen, Norway

Abstract

Using fundamental model Rayleigh (Rg) recordings from seven arrays on four continents, we have explored structural properties in the respective siting areas through inversion of Rg phase velocity dispersion characteristics. The models used were one and two layers over a halfspace with shear velocities and layer thickness as unknowns. In the latter case, layer thicknesses were fixed at 0.5 and 1.0 km, respectively. The estimated halfspace S-velocities were remarkably consistent between the arrays with an average value of 3.55 $\pm$ 0.03 kms^{-1}. Likewise, in the case of the one-layer model, the average S-velocity was 2.87 $\pm$ 0.07 kms^{-1} and thus also rather consistent. However, estimated layer thicknesses ranged from 0.12 km (Yellowknife) to 1.6 km (Alice Springs). A comparison of the one-layer and two-layer model results implies that layer thicknesses and corresponding shear velocity are coupled. For a better physical insight into Rg propagation in complex media, 2D finite difference synthetics were computed. Inhomogeneous media were described by 0-th order von Karman functions (self-similar). In the latter case, S-scattering wavelets would intefere with the Rg wavetrain and thus reduce the accuracy of the phase velocity measurements, especially at short periods. Finally, excitation of Rg waves drops sharply for focal depths below 2-3 km.

1 Introduction

In a previous paper we discussed and demonstrated the usefulness of using short-period fundamental mode Rayleigh (Rg) waves as a tool for mapping upper crustal structures. The observational data were local explosion recordings from 15 NORSAR subarrays (aperture ca 7 km) located in SE Norway (Lokshtanov et al, 1991). In this study we report on a similar undertaking using local seismogram records from 6 other arrays located on 4 continents (Table 1). Traditionally, seismic reflection and refraction profiling are used for crustal mapping, but none of these techniques are particularly effective as regards the uppermost 2-3 km of the crystalline crust. Not surprisingly, some investigators have used the Rg part of the records for detailed mapping of the upper crustal layering along such profiles (e.g., MacBeth and Burton, 1985, 1986; Reiter et al, 1988; and Saikia et al, 1990). A drawback with this kind of surveys is the high cost of the field work in contrast to high-quality recordings from stationary arrays which are easily available and free of charge.

In this study, upper crust structural information bearing on the respective array sites are derived by inversion of frequency-dependent Rg phase velocity observations. Computational details on the dispersion analysis and inversion formalism used are given in the Lokshtanov et al (1991) paper and will not be repeated here. Furthermore, as we are dealing with Rayleigh wave observations in different geological environments, relative Rg excitation and propagation efficiency are explored through synthetic seismogram analysis. In this respect, also heterogeneous or random scattering media would be considered.

2 Observational data, their analysis and results

Our observational data stem from six small-to-medium sized arrays on 4 continents, namely, ARCESS (ARA0, Norway), Eskdalemuir (EKA, Scotland), GERESS (GEC2, Germany), Gauribidanur (GBA, India), Alice Springs (ASAR, Australia) and Yellowknife

(YKA, Canada). For the sake of completeness, we have included the results from the NORESS (NRAO, S. Norway) already published by Lokshtanov et al (1991). The necessary technical details are given in Table 1, including the number of earthquake/explosion recordings used for the individual arrays. Representative waveform records are shown in Fig. 1.

As is well known, crust and upper mantle structural information can be derived from Rayleigh wave dispersion analysis. The standard procedure here is first to extract dispersion information, that is, phase and/or group velocities and then solve the inverse problem in terms of medium structural parameters. The structure is represented through a stack of uniform layers and the model parameters introduced in the inversion formalism are compressional and shear wave velocities, layer densities and thicknesses. Further details in Lokshtanov et al (1991), hereafter referenced as Paper 1.

A conventional f-k technique was the principal tool in the dispersion analysis. Signal power was extracted as a function of phase velocity for a given frequency and azimuth, as illustrated in Fig. 2. The scatter in the observations is quite moderate, as also experienced in our Rg dispersion analysis for the NORSAR subarrays (Paper 1). Hence, 2-3 events for each array appear adequate for dispersion estimates which are shown in Fig. 3.

Our inversion algorithm is limited to models with constant physical parameters within horizontal layers, while in the real crust this assumption is likely to be only approximately valid. Also, the limited bandwidth of the observations (typically 0.6 - 1.8 sec), the smoothness of the dispersion curves and the absence of higher mode Rg waves imply that we cannot resolve more than 2-3 model parameters. Hence we have restricted our inversion experiments to two models, each having three free parameters. These unknowns are shear velocities and/or layer thickness, while densities are fixed and P and S velocities are coupled through a Poisson ratio of 0.25. Model 1 consists of a single layer over a halfspace with the two shear velocities and layer thickness as unknowns. Model 2 consists of two

73

layers (thicknesses 0.5 and 1.0 km) over a halfspace and the three shear velocities are the free model parameters.

Model 1: One layer over halfspace

The β_2 estimates of S-wave velocities in the upper crust (half-space equivalent) are remarkably consistent, varying from 3.44 kms^{-1} (YKA) to 3.68 kms^{-1} (ASAR) or by 7 per cent (details in Table 2 and Fig. 4a). The exception here is EKA at 3.10 kms^{-1} which was expected in view of its siting on sedimentary rocks. The β_1 estimates, representative for the top crustal layer, are also rather consistent, varying from 2.59 kms^{-1} (EKA) to 2.96 kms^{-1} (ASAR), or by 13.5 per cent. The top layer thicknesses range from 0.12 km (YKA) to 1.6 km (ASAR) and thus vary considerably. The latter (ASAR) is not directly comparable to the other arrays, since the observations are confined to relatively long wavelengths. Layer thickness in the range 0.5-1.0 km are most common for the siting areas and frequency ranges considered.

Model 2: Two layers over halfspace

For this model the layer thicknesses were fixed at respectively 0.5 and 1.0 km, so here the unknowns were restricted to layer and half-space shear velocities and subjected to the constraint that $\beta_1 \leq \beta_2 \leq \beta_3$. The half-space velocities (β_3 estimates) are very similar, as seen from Table 2 and Fig. 4b. For those arrays with relatively thin Model 1 layer thicknesses (ARAO, EKA, GBA and YKA), the layer 2 velocities (β_2 estimates) are less than 10 per cent below their respective half-space velocities. For NRAO and GBA having relatively large Model 1 layer thicknesses, the β_1 velocities have been lowered in comparison to Model 1. The overall model fit parameter σ (also given in Table 1) is small for all arrays for both Model 1 and 2, thus implying a good fit between observations and derived model parameters. However, model resolution is somewhat poor in particular for ASAR, which in turn reflects lack of short wavelength observations.

3 Synthetic Rg modelling

The Models 1 and 2 above are homogeneous models in the sense that small-scale velocity perturbations are not considered. Both tomographic and scattering studies aim at mapping such heterogeneities, which naturally are frequency dependent. Typical "scattering" medium parameters like P- and S-velocities at 1 Hz for the crust are RMS fluctuations in the range 2-6 per cent and correlation distances in the range 2-20 km (Wu and Flatte, 1988; Charette, 1991). Typical correlation functions describing such media are of the Gaussian, exponential or the von Karman type. The latter can describe self-similar media, by which is meant that the extent of velocity perturbations, calculated over equal logarithmic intervals of wave number, remains constant over a range of scale lengths (Frankel and Clayton, 1986). In order to provide a better understanding of Rg propagation in complex media, we have calculated synthetic seismograms for a set of homogeneous and inhomogeneous models. The technique used is that described by Hestholm et al (1992) that is, 2-dimensional (2D) finite difference solutions of the elastic wave equation. In cases of inhomogeneous upper crust media, we have used exclusively 2D von Karman functions. As mentioned, it is considered unrealistic that the upper crustal low velocity layer (LVL) should have a uniform thickness, so for some models a corrugated interface was introduced in the form of a 1D von Karman function. Details on the various models considered are given in Table 3. Note that only P-type sources are used, as almost all Rg observations stem from explosions close to the surface. The motivation for using Rg synthetics was as follows:

- How well do we recover model parameters when inverting the synthetic records in the same manner as the real ones.

- The "response" of the Rg waves to model heterogeneities.

- Rg excitation as a function of focal depth; this problem is of interest in the context seismic source identification as explosions are confined at most to 1-2 km depths.

Below we present results pertaining to the above class of problems with basis in synthetic seismograms, a few of which are shown in Fig. 5 (Models 2, 3, 4) and Fig. 6 (Model 2).

Inversion of synthetic seismograms

From synthetic seismograms as exemplified in Fig. 5, we estimated Rg phase velocities and then inverted in order to retrieve the original model parameters. The outcome of this experiment for Model 2 (Table 3) is included in Table 2 for the distance range 30-60 km and depth 2 km. The differences in measured synthetic phase velocities compared to theoretical model values amounts to maximum 0.1 kms^{-1}. At shallow depths (1-2 km), the Rg fundamental mode would be dominant over the higher modes for entire peiord range considered here (e.g., see Panza et al, 1973), so any bias effect in phase velocity measurements is likely to be small. Concerning observational data, standard practice is to average phase velocity measurements between events as actually done here and also in Paper 1.

The above synthetic experiment has been instructive as it demonstrated that Rg phase velocity inversion provides robust estimates of top crust structural parameters. Also, there is obviously a trade-off in the estimate of LVL thickness and corresponding shear velocities at least for observational bandwidths available to us.

Rg wavetrain complexities

Instructive examples are shown in Fig. 5, where synthetics in two different passbands are shown for Models 2, 3 and 4 in Table 3. At relatively low frequencies (0-2 Hz) the Rg wavetrain is almost undeformed even when comparing Model 2 and 4 synthetics. However, at higher frequencies (unfiltered traces) the P-to-S and S-to-S first and higher order scattering contributions tend to mask the Rg wavetrain. Only the Airy-phase arriving at ca 25 sec remains clearly discernible. For Model 5 (synthetics not shown) these effects are even more pronounced. The Airy phase (period ca 1 sec) dominates our synthetics which

is typical for such models. Naturally, epicenter distance ranges are of importance, as for example ASAR at 450 km (Table 1) only records the long period part of the Rg (1.7-4.5 sec). The other extreme is YKA at 12-65 km, where Rg periods down to 0.3 sec are recorded. In view of our synthetics, this would imply that the amount of scatters in top crust near YKA must be moderate, that is, must be less than the RMS of 4 per cent presumed for Model 4.

For most of the arrays, the source distance range is 60-200 km and the corresponding Rg period range is 0.7-1.7 sec. For distances up to ca 100 km interference from S-scattering wavelets may interfere strongly with the Rg wavetrain. The main effect of upper crust heterogeneities appears to be to attenuate the Rg over large distances. For example, the NORESS array, located in hilly country, hardly records Rg beyond 100 km. while ARCESS records Rg out to ca 300 km. From Sweden Båth (1975, 1982) reports Rg out to 600 km. Very efficient topography related P-to-Rg scattering has been reported by Bannister et al (1990). Our synthetics were computed without incorporating intrinsic attenuation in the models and are not aimed at addressing this problem. On the other hand they illustrate that complex media (Models 3 and 4) may give rise to mode conversion and other scattering effects.

Rg excitation as a function of depth

The results in Fig. 5 were obtained for a fixed source depth at 2 km. Moving the source depths to 4 and 6 km, respectively, had rather profound effects on the Rg excitation efficiency as shown in Fig. 6. Essentially, for depths below 2 km very, very little Rg excitation takes place in the 0.5 - 2.0 sec signal band. In other words, Rg observations imply that the source must be very shallow. The array data used in this study stem from chemical explosions near the surface, except those from the Alice Springs array. In the latter case, earthquake rupturing of the free surface took place.

4 Discussion

In this study we have used Rg recordings from seven arrays located on four continents to explore structural inhomogeneities in the uppermost crust in their respective siting areas. The common result feature is the existence of a low-velocity layer (LVL) in the uppermost part of the crust. This may to some extent be an artefact of the inversion models used; we have not considered models with gradual velocity increases in layer(s) over a halfspace. Anyway, the shear-wave estimates for the halfspace are in average 3.55 kms^{-1} and remarkably consistent between the widely separated arrays (details in Table 2). EKA is exceptional in this regard (3.10 kms^{-1}), which is attributed to its siting on sedimentary rocks. The shear velocity within the presumed LVL is reasonably consistent (Table 2) and in average 2.87 kms^{-1}. Estimated layer thicknesses vary considerably, being thin for YKA (0.12 km) and ARAO (0.45) and very thick for ASAR (1.6 km). We have also estimated shear velocities using a model with fixed layer thicknesses over a halfspace. The results here (Table 2) demonstrate that LVL thickness(es) and corresponding shear velocities are not well resolved.

The observational data, that is, Rg phase velocity dispersion curves, vary somewhat from one event to another, hence averaging over a few events was performed. The reason for this is attributed to interferences from S-scattering wavelets. This has been visualized through synthetic seismogram analysis using a suite of homogeneous and inhomogeneous structural models (Table 3). It has not been possible to mimic extreme observational features like the vanishing of Rg on one sensor while another one 500 to 1000 m away exhibits clear Rg phases. Also, an LVL model would imply the existence of a clear Airy phase with typical features like the synthetics displayed in Fig. 5. Observationally, the Rg waveform is more complex (seldom very clear Airy phases), which may reflect the effects a gradual velocity increase in the uppermost crust or interferences from S-scattering wavelets.

The main result of this study is that a low-velocity layer appears to exist in the uppermost part of the continental crust and that this is a global phenomenon. A common physical explanation is that of a relative abundance of cracks near the surface as well as a water content that is relatively high in the uppermost 1-2 km of the crust (e.g., see Fritz and Frape, 1987). This provides a mechanism for lowering seismic velocities. Results of a laboratory study of such problems have been reported by Stesky (1985), who found that fractures in rocks under confining pressures up to 200 MPa decreased P- and S-velocities on the order of 10-20%. The effect was greater at lower pressures, with higher averaged numbers of fractures, and in rocks containing a lower microcrack porosity. Although petrological factors are claimed to be important on the basis of Rg studies in mainly sedimentary rock environments (MacBeth and Burton, 1986, 1987; Saikia et al, 1990, among others), this is not obvious from our results stemming from Rg observations in crystalline rock environments (except EKA).

Finally, we want to comment on the practical aspects of our results. Clearly, a pronounced LVL on top of the crust would affect the waveform of high-frequency P- and S-waves propagating through such a layer. For example, Lokshtanov et al (1991) demonstrated that more consistent slowness estimates for P were obtained if the LVL effect was taken into account. S-waves having relatively short wavelengths are likely to be affected even more by such a low-velocity layer, which observationally is manifested by rather complex particle motion patterns (Roberts and Christoffersson, 1990).The observational existence of Rg waves implies that the source depth should be less than say 2-3 km (see Fig. 6). Thus in many contexts, Rg observations can be used to discriminate between man-made explosions and real earthquakes (Kafka, 1990). In practice, this would imply that more effective means for extracting Rg parameters from the seismic records need to be developed.

5 Concluding remarks

Using Rg recordings from seven arrays on four continents, we have demonstrated that an uppermost crust low-velocity layer appears to be a global continental phenomenon. The halfspace average shear velocity of 3.55 kms^{-1} is remarkably consistent among the arrays and the same applies roughly to the LVL shear velocity average of 2.87 kms^{-1}. However, the LVL thicknesses vary considerably, which to some extent may reflect poor resolution for this parameter in the observational data. Through synthetic seismogram analysis, we have demonstrated that structural inhomogeneities, modelled as a (self-similar) von Karman medium, could to some extent mask the Rg wavetrain through shear wave scattering contributions. For events with focal depths exceeding 2-3 km, Rg excitation would be minimal, and thus Rg observations have the potential of being a powerful earthquake/explosion discriminant for epicentral distances of a few hundred kilometers. The existence of the LVL naturally contributes to the complexity of local seismogram records where high signal frequencies (>4 Hz) are dominant.

6 References

Bannister, S.C., B.O. Ruud and E.S. Husebye (1990): Teleseismic P-coda analyzed by three-component and array techniques, Bull. Seism. Soc. Am., 80, 1969-1986.

Båth, M. (1975): Short-period Rayleigh waves from near-surface seismic events, Phys. Earth Planet. Inter., 10, 369-376.

Båth, M. (1985): Superficial granitic layering in shield areas, Tectonophysics, 118, 75-83.

Charette, E.E. (1991): Elastic wave scattering in laterally inhomogeneous media, Ph.D. thesis, MIT, Cambridge, MA, USA, 222 pp.

Flatte, S.M. and R.S. Wu (1988): Small-scale structure in the lithosphere and asthenosphere deduced from arrival time and amplitude fluctuations at NORSAR. J. Geophys. Res., 93, 6601-6614.

Frankel, A. and R. Clayton (1986): Finite difference simulations of seismic scattering: implications for the propagation of short-period seismic waves in the crust and models of crustal heterogeneity, J. Geophys. Res., 91, 6464-6489.

Fritz, P. and S.K. Frape (eds.) (1987): Saline water and gases in crystalline rocks, Spec. Pap. Geol. Ass. Can., 33, 259 pp.

Hestholm, S., B.O. Ruud and E.S. Husebye (1992): Synthesizing 2D wave propagation in a heterogeneous lithosphere using finite difference techniques, ms in preparation.

Kafka, A.L. (1990): Rg waves as a depth discriminant for earthquakes and explosions in New England, Bull. Seism. Soc. Am., 80, 373-394.

Lokshtanov, D.E., B.O. Ruud and E.S. Husebye (1991a): The crustal transfer function in seismic 3-component slowness estimation, Geophys. Res. Lett., 18, 1393-1396.

Lokshtanov, D.E., B.O. Ruud and E.S. Husebye (1991b): The upper crust low velocity layer; a Rayleigh (Rg) phase velocity study from SE Norway, Terra Nova, 3, 49-56.

MacBeth, C.D. and P.W. Burton (1985): Upper crustal shear velocity models from higher mode Rayleigh wave dispersion in Scotland, Geophys. J.R. astr. Soc., 83, 519-539.

MacBeth, C.D. and P.W. Burton (1986): Propagation of 0.7-2.5 Hz Rayleigh waves in Scotland, Geophys. J.R. astr. Soc., 84, 101-120.

Panza, G.F., F.A. Schwab and L. Knopoff (1973): Multimode surface waves for selected focal mechanisms. I. Dip-slip sources on a vertical fault plane, Geophys. J.R. astr. Soc., 34, 265-278.

Reiter, E., M.N. Toksoz and A.M. Dainty (1988): Influence of scattering on seismic waves: velocity and attenuation structure of the upper crust in southeast Maine, Report AFGL-TR-88-0094, Air Force Geophys. Lab., Hansom AFB, Massachusetts. ADA199131

Roberts, R.G. and A. Christoffersson (1990): Decomposition of complex single-station 3-component seismograms, Geophys. J. Int., 104, 22-29.

Saikia, C.K., A.L. Kafka, S.C. Gnewuch and J.W. McTigue (1990): Shear velocity and intrinsic Q structure of the shallow crust in southeastern New England from Rg wave dispersion, J. Geophys. Res., 95, 8527-8541.

Stesky, R.M. (1985): Compressional and shear velocities of dry and satured jointed rock: a laboratory study, Geophys. J.R. astr. Soc., 83, 239-262.

Toksoz, M.N., B. Mandal and A.M. Dainty (1990): Frequency dependent attenuation in the crust, Geophys. Res. Lett., 17, 973-976.

Array	Lat. (deg)	Long. (deg)	Geol. Siting	Source	Ranges (km)	(deg)	Rg-Periods (sec)
NORESS-NRAO (S. Norway)	60.74N	11.54E	Precambrian Granite-gneiss	1 EX	34	314	0.7-1.5
ARCESS-ARAO (N. Norway)	69.53N	25.51E	Precambrian Gabbro	2 EX	170-190	83-96	0.65-1.70
GERESS-GEC2 (Bavaria, Germany)	48.84N	13.70E	Precambrian Granite-gneiss	4 EX	70-90	130-325	0.6-1.4
Eskdalemuir-EKA (Scotland)	55.38N	3.13W	Silurian shales	3 EX	60	279	0.6-21
Garibidinaur-GBA (India)	13.60N	77.44E	Archean gneiss	3 EX	110-215	125-330	0.8-2.0
Yellowknife-YKA (NW Canada)	62.49N	114.61W	Archean gneiss	2 EX	12-65	90-300	0.3-2.0
Alice Springs-ASAR (C. Australia)	23.67S	133.90E	Precambrian	2 EQ	450	6-7	1.7-4.5

Table 1. Location of the arrays used in this study. Brief information on geological siting and the events analyzed are given (EX = explosion; EQ = earthquake). Distance ranges of the events are given in km and azimuth range in degrees.

Array	One layer model				Two layers model			
	β_1 (km/s)	h_1 (km)	β_2 (km/s)	σ	β_1 (km/s)	β_2 (km/s)	β_3 (km/s)	σ
NRA0	3.02	1.07	3.52	0.0014	2.80	3.36	3.59	0.0003
ARA0	2.69	0.45	3.65	0.0006	3.02	3.50	3.62	0.0019
GEC2	2.93	1.02	3.54	0.0012	2.59	3.35	3.63	0.0018
EKA	2.59	0.71	3.10	0.0028	2.41	3.09	3.12	0.0053
GBA	2.86	0.76	3.51	0.0238	2.57	3.52	3.52	0.0364
YKA	2.81	0.12	3.44	0.0005	3.30	3.38	3.42	0.0011
ASAR	2.96	1.60	3.68	0.0275	2.91	2.91	3.70	0.0320
SYN	2.68	1.23	3.43	0.0062	2.51	2.88	3.48	0.0382

Table 2. Results from inversion of dispersion data. β is S-wave velocities and h is layer thickness. For Model 2 the layer thicknesses were fixed to $h_1 = 0.5$ km and $h_2 = 1.0$ km. σ is a data misfit function defined as $\sigma = 1000 \cdot \sum_{i=1}^{n} (v_i^{-1} - u_i^{-1})^2$ where v and u are observed and calculated phase velocities, respectively and n is the number of observations. In the last line (array = SYN) results of analysis and inversion of the synthetic data are shown.

Synth. model	Model type	Model dist.	Source		Basic model			von Kármán medium		
			type	depth (km)	β_1 (km/s)	h_1 (km)	β_2 (km/s)	ν	a (km)	rms
1	h.space	no	P	2/4/6	3.55	-	-	-	-	-
2	LVL	no	P	2/4/6	2.82	1.4	3.55	-	-	-
3	LVL	CI	P	2/4/6	2.82	1.4	3.55	0.5	10	0.1km
4	LVL	RM	P	2/4/6	2.82	1.4	3.55	0.0	5	4%
5	LVL	Ani.	P	2/4/6	2.82	1.4	3.55	0.0	5/1	4%

Table 3. Summary of the models used for computation of finite difference synthetics. In the column "Model disturbance" CI means corrugated interface generated by 1D randomization of layer thickness using a von Karman correlation function with indicated parameters (order, correlation distance, and rms variation). RM means random media (velocity variations) in the LVL with given correlation function. "Ani." is for a model with "apparent anisotropi", that is, different correlation distances in the horizontal and vertical direction. (Results of this last model is not shown here).
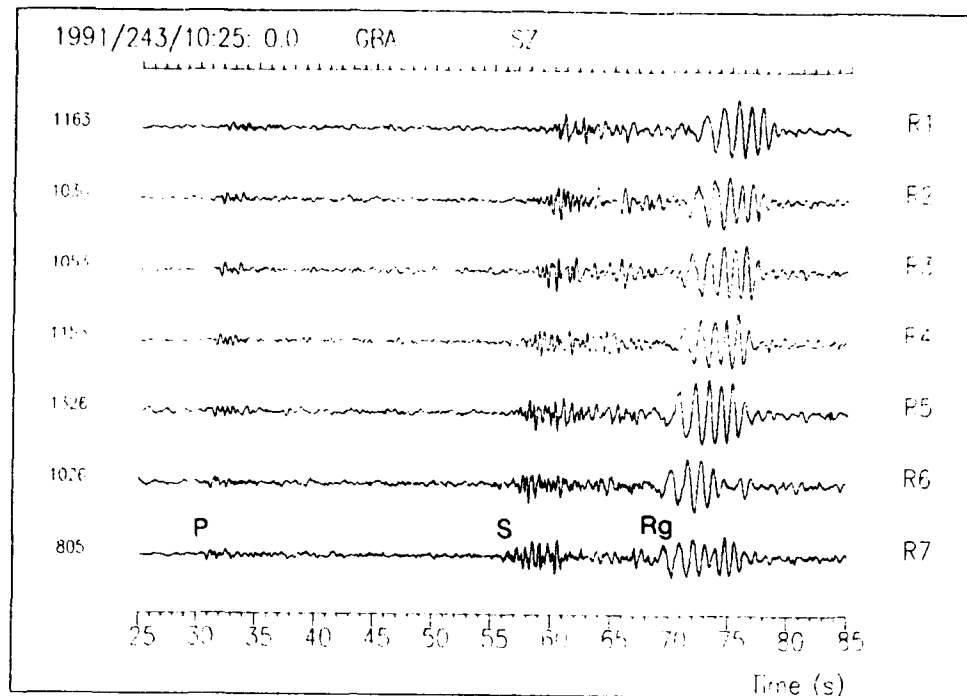
Fig. 1. Typical waveforms for a shallow, local (distance about 215 km) event showing

clear Rg waves. The seismograms are from seven stations along the "red" line of the

Garibidinaur array in India. The Rg phases starting at about 70 seconds have the

highest amplitudes in the seismograms and are characterized by low frequencies and

a dispersive wavetrain (with gradually increasing frequency). Also seen is the S-

phase at about 55 sec and the P-phase at 30 sec.
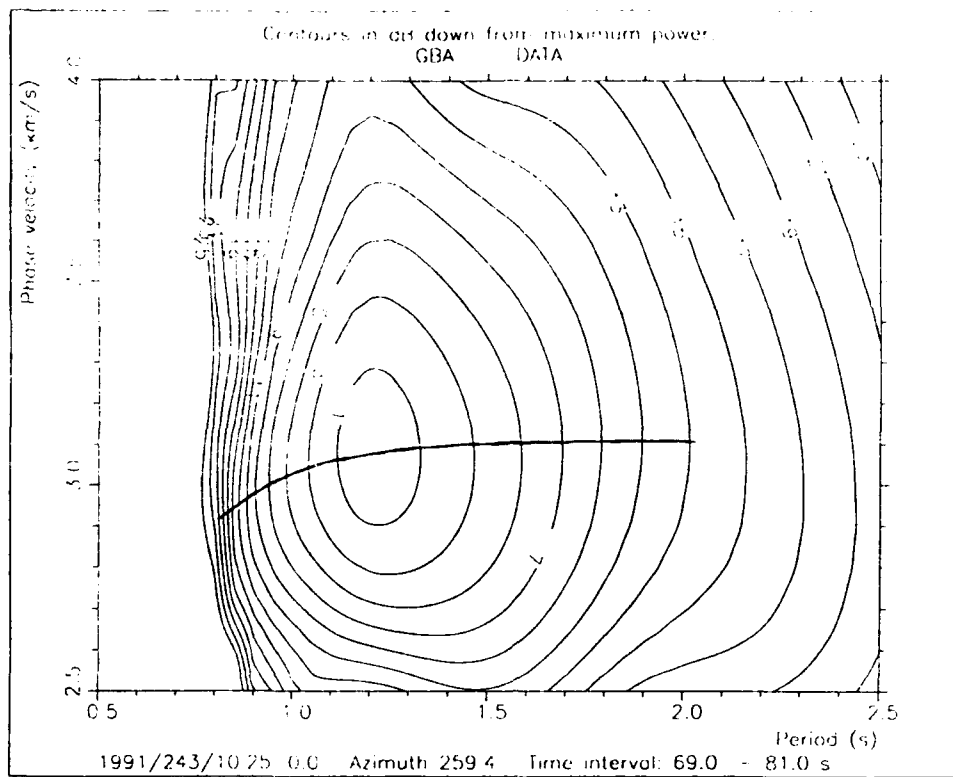
Fig. 2. Dispersion analysis of the event shown in Fig. 1 (all 20 channels are used). The solid line is the dispersion curve used for inversion.

Fig. 3. The averaged dispersion curves extracted for the seven arrays used in this study.
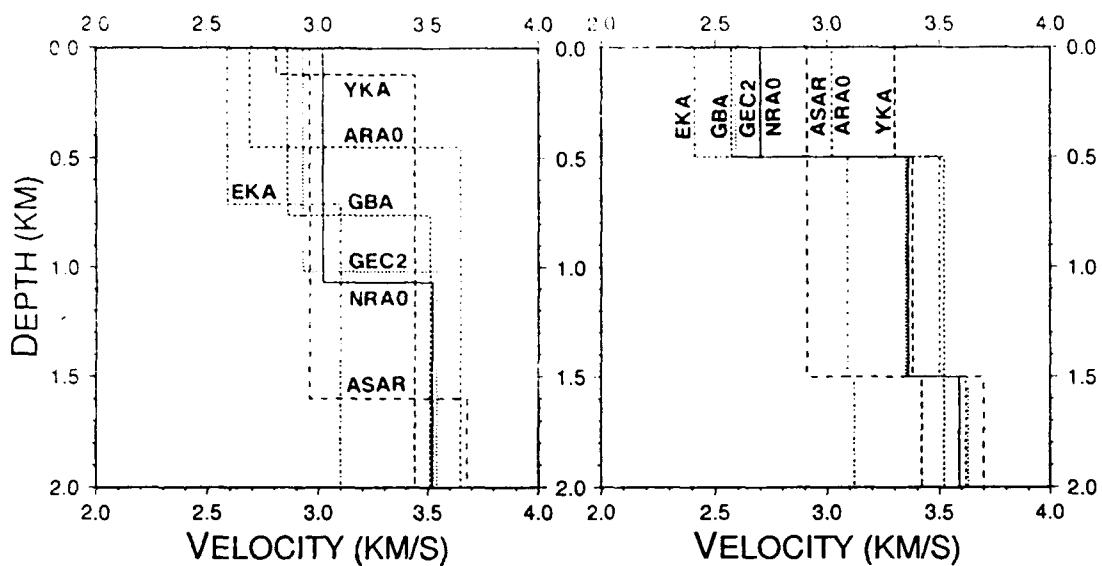
Fig. 4. S-velocities versus depth for the two types of models considered. On the left side results from Model 1 inversion are shown (1 layer, variable velocities and thickness), while Model 2 results (2 layers, variable velocities, fixed thicknesses) are shown to the right.
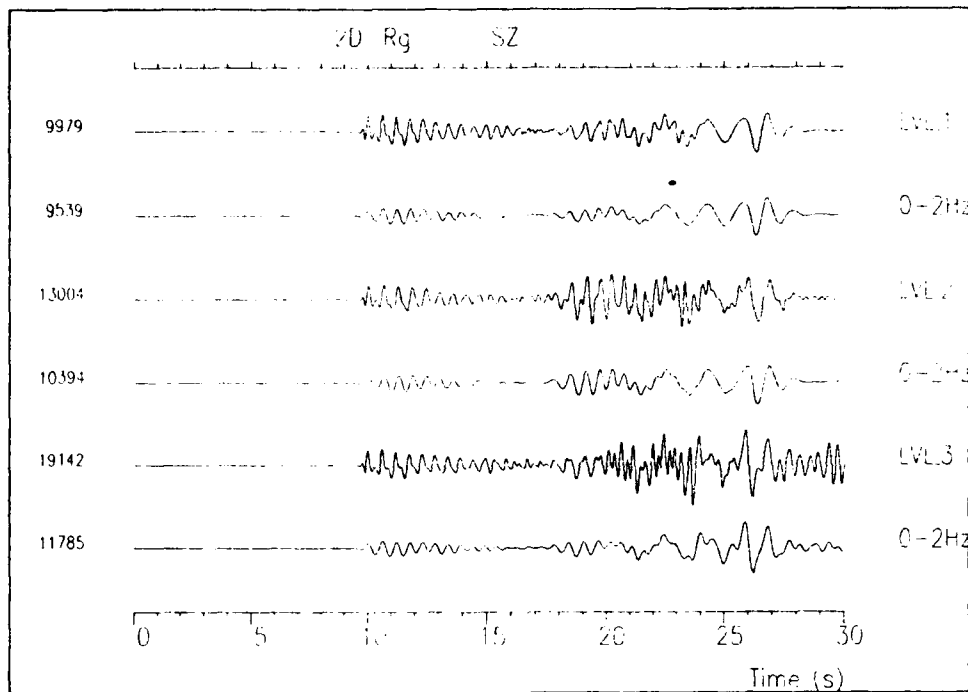
Fig. 5. Synthetic seismograms computed by 2D finite difference elastic wave modelling for different models. In all three cases the explosion source is l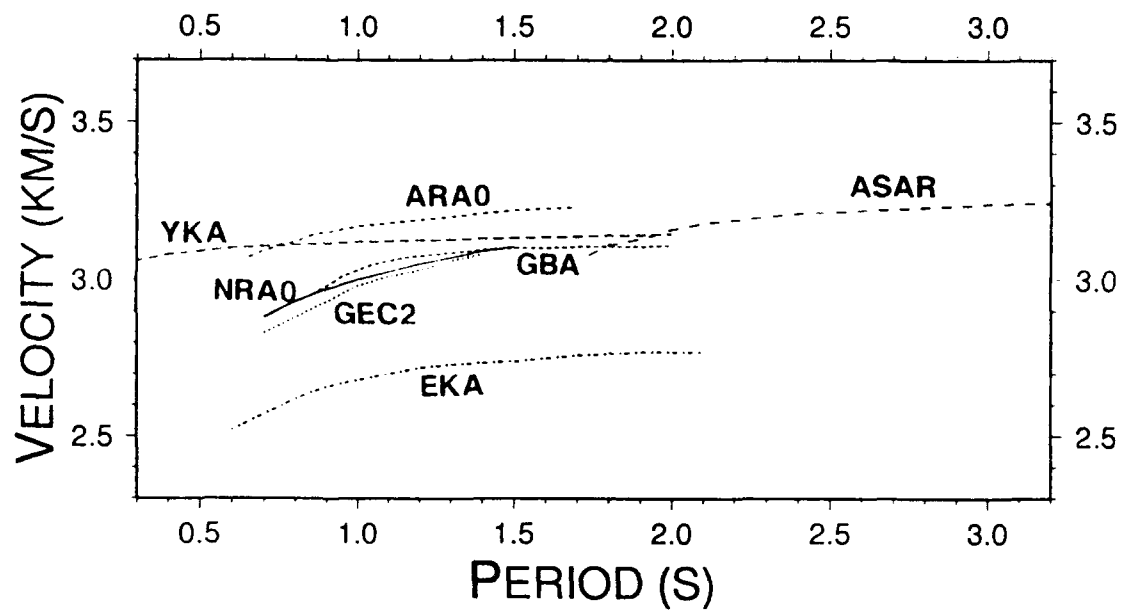ocated at 60 km distance and 2 km depth. The trace labelled LVL_1 was produced with a flat homogeneous low velocity layer. LVL_2 is for a model with random variations in layer thickness, while LVL_3 is for a flat layer with random variations in layer velocity. Further model details are given in Table 3. Below each of the three traces, a low-pass filtered (0-2 Hz) version is shown. Note that the low frequency Rg waves are almost unaffected by the random variations.

Fig. 6. Synthetic seismograms for different source depths (explosion source, homogeneous LVL model and 60 km distance for all cases). Source depths are 2, 4 and 6 km. Rg excitation is seen to diminish very rapidly with depth.

Synthesizing 2D wave propagation in a heterogeneous lithosphere using finite difference techniques

S.O. Hestholm[1], B.O. Ruud[2], E.S. Husebye[3] and B.O. Rosland[1]

1) IBM Bergen Scientific Centre, Norway
2) Dept. of Geology, Oslo University, Oslo, Norway
3) NTNF/NORSAR, Kjeller, Norway
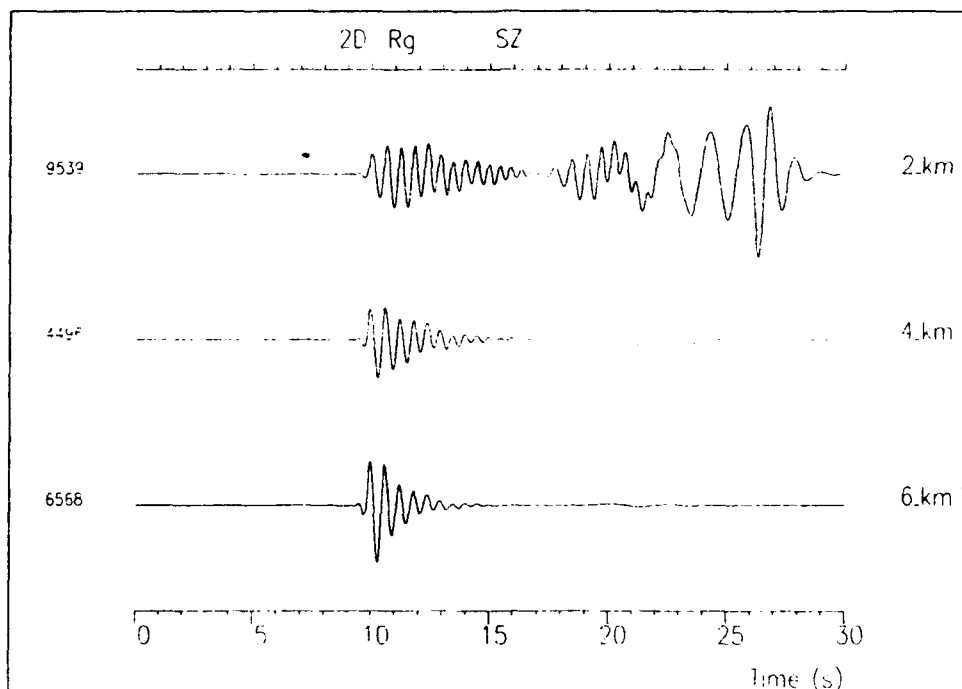
Abstract

In this study we report on efforts in using synthetic seismograms for a better understanding of wave propagation in complex media. Firstly, a comprehensive description is given of the numerical finite difference (FD) technique used to solve the elastic wave equation. Our FD schemes have been tested on 2-dimensional (2D) crust/lithosphere models of varying complexities. The first model considered was a simple one-layered homogeneous crust, then the model was made more complex by adding corrugations to the Moho-interface. Further model inhomogeneities introduced were randomized velocities with correlation functions of the von Karman type. The main result, when comparing to observational records at local distances, is that c. 4 per cent RMS velocity fluctuations in the crust is required to ensure sufficient strong and persistent coda exitation. However, coda coherency remains relatively high which we attribute to the limitation of using 2D-schemes and also that scattering by free surface topography is not taken into account. The relatively small amplitudes of the Pn-phase compared to later P-phases in our synthetics may reflect a lack of sub-Moho velocity gradients in the model. Finally, S-to-P conversions appear to be more efficient than P-to-S, which may prove to be a diagnostic feature for better event classification.

1 Introduction

The understanding of high-frequency (> 1 Hz) seismic wave propagation in the crust/ lithosphere structural system remains problematic to seismologists and exploration geophysicists alike. The observational manifestations of this enigma are easy to illustrate: at local distance ranges both P and S waves are accompanied by prolonged coda waves which are not accounted for by standard structural models. Likewise, array recordings of teleseismic events exhibit intrinsic P-wave time and amplitude anomalies, also between sensors spaced only 1-2 km apart (Haddon and Husebye, 1978). However, complex layered models in combination with wave propagation schemes tied to ray tracing, Gaussian beams, WKBJ, perturbation methods, etc., cannot realistically model observational features of the above kind. The rapid P-wave time and amplitude fluctuations across the large arrays NORSAR (SE Norway) and LASA (Montana) are reminiscent of scattering. The first successful attempts at seismological modelling of such phenomena, using the first order (acoustic) scattering theory of Chernov (1960), were Aki (1973) (see also Bertheussen et al, 1975; Flatte and Wu, 1988, among others). In this context, the scattering medium is described statistically in terms of first and second order moments and the correlation distance length. Naturally, in the solid earth scatterers must have deterministic locations, as elegantly demonstrated by Aki et al (1977), using their novel tomographic technique in analysis of array P-time residuals.

Efforts to exploit the information potential of the coda waves from small, local earthquakes have met with relatively little success in terms of locating specific scattering sources. On the other hand, Aki and Chouet (1975) demonstrated that characteristic coda features like duration, decay rates and scattering attenuation can be modelled in terms of a single backscattering theory (weakly inhomogeneous media -- the Born approximation valid). Further elaborations on the single scatter theory come from the work of Wu and Aki (1985) and Wu (1985, 1988), who split the scattering contributions in two parts, namely, a back-scattering term stemming from impedance perturbations and a forward-

scattering term stemming from velocity perturbations. Dainty and Toksoz (1977) considered similar problems but using diffusion theory.

The basic problem in most studies of wave propagation in complex media is that scattering theory incorporating the Born approximation is not necessarily valid, while convenient analytical solutions of the elastodynamic wave equation are seldom at hand. In this context it is naturally to aim for the numerical solutions of the wave equation which have been around for some time (Alterman and Karal, 1968). Finite difference solutions here can handle complex media and at the same time properly account for *multiple* scattering effects, although severe computer requirements still limit the practical usage of such powerful modelling tools. Most of the works published so far appear to be aimed at testing the validity of the numerical codes used, exploring the practical applicability of the Born approximation in scattering studies and recently investigating the range of "scattering" functions appropriate for crust/lithosphere medium descriptions. Works of relevance here are Macaskill and Ewart, 1984; Frankel and Clayton, 1986; McLaughlin and Anderson, 1987; Dougherty and Stephens, 1988; Toksoz et al, 1990.

In this study we concentrate on generating FD synthetics with basis in the elastodynamic wave equation, and limit ourselves to 2D crust/lithosphere models. The starting point is details on the velocity-stress formulation used in the numerical solution of the wave equation. Then source functions incorporated and scattering medium functions considered would be described. In the latter case it is of some importance whether medium properties are non-uniform within the lithosphere as claimed by Flatte and Wu (1988). Results are in terms of synthetics for realistic crustal models, which are subsequently discussed in terms of characteristic features of NORESS array recordings.

2 Discretization of the wave equation

The basic equations governing wave propagation in a continuous elastic medium are the momentum conservation and the stress-strain relation. Following Achenbach (1984), in the velocity-stress formulation, these are given by

$$\rho \frac{\partial}{\partial t} v_j = f_j + \frac{\partial}{\partial x_l} \sigma_{jl} \qquad j, l = 1, ..., J \tag{1}$$

$$\frac{\partial}{\partial t} \sigma_{jj} = \lambda \frac{\partial}{\partial x_l} v_l + 2\mu \frac{\partial}{\partial x_j} v_j \qquad j, l = 1, ..., J \tag{2}$$

$$\frac{\partial}{\partial t} \sigma_{jl} = \mu (\frac{\partial}{\partial x_j} v_l + \frac{\partial}{\partial x_l} v_j) \qquad j, l = 1, ..., J \qquad j \neq l \tag{3}$$

where Einstein's summation convention is used. J is the dimensionality of the problem, ρ is density, and λ and μ are Lame's parameters. f_j are body forces and v_j and σ_{jl} are particle velocities and stresses, respectively.

Spatial partial differentiation is achieved through cost-optimized, dispersion-bounded, high-order finite difference operators on a staggered grid. For time stepping a leap-frog technique is used. The discretization of the elastodynamic equations with two staggered numerical space differentiators, $\delta^{\pm}$, applied as in Levander (1988) to stresses and particle velocities leads to:

$$\rho_j^+ \{ V_j^+ (t + \Delta t/2) - V_j^+ (t - \Delta t/2) \} = \Delta t \{ F_j^+ (t) + \delta_j^+ S_{jj}(t) + \sum_{\substack{l=1 \\ l \neq j}}^{J} \delta_l^- S_{jl}^{++}(t) \}$$

$$j, l = 1, ..., J$$

$$S_{jj}(t + \Delta t) - S_{jj}(t) = \lambda \Delta t \sum_{r=1}^{J} \delta_r^- V_r^+ (t + \Delta t/2) + 2\mu \Delta t \delta_j^- V_j^+ (t + \Delta t/2)$$

$$j, l = 1, ..., J$$

$$S_{jl}^{++} (t + \Delta t) - S_{jl}^{++} (t) = \mu_{jl}^{++} \Delta t \{ \delta_j^+ V_l^+ (t) + \delta_l^+ V_j^+ (t) \} \qquad j, l = 1, ..., J; j \neq l$$

with

$$V_j^+ (t) = v_j(x + h_j/2, t) \qquad F_j^+ (t) = f_j(x + h_j/2, t)$$

$$S_{jj}(t) = \sigma_{jj}(x, t) \qquad S_{jl}^{++} (t) = \sigma_{jl}(x + h_j/2 + h_l/2, t)$$

$$\rho_j^+ = \rho(x + h_j/2) \qquad \lambda = \lambda(x) \qquad \mu = \mu(x) \qquad \text{and} \qquad \mu_{jl}^{++} = \mu(x + h_j/2 + h_l/2)$$

$$\delta_j^+ q(x) = \sum_{l=1}^{L/2} d_{2l-1}^+ \frac{q(x + lh_j) - q(x - (l-1)h_j)}{\Delta x_j} \cong \frac{\partial q}{\partial x_j}(x + h_j/2)$$

$$\delta_j^- q(x) = \sum_{l=1}^{L/2} d_{2l-1}^- \frac{q(x + (l-1)h_j) - q(x - lh_j)}{\Delta x_j} \cong \frac{\partial q}{\partial x_j}(x - h_j/2)$$

Here h_j is the unit vector in the jth direction, λ, μ and S_{jj} are defined at the nodes of the Cartesian mesh, ρ_j^+, V_j^+ and F_j^+ are defined at the links connecting the nodes and S_{jl}^{++} and μ_{jl}^{++} are defined at the centers of the "obliquities'.; $\delta^\pm$ are numerical differentiators of coefficients $\{d_{2l-1}^\pm\}$. q is velocity or stress and $L^\pm$ is the length of the operator.

For the numerical dispersion relations, the stability limit and bandwidth introduced by the discretization, the reader is referred to Sguazzero et al (1989). The computational cost (in floating point operations) of an elastic numerical simulation is given by

$$C_{el} = [J^2(n_{op}^- + n_{op}^+ + 2) + 7J - 1] (N_o n_m)^{J+1} \alpha_m^{-1} \qquad (4)$$

Here $n_m \geq 2$ is the number of grid points per shortest wavelength needed to model the wavefield, $n_{op}^\pm = 3(L^\pm /2) - 1$ is the number of floating point operations needed to compute the numerical derivative and N_0 is the number of shortest wavelengths in each direction of the computational domain. $J = 1, 2$ or 3 is the dimensionality of the problem, $\alpha_m = c\Delta t/\Delta x$ is the Courant number of this explicit scheme and c is the relevant propagation speed.

Spatial partial differentiation is performed after the optimization of (4) with respect to $d_{2i-1}^{\pm}$ subject to various constraints (for details, see Sguazzero et al, 1989). This process leads to the optimized operators utilized in our code.

Absorbing Boundary Conditions

By necessity, the numerical modeling limits the medium. To reduce artificial reflections from the numerical boundaries, the velocities and stresses are multiplied by exponentially decreasing terms near the edges. Using this procedure, the reflections are still visible to a certain extent by the time the wave has been reflected and propagated back into the computational domain. This causes errors. Therefore this treatment of boundary reflections requires a relatively long distance in each spatial direction, and thus in 3D becomes computationally intensive. A typical application demands a run time storage of 700-800 MBytes.

A recently developed alternative to this procedure has been forwarded by Higdon (1990, 1991). He introduced an operator to minimize the reflections at the computational boundary. At $x = 0$ this reads

$$\prod_{j=1}^{m} (\cos\alpha_j \frac{\partial}{\partial t} - c_j \frac{\partial}{\partial x}) \tag{5}$$

which will absorb perfectly a plane wave traveling towards the boundary at angle α_j and speed c_j. m reflects the accuracy of the operator, and is the number of angles for which absorption is perfect. Similar operators are used on the other boundaries. A version of this algorithm has been successfully applied to various body geometries and structures. With a suitable positioning of source and receivers, this procedure could halve the distance necessary in each spatial direction. The required 3D run time storage for the computational domain is then reduced to 1/8 of the above. Nevertheless, it is the method of exponentially decreasing terms for damping "edge effects" that has been used in our 2D synthetics. The

accuracy of this method proved to be better than that of Higdon (1990). In the latter case, the problem appears to be that the number of incident angles for which the absorption is good is limited.

Free Surface Boundary Conditions: On the top surface, we use the vanishing stress conditions for a free boundary

$$n \cdot T = 0 \tag{6}$$

Here $\hat{n}$ is the outward normal unit vector of the surface and T is the stress tensor. To get computationally tractable conditions, we assume the free top surface to be locally plane, with $\hat{n} = \hat{k}$, where $\hat{k}$ is the unit vector in the vertical z-direction. x and y are horizontal coordinates. Eq. (6) then leads to

$$\sigma_{zx} = \sigma_{zy} = \sigma_{zz} = 0 \tag{7}$$

Across the discontinuity at the top surface the momentum conservation equation (1) is not valid. Eq. (7) put into the versions of eqs. (2) and (3) for the stresses σ_{zx}, σ_{zy} and σ_{zz} leads to the system

$$\frac{\partial v_x}{\partial z} = -\frac{\partial v_z}{\partial x} \tag{8}$$

$$\frac{\partial v_y}{\partial z} = -\frac{\partial v_z}{\partial y} \tag{9}$$

$$\frac{\partial v_z}{\partial z} = -\frac{\lambda}{\lambda + 2\mu} \left(\frac{\partial v_x}{\partial x} + \frac{\partial v_y}{\partial y} \right) \tag{10}$$

which is closed with respect to the three velocity components. Once these are solved for, it is possible to find the remaining stresses σ_{xx}, σ_{yy} and σ_{xy} on the surface from the appropriate versions of eqs. (2) and (3).

Note, the above boundary conditions are strictly valid for a locally plane free surface and not for one exhibiting topographic relief. The latter case is rather problematic even for 2D models (Jih et al, 1988), and at present such an option has not been incorporated in our numerical scheme.

Discretization of Free Surface Conditions:

The dependent variables, Lame's parameters, the density and volume forces are defined on a staggered grid in accordance to Levander (1988). Because of the way in which the particle velocities and stresses are defined on this grid, it turns out that eqs. (8)-(10) can be resolved as an explicit system of equations once the interior points have been solved for. If only velocities are needed, this suffices as the system is closed. Otherwise eqs. (2) and (3) can subsequently be used to calculate the remaining free-surface stresses.

In our application a cost-optimized, dispersion-bounded 8th order operator of length 8 is chosen as spatial differentiator. It corresponds to a sampling frequency of 3 per minimum wavelength, and it has a relative error bound of 1.9% for the group velocity. Because of the length of the operator, other devices have to be used on the layers near all boundaries. Second order staggered finite differences given earlier as $\delta_j^{\pm}$ with $L^{\pm} = 2$ are therefore employed at all 4 outermost points of the domain. These spatial differentiators are also used for discretizing the system (8)-(10).

Recently, our scheme has been improved by increasing the accuracy near the free surface. Here we use second-order, single-sided, staggered finite difference operators for the discretization of eqs. (8)-(10). Below the surface the operator order gradually increases with depth, that is, from second to fourth and sixth order, and these central, uniform operators are employed on a staggered grid (Fornberg, 1988). In this way, a high level of accuracy is maintained at the surface. For the Courant number used, these operators are stable even when simulating very short wavelength Rg phases. These are fundamental mode

Rayleigh waves propagating along the surface with phase velocities in the range 2.5-3.5 kms^{-1} for periods 0.5-4.0 sec (e.g., see Ruud et al, 1992).

3 Source types used in seismic modeling

Below we give the body force equivalents for the two source types used in this study. We assume that the source extent is small compared to the dominating wave lengths so that we can use a point source approximation. Here $s(t)$ is the source time function and $\delta(x)$ is the Dirac delta function.

Explosion Source (P-source)

$$f_x(x, z, t) = \frac{\partial}{\partial x} \delta(x-x_0) \delta(z-z_0) s(t) \tag{11}$$

$$f_z(x, z, t) = -\delta(x-x_0) \frac{\partial}{\partial x} \delta(z-z_0) s(t) \tag{12}$$

This force field has zero curl $(\nabla \times \mathbf{f} = 0)$ so that no S-waves are generated at the source.

Rotation Source (S-source):

$$f_x(x, z, t) = +\delta(x-x_0) \frac{\partial}{\partial z} \delta(z-z_0) s(t) \tag{13}$$

$$f_z(x, z, t) = -\frac{\partial}{\partial x} \delta(x-x_0) \delta(z-z_0) s(t) \tag{14}$$

This force field has zero divergence $(\nabla \cdot \mathbf{f} = 0)$ so that no P-waves are generated at the source. Unlike the explosion source, this is not an internal source because the angular moment of the force field is different from zero.

In practice an approximation must be used for the delta function. We have used a Gaussian function (with $\sigma \approx 2|h_x| = 2|h_z|$):

99

$$\delta(x) \approx \frac{1}{\sqrt{2\pi}\sigma} e^{-\frac{x^2}{2\sigma^2}}; \qquad \frac{\partial}{\partial x}\delta(x) \approx -\frac{x}{\sigma^2}\delta(x) \qquad (15)$$

For $s(t)$ we have used a function proportional to $\frac{\partial}{\partial t}\delta(t)$ with $\sigma \approx 0.036$ s.

4 Scattering representation of the lithosphere

Seismic wave scattering is a complex phenomenon which depends on the size, distribution and magnitude of the heterogeneities in the lithosphere which in general are unknown. Traditionally, the earth is often modelled as a simple stratified medium, each of the strata having constant physical properties. Seismograms from these models tend to match the gross features of observational records but lack the variations in amplitude and travel time and coda waves accompanying major phase arrivals. These features are symptomatic of scattering from small-scale changes in velocity and/or density.

In the scattering literature, heterogeneous media are commonly described in terms of a few physical parameters like thickness of the scattering layer, heterogeneity correlation distance a (in case of anisotropy a_x, a_z) and heterogeneity fluctuation (RMS variation). We may limit fluctuations to either velocity or density and also introduce corrugated layer boundaries. Heterogeneous media realizations are often represented by random fields where complexities can be expressed in terms of few low order statistical moments based on the above scatter parameters a and RMS. In this context, the Gaussian, the exponential and the von Karman correlation functions have become popular among seismologists. The fall-off rate of the spectra controls the amount of roughness in the realizations. The von Karman function appears most suitable for describing lithospheric heterogeneities (e.g., Frankel and Clayton, 1986; Toksoz et al, 1988; Charette, 1991). Note, we may have several medium realizations with basis in the von Karman function reflecting a particular choice of the v parameter in Table 1. For example for $v = 0.5$ it simplifies to an exponential function while for $v = 0.0$ the medium is characterized with heterogeneities that are

self-similar for ka > 1 (k is wave number). With "self-similar" is meant that the standard deviation of the medium, calculated over equal logarithmic intervals of wave number remains constant over a range of scale lengths (Frankel and Clayton, 1986). Note that Flatte and Wu (1988) in their 3D scattering analysis of NORSAR P-waves used a band-limited power law function, which is quite similar to that of the exponential function.

In the present work we have exclusively experimented with von Karman media with $v = 0.0$ and $v = 0.5$. Likewise, we have used a similar 1D von Karman function to describe a corrugated Moho. In general, the scattering medium is isotropic, but can easily be made "apparently" anisotropic by simply using different correlation lengths along the x- and z- axes, respectively.

5 Synthesizing wave propagation in the crust and lithosphere

The problem at hand is perhaps most easily illustrated through display of real seismic records as in Figs. 1 and 2. The first one shows 3-component NORESS recordings from a ripple-fired quarry blast 300 km away to the southwest. The surprising feature here is that the dominant wavefield amplitude is associated with shear waves (Lg phases) on the transverse component! In Fig. 2 a refraction profiling section from EUGENO-S (Gregersen, 1991) is shown. The outstanding feature here is that the coda dominates the wavefield after the PmP-phase arrival (PmP - P-wave reflected from the Moho). To us it is rather speculative to attempt to identify specific arrivals within the P-coda. In the following, we present a succession of crust/lithosphere synthetics for a suite of models of increasing structural complexities. The basic model parameters are a crustal thickness of 30 km, and P-velocities of respectively 6.15 kms^{-1} and 8.15 kms^{-1} (sub-Moho). P- and S-velocities are related through a Poisson's ratio of 0.25.

Homogeneous crust with different velocity distributions

The homogeneous crustal model considered is shown in Fig. 3a, which also includes ray tracing synthetics. The corresponding 2D FD synthetics, shown in Fig. 3b, are very similar to those generated by ray tracing except for the source spectrum. A noticeable feature in Fig. 3b is the "ringing" appearance of the Rg wavetrain caused by the velocity gradient in the uppermost parts of the crust. Anyway, the striking feature of the Fig. 3 synthetics is the complete lack of significant coda waves which besides have no counterpart in comparison to observational data (Fig. 1 and 2). In other words, for signal frequencies above 1 Hz homogeneous crust/lithosphere models are not tenable for computing realistic seismograms.

Homogeneous crust with sinusoidal shaped Moho

This model is very simple except that the Moho is given a sinusoidal form with $\lambda = 8$ km and Amp = 1 km. The corresponding 2D FD synthetics, dramatically different from those in Fig. 3b, are shown in Fig. 4. We have here used both P- and S-sources at a depth of 10 km. The striking feature of these synthetics is the abundance of distinct secondary phases of types pP, SmS, etc., that is, crustal reverberations. However, in contrast to coda waves in real records, the above secondary phases are highly correlated across line arrays of apertures 5-10 km. Naturally, a flat Moho also gives rise to correlated crustal reverberations. Another interesting feature, specific for a corrugated Moho, is P-to-S converted wavelets (Fig. 4a) appearing between the major P- and S-arrivals. In general, S-to-P conversions seem to be more efficient than P-to-S conversions. The Fig. 4a,b synthetics also demonstrate that there could be a plethora of secondary P-arrivals and to single out one of these as a pP-phase for focal depth estimation is considered a dubious undertaking. Although using a regular, sinusoidal shaped Moho interface represents an oversimplification, it serves to illustrate that even minor undulations of a major structural discontinuity could profoundly affect seismic recordings at local distances in a nontrivial way.

102

Random media synthetics

In this model the von Karman medium considered is of the exponential type (v = 0.5) with a = 0.004 km and RMS = 4 per cent. The a parameter value here reflects a model specification error, should have been 4 km, but still reasonably realistic synthetics were produced. For the P-source synthetics (Fig. 5a), the coda excitation is moderate relative to the preceding P-arrival. On the other hand, for the first 4 sec into the coda the coherency is high, and then drops sharply to a level typical of observational data. The S-source synthetics (Fig. 5b) appear somewhat different and on two accounts: Firstly since P-excitation is weak, the P-phase amplitude and the coda level are roughly similar. Secondly, the coda coherency is rather high due to a specific phase arrival at 42 sec on the local time scale. With no "deterministic" explanation for this phase arrival, it is considered due to fortuitous interferences of scattering wavelets. The essence of this experiment is that a medium with RMS velocity perturbations of ca 4 per cent suffice for generating a reasonably strong coda. Observational studies also imply velocity perturbations of this order (4 per cent) for correlation distances in 10-30 km range (e.g., see Aki, 1973; Berteussen et al, 1975; Flatte and Wu, 1988).

Generalized random media synthetics

In this experiment, we use a crust/lithosphere model which we consider to be fairly representative of the real earth. Firstly, a top crust low-velocity layer (LVL) of 1.4 km thickness is included, as this appears to be a widespread continental structural feature (Ruud et al, 1992). The medium randomization (detailed in Table 1) also includes perturbations of the LVL bottom interface and the Moho. The RMS velocity variations are 4 and 2 per cent in the crust and below Moho, respectively. Note that both Flatte and Wu (1988) and Charette (1991), on the basis of NORSAR and NORESS scattering observations, favor relatively smaller velocity perturbations below Moho than above Moho (ca 3 and 2 per cent, respectively). Anyway, the synthetics for this medium are displayed in Fig. 6,

and the following comments apply: Firstly, the S-synthetics in Fig. 6b have some resemblance to the Blåsjø recordings, although the Pn, Pg and PmP are somewhat weak. The P-source synthetics (Fig. 6a) exhibit some resemblance to the profiling records displayed in Fig. 2. The first-arriving Pn is weak, followed by strong Pg and PmP phases, and then a prominent and persistent coda wavetrain. In an attempt to identify specific arrivals here, a semblance analysis was undertaken. For the P-source records (6a), wavelets arriving after the 50 sec time mark (semblance values 0.50 or greater) exclusively exhibited velocities in the range 3.0 to 4.0 kms^{-1}. For the S-source synthetics (Fig. 6b), a semblance analysis gave similar velocity results, although the shear arrivals started at 53 sec and semblance values reached 0.8 units. In other words, Sn-phases must be very weak and the same applies to SmSSmSSmS-type of phases with expected phase velocities in excess of 4.4 kms^{-1}. Seemingly, many of the late-arriving wavelets must be caused by asymmetric reflections caused by the non-plane boundaries of the crustal waveguide.

As noted above, there are several common features between the observational records in Figs. 1 and 2 and our synthetics as displayed in Fig. 6. However, there is also a significant discrepancy between these two record sets, namely, that the synthetic coda waves are too highly correlated. The obvious explanation here is that for computational reasons we are restricted to 2D modelling and a flat surface, thus ignoring "out of plane" interfering scattering wavelets and also scattering by topography. Observationally, it is fairly easy to demonstrate the importance of such contributions, say by array analysis of coda waves (Bannister et al, 1991). Another problem is that in the synthetic records, the Pn-phase appears too weak in comparison to Pg- and/or PmP-phases. Tentatively we attribute this to a lack of even a weak sub-Moho velocity gradient - the validity of this hypothesis will be tested by computing synthetics for models incorporating such features.

6 Discussion

This study was aimed at advancing our understanding of high-frequency seismic wave propagation at local distances, thus exclusively involving the crust/lithosphere system. From numerous previous studies we have that such media are inhomogeneous and often are represented by random fields, where complexities can be expressed in terms of a few low order statistical moments based on scattering parameters like correlation distance and RMS velocity perturbations. Since traditional approaches, say ranging from ray tracing to perturbation methods, are not entirely adequate for computing synthetics for inhomogeneous media, we have explored the usefulness of 2D finite difference synthetics. We started with simple structural models of the kind used in seismic profiling studies, and not surprisingly found that the corresponding synthetics had little in common with real observations. Since Moho represents a first-order discontinuity with medium property contrasts of the order of 15-20 per cent, perturbing the geometry of this interface as demonstrated in Fig. 4 strongly contributes to the number of observable secondary phases and also the coda per se. In Fig. 5 we demonstrate that an inhomogeneous medium (flat Moho) with an RMS velocity perturbation of 4 per cent would generate a significant amount of coda waves. Our most complex crust/lithosphere model features both a top crust low-velocity layer, a perturbed Moho geometry and otherwise randomized velocity fluctuations "produce" synthetic seismograms with complexities comparable to real recordings, although the coda wave correlation is a bit high.

At this stage of development, we have not specifically aimed at quantifying the relative importance of various scattering sources. Even on a very powerful IBM 3090 machine (IBM Scientific Centre Bergen), it takes days to compute synthetics like those displayed in Fig. 6. In the context of event classification, geometrical aspects of such problems must be explored. For example, to what extent are generations of secondary phases and coda waves dependent on focal depth. Likewise, could Moho undulations act as a blocking mechanism for efficient crust/lithosphere wave propagations? Such barriers are often

attributed to mountain roots, sedimentary basins and even ancient plate boundaries. As demonstrated above, 2D FD synthetics are well-suited for providing an in-depth physical understanding of such problems.

7 Concluding remarks

In this report we have demonstrated that 2D FD synthetics computed for even simple (inhomogeneous) von Karman media can produce quite complex seismograms including prolonged coda waves. Although we have not specifically attempted to evaluate which of the medium parameters are dominant for generating coda waves, RMS fluctuations of the order of 4 per cent and minor Moho perturbations are clearly important here. Also, a pure P-source in a cracked medium would produce relatively strong Lg-waves as typical of many mining explosions. On the other hand, our S-source generates some P-waves, which implies that S-to-P conversions are more efficient than P-to-S conversions. In all our synthetic records, the Pn-phase is relatively weak, which we take to imply that sub-Moho constant medium velocity probably is not a good approximation of the real earth.

Finally, the advantage of FD synthetic seismogram analysis is an improved physical insight in complex media like the crust/lithosphere system. This in turn is of importance for the design of event classification criteria simply because the path effect and focal depth would be dominant factors at local/regional distance ranges.

Acknowledgments

8 References

Achenbach, J.D. (1984): Wave Propagation in Elastic Solids, Elsevier, New York.

Aki, K. (1973): Scattering of P waves under the Montana LASA, J. Geophys. Res., 78, 1334-1346.

Aki, K., A. Christoffersson and E.S. Husebye (1977): Determination of the three-dimensional seismic structure of the lithosphere, J. Geophys. Res., 82, 277-296.

Aki, K. and B. Chouet (1975): Origin of coda waves: source, attenuation and scattering effects, J. Geophys. Res., 80, 3322-3342.

Alterman, Z.S. and F.C. Karal, Jr. (1968): Propagation of elastic waves in layered media by finite difference methods, Bull. Seism. Soc. Am., 58, 367-398.

Bannister, S.C., E.S. Husebye and B.O. Ruud (1990): Teleseismic P-coda analyzed by three-component and array techniques -- deterministic location of topographic P-to-Rg scattering near the NORESS array, Bull. Seism. Soc. Am., 80, 1969-1986.

Berteussen, K.-A., A. Christoffersson, E.S. Husebye and A. Dahle (1975): Wave scattering theory in analysis of P-wave anomalies observed at NORSAR and LASA, Geophys. J.R. astr. Soc., 42, 403-417.

Charette, E.E. (1991): Elastic wave scattering in laterally inhomogeneous media, Ph.D. thesis, MIT, Cambridge, MA, USA, 222 pp.

Chernov, L.A. (1960): Wave Propagation in a Random Medium, translated by R.A. Silverman, McGraw-Hill, New York.

Dainty, A.M. and M.N. Toksoz (1977): Elastic wave propagation in a highly scattering medium -- a diffusion approach, J. Geophys., 43, 375-388.

Dougherty, M.E. and R.A. Stephen (1988): Seismic energy partitioning and scattering in laterally heterogeneous ocean crust, Pure and Appl. Geophys., 128, 195-229.

Flatte, S.M. and R.S. Wu (1988): Small-scale structure in the lithosphere and asthenosphere deduced from arrival time and amplitude fluctuations at NORSAR, J. Geophys. Res., 93, 6601-6614.

Fornberg, B. (1988): The pseudospectral method: Accurate representation of interfaces in elastic wave calculations, Geophysics, 53, 625-637.

Frankel, A. and R.W. Clayton (1986): Finite difference simulations of seismic scattering: Implications for the propagation of short-period seismic waves in the crust and models of crustal heterogeneity, J. Geophys. Res., 91, 6465-6489.

Gregersen, S. (1991): Crustal structure across the Tornquist Zone (southwestern edge of the Baltic Shield): A review of the Eugeno-S geophysical results. Tectonophysics, 189, 165-182.

Haddon, R.A.W. and E.S. Husebye (1978): Joint interpretation of P-wave time and amplitude anomalies in terms of lithospheric heterogeneities, Geophys. J.R. astron. Soc., 55, 19-43.

Higdon, R.L. (1990): Radiation boundary conditions for elastic wave propagation, SIAM J. Num. Anal., 27, 831-870.

Higdon, R.L. (1991): Absorbing boundary conditions for elastic waves, Geophysics, 56, 231-241.

Hyndman, R.D. and S.L. Klemperer (1989): Lower-crustal porosity from electrical measurements and inferences about composition from seismic velocities, Geophys. Res. Lett., 16, 255-258.

Levander, A.R. (1988): Fourth-order finite-difference P-SV seismograms, Geophysics, 53, 1425-1436.

Macaskill, C. and T.E. Ewart (1984): Computer simulation of two-dimensional random wave propagation, IMA J. Appl. Math., 33, 1-15.

McLaughlin, K.L. and L.M. Anderson (1987): Stochastic dispersion of short period P-waves due to scattering and multipathing, Geophys. J.R. astron. Soc., 89, 795-821.

Ruud, B.O., E.S. Husebye and R.S. Hestholm (1992): On crustal short-period Rg-propagation using array records from 4 continents, manuscript submitted.

Sguazzero, P., M. Kindelan and A. Kamel (1990): Dispersion-bounded numerical integration of the elastodynamic equations, Comp. Meth. Appl. Mech. Eng., 18.

Toksoz, M.N., A.M. Dainty, E. Reiter and R. Wu (1988): A model for attenuation and scattering in the earth's crust, Pure and Appl. Geophys., 128, 81-100.

Toksoz, M.N., A.M. Dainty and E.E. Charette (1991): Coherency of ground at regional distances and scattering, Phys. Earth Planet. Inter., 67, 162-179.

Wu, R.S. (1985): Multiple scattering and energy transfer of seismic waves -- Separation scattering effect from intrinsic attenuation, Geophys. J.R. astron. Soc., 82, 57-80.

Wu, R. (1988): Multiple scattering and energy transfer of seismic waves -- Separation of

scattering effect from intrinsic attenuation: II. Application of the theory to Hindu

Kush region, Pure and Appl. Geophys., 128, 49-80.

Wu, R. and K. Aki (1985): Elastic wave scattering by random medium and the small-scale

inhomogeneities in the lithosphere, J. Geophys. Res., 90, 10261-10273.

Layer	H (km)	Pvel (kms⁻¹)	ρ (g/cm³)	Interface von Karman			Randomization von Karman			
				v	a	RMS	v	RMS	a_z	a_x
1	0.4	4.88	2.65	-	-	-	-	-	-	-
2	1.0	4.88	2.65	0.5	5	0.1	0.5	4.0	0.1	0.5
3	28.6	6.15	2.85	0.5	1.5	1.0	0.5	4.0	1.0	10.0
4	∞	8.15	3.34	-	-	-	0.5	2.0	1.0	15.0

Table 1: Crust/lithosphere model used for computing the synthetics for P- and S-sources at a depth of 12 km (waveforms are displayed in Fig. 6). H is layer thickness. S-velocities were calculated from the P-velocities (Pvel) given a Poisson ratio of 0.25. For the von Karman random media, v is the order and a is the correlation distance in km. The RMS fluctuation is given in km for the corrugated interfaces and in per cent for velocities.
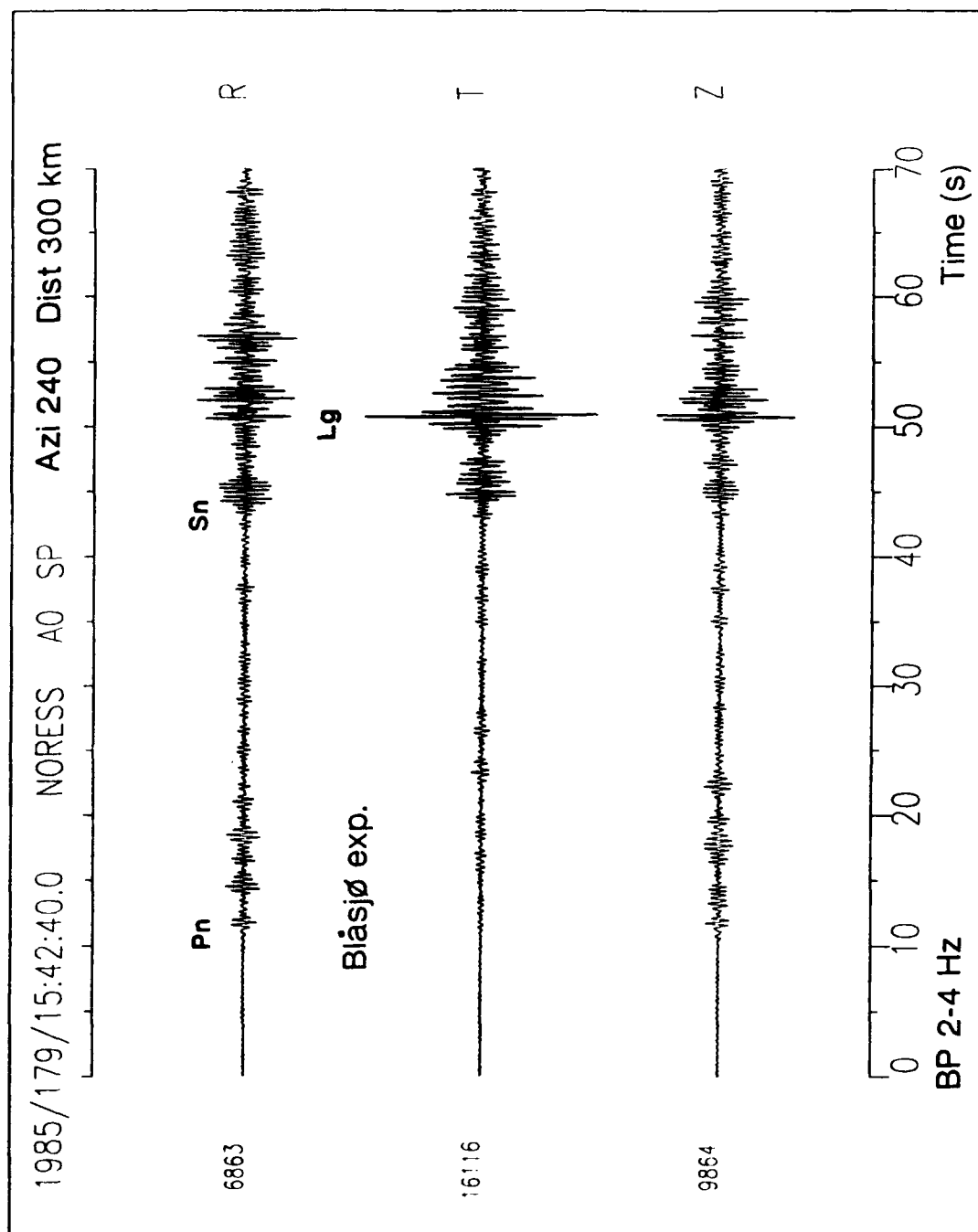
Fig. 1: NORESS recording of a Blåsjø-explosion. The outstanding scattering-related feature is the strong Lg-phase on the transverse component. Also notice the strong and persistent coda level between the Pn- and Sn-phases.

113
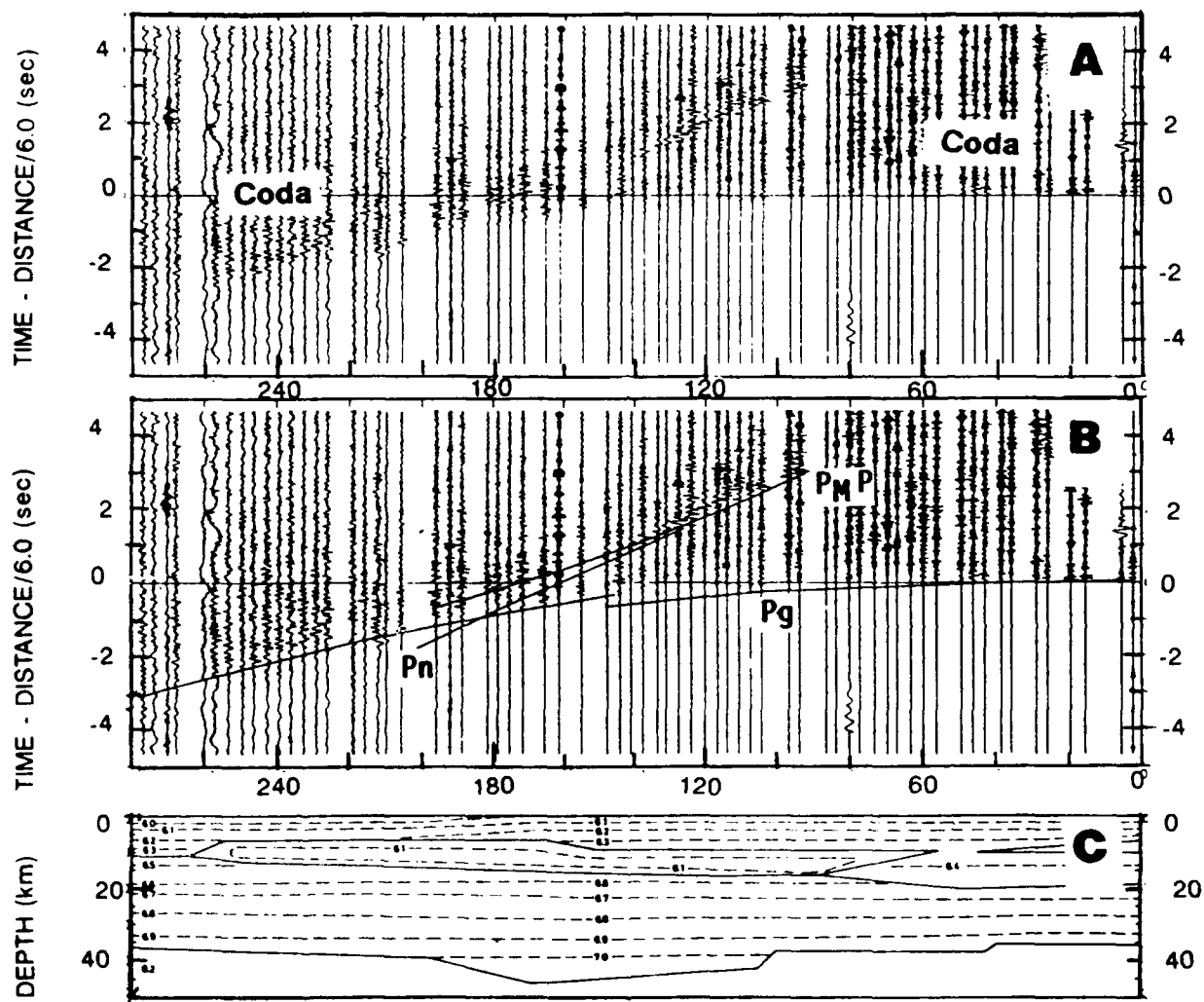
Fig. 2: Refraction profiling records reproduced from Gregersen (1991). a) Original profil-

ing records; b) Same as a) with travel time curves added; c) crustal velocity model

used. The outstanding feature here is the absence of any distinct arrival after the

PmP-phase.

High Velocity Lower Crust
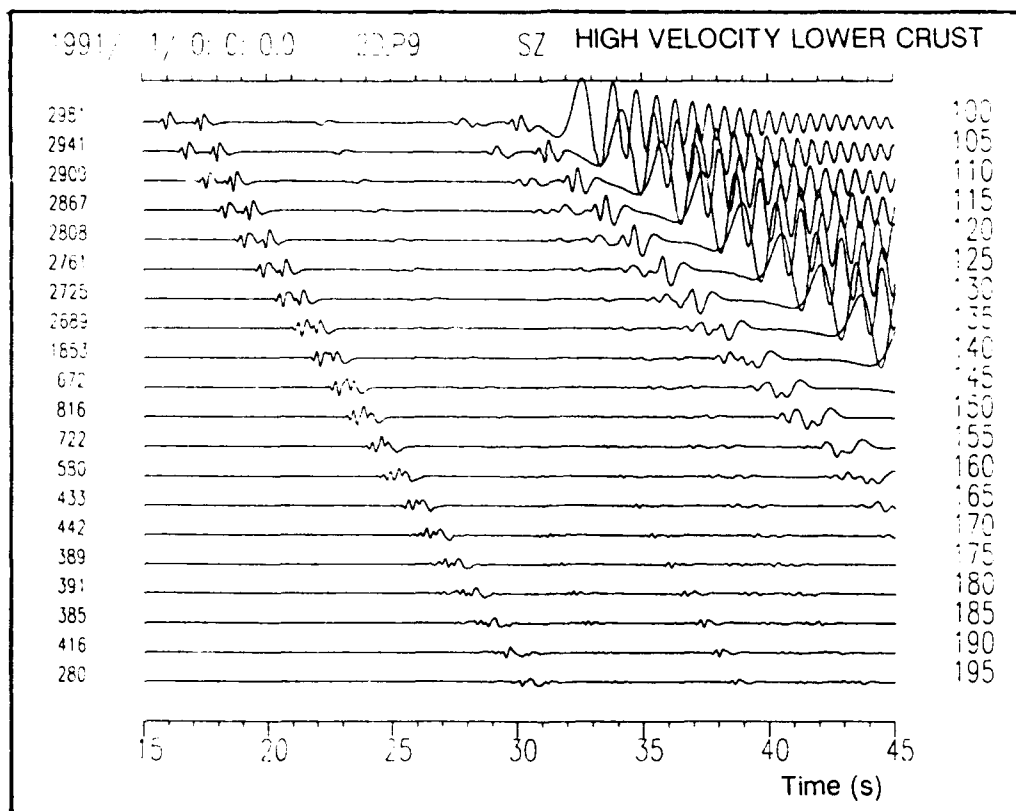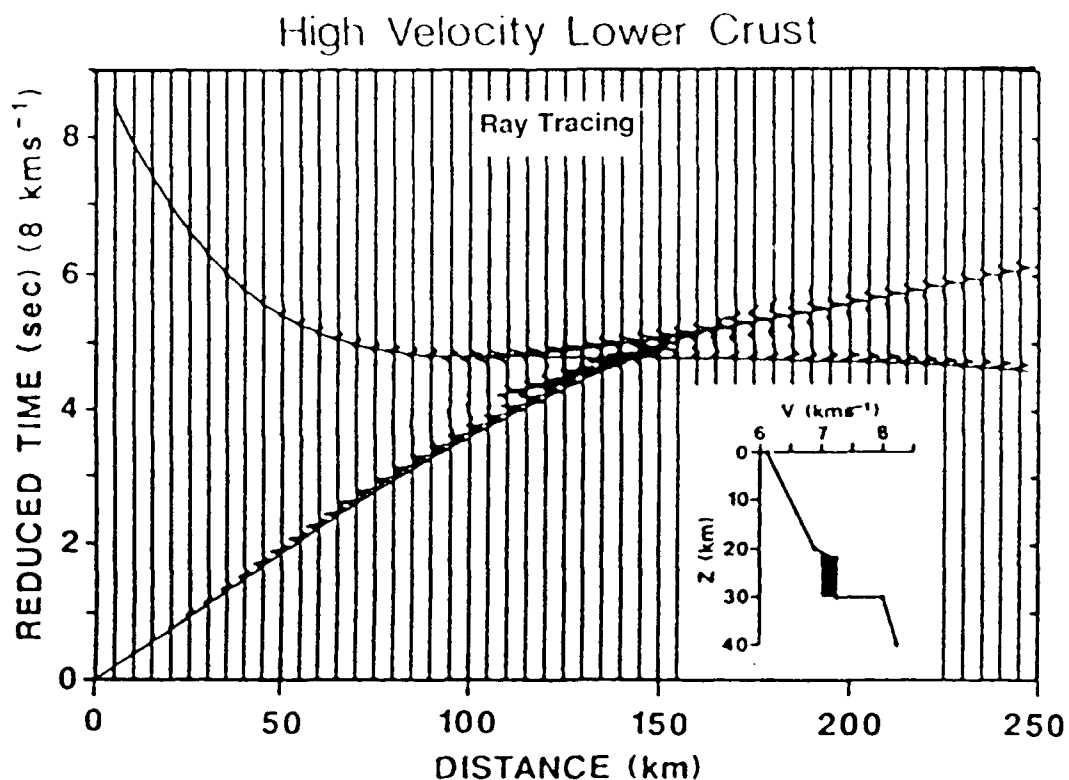
Fig. 3: Comparison between ray tracing and 2D Fd synthetics for a "High Velocity Lower Crust" model taken from Hyndman and Klemperer (1989). For such a simple homogeneous model, the differences between the two sets of synthetic records are small. A peculiar feature in the FD synthetics (Fig. b) is the apparent ringing in the Rayleigh waves apparently caused by the velocity gradients in the upper crust.

115
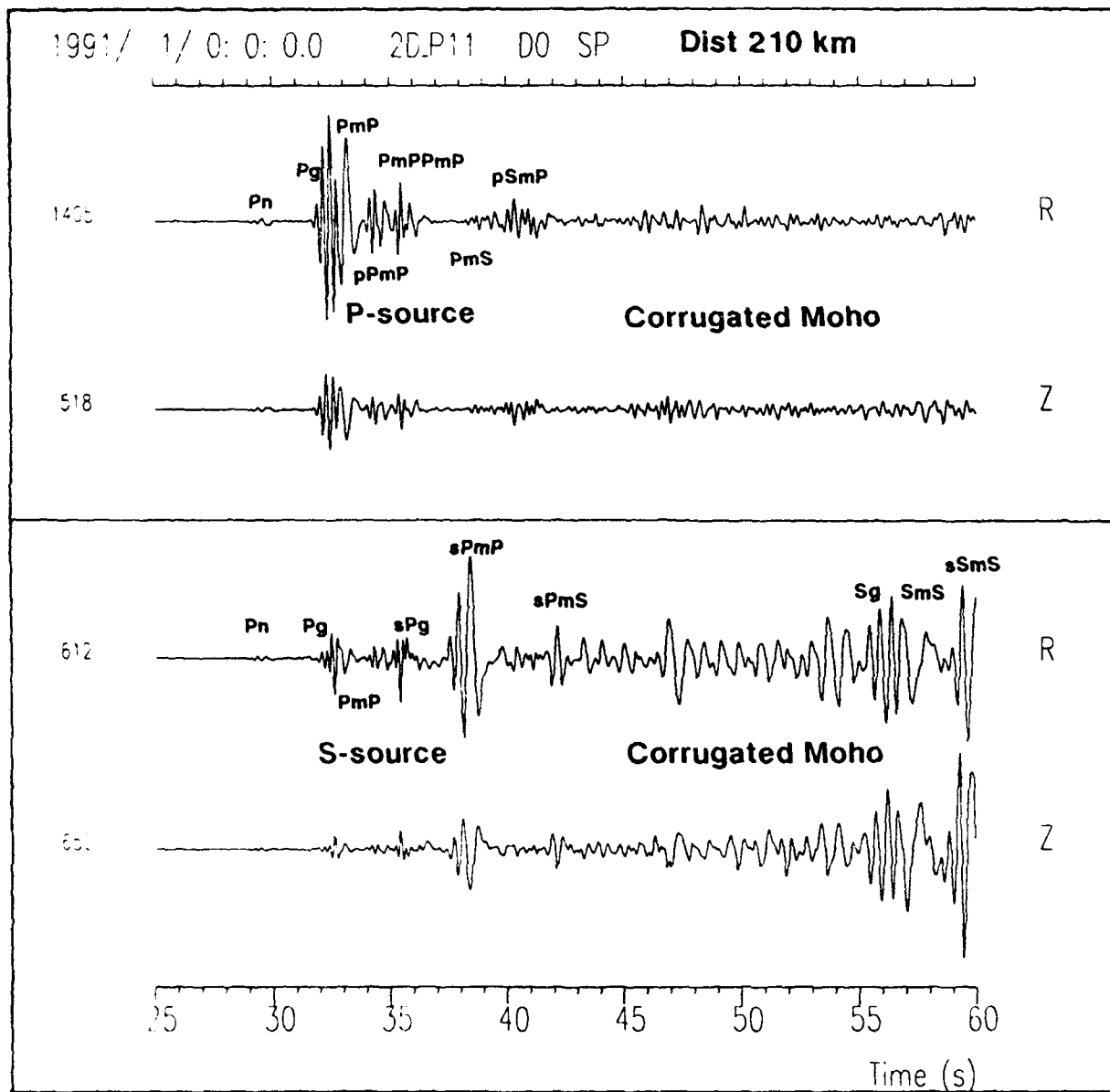
Fig. 4: 2D FD synthetics for a simple crustal model, but with a corrugated Moho ($\lambda = 8$ km, amp = 1 km). Both P- and S-sources are used, and the focal depth was 10 km. The lower parts of figure a) and b) are semblance analysis results of the respective P- and S-source synthetics. Some of the secondary arrivals are likely to have a scattering origin (poor semblance) and also that S-to-P conversions appear to be more efficient than P-to-S conversions.

116

Random medium
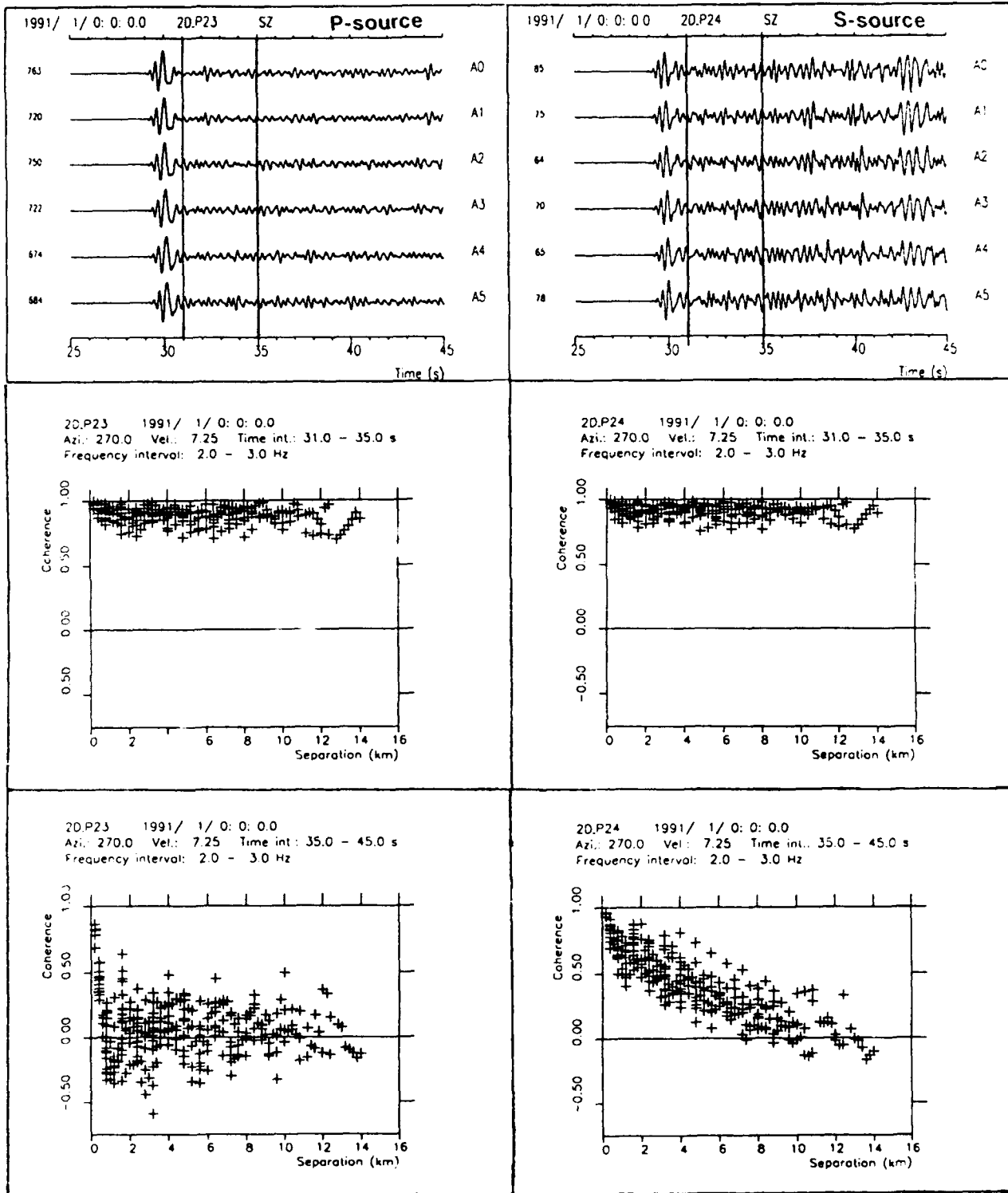
Fig. 5: 2D FD synthetics for a simple, inhomogeneous crust of the von Karman type (v = 0.0; a = 0.004 km; RMS = 4 per cent). P- and S-sources are at the surface, and no corrugated Moho. Sensor separation was 0.4 km and for the P-coda after 35 sec the coherency is approximately zero. The S-coda behaves slightly differently; the arrivals at ca 42 sec are taken to represent fortuitous interferences of scattering wavelets.

117
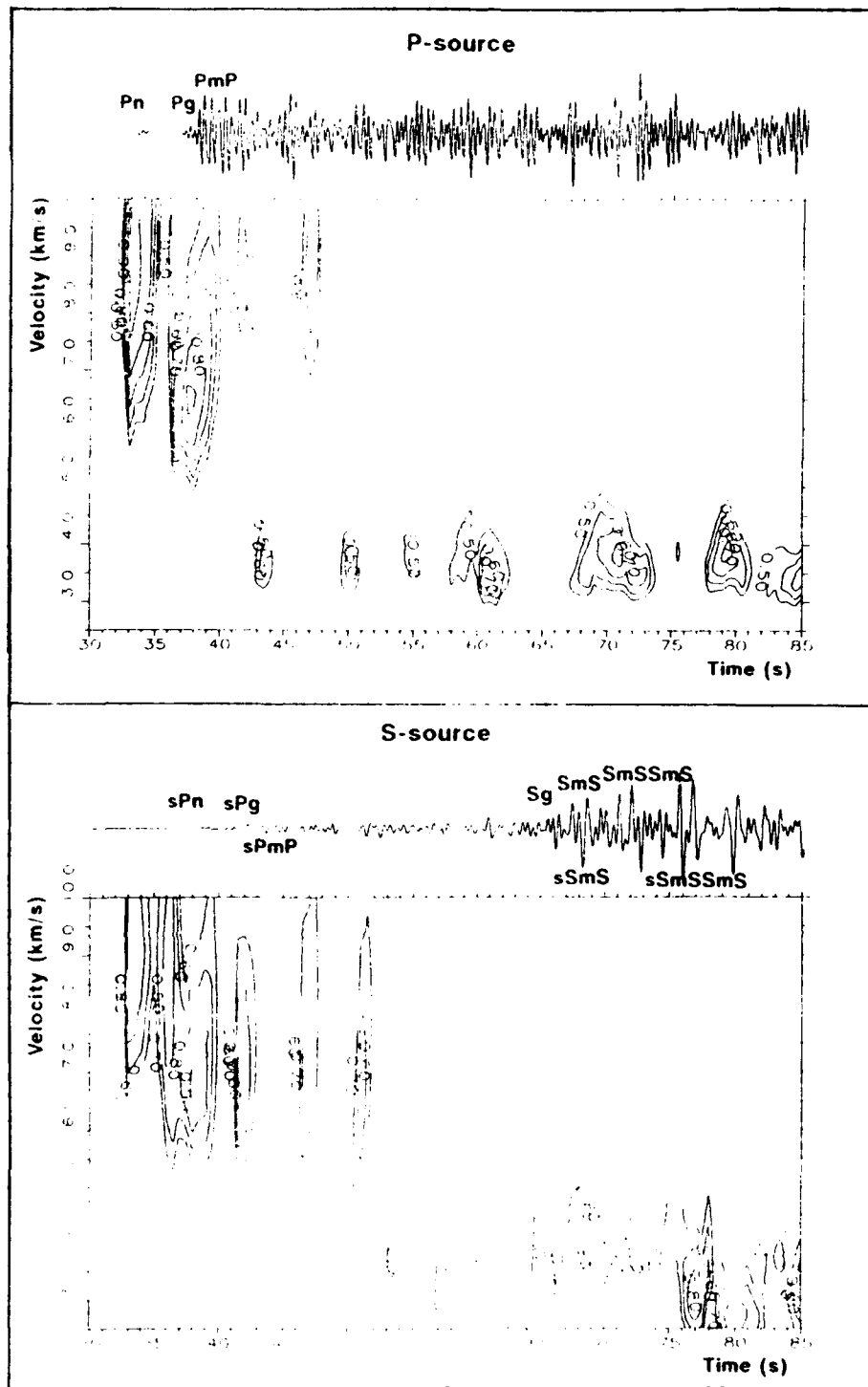
Fig. 6: P- and S-source synthetics for the medium detailed in Table 1. Source depth was 12 km and epicentral distance was 230 km. Below the respective P- and S-source traces the corresponding semblance analysis results are given. The outstanding feature here is that all prominent phase arrivals after 48 sec (P) and 52 sec (S) have phase velocities in the range 3-4 kms^{-1}.

118

Enhanced Seismic Source Discrimination

Using NORESS recordings from Eurasian Events

S.L. Tsvang[1,2], V.I. Pinsky[1,2] and E.S. Husebye[2]

[1] Intern. Inst. of Earthquake Prediction Theory and Math. Geophys., Moscow, USSR

[2] NTNF/NORSAR, Kjeller, Norway

ABSTRACT

The problem of discriminating between earthquakes and underground nuclear explosions is formulated as an exercise in pattern recognition approach analysis. An advantage of our procedure is flexibility, by combing both adaptive noise suppression and event classification incorporating feature selection criteria.

The analysis has been applied to a learning set of 44 nuclear explosions (8 test sites) and 35 earthquakes in Eurasia recorded at the NORESS array (Fig. 1). The signal features considered were the normalized power in 8 spectral bands in the 0.2-5.0 Hz range of the P-wave (6 sec) and the P-coda (30 sec). Physically, it means that we exploit potential differences in the shape of earthquake and explosion spectra, respectively. Other features included are peak P and P-coda amplitude frequencies and relative P/P-coda power. These 19 features were extracted either from conventional array beam traces or the optimum group filtered traces (OGF-removal of coherent low-frequency noise). Using the feature selection algorithm, based on estimates of the expected probability of misclassification (EPMC), only 2 to 4 features were needed for optimum discrimination performance. The dominant features were coda excitation and P- and P-coda power at lower signal frequencies. Furthermore, feature parameters extracted from the OGF traces had a slightly better performance in comparison to those extracted from beam traces. Finally, there were no misclassifications for OGF-derived features when the explosion population was limited to E. Kazakh events, while including events from the other test sites lead to a decrease in discrimination power.

INTRODUCTION

The problem of distinguishing underground nuclear explosions from natural earthquakes using seismic data has been studied for a long time. In fact, it dates back to 19 Sep 1957 as on that day a nuclear explosion, code-named Rainier, was detonated under the Nevada desert. The principal goal of the experiment was to explore the ability of an underground test, unhampered by weather and concerns over radioactive fallout, to fulfill all the needs of a nuclear test program. In this respect Rainier was a great success. The resulting seismological data were studied intensely in scientific and political circles, setting a pattern that still prevails. The introduction of seismology to the international political arena took place a year later when scientific experts from the UK, USA and USSR met in Geneva, in Aug 1958, to design a seismic verification system as part of a comprehensive Nuclear Test Ban Treaty (CTB). Scientific experts (now from some 26 countries) still meet regularly in Geneva to discuss the design of such a system for a potential CTB. Source identification (SI) by seismological means remains problematic for small events.

In order to avoid the once troublesome issue of in-country operation of non-national seismic stations, the SI research in the 1960 and 1970-ties focused on observations in the teleseismic window. The most successful criteria for seismic source identification were spectral ratio variants, mainly between non-overlapping frequency bands for the P-signal itself, or the relative signal excitation at 1 sec (P-wave) and 20 sec (surface waves). The latter is often denoted the $m_b:M_s$ (body wave versus surface wave magnitudes) discriminant. Another commonly used discriminant was the so-called complexity tied to the ratio of P coda RMS in two consecutive windows of lengths around 5 sec and 30 sec respectively (Dahlman and Israelson, 1977; Douglas, 1981). A variant of the complexity often denoted the coda discriminant, was introduced by Tjøstheim (1975, 1978) and Sandvin and Tjøstheim (1978) using autoregressive spectral coefficients as signal attributes in combination with more advanced discrimination statistics. A vast literature exists on the seismic source identification problem and the theoretical foundation for the mentioned discriminants; for example, see Bolt (1976), Dahlman and Israelson (1977), Husebye and Mykkeltveit (1981), Kerr (1985), Press (1985), Tsipis et al (1986) and the many articles contained in these books. Other references are Everndon (1977); Evernden and Kohler (1979), and Evernden et al (1986), Blandford (1982), and Pomeroy et al (1982).

The above discriminants, and in particular the m_b: M, one, are efficient in terms of few failures, but often fail for events with m_b magnitudes below 4.5 - 5.0 units due to detoriating signal-to-noise (SNR) ratios. This, seemingly in combination with a lack of novel ideas for source discriminants in the teleseismic window, is taken to explain the relatively few discrimination papers published during the 1980s. On the other hand, during this decade seismic instrumentation and array design improved considerably. It suffices here to mention the advent of the 24 bits digitizer, increased bandwidths (20 Hz or higher) and the introduction of new arrays like NORESS for event monitoring at local distances. In these ranges the event detectability is likely to be around 2.5 to 3.0 magnitude units at the 90 per cent level (Sereno et al, 1991) and the corresponding SI performance is, by rule-of-thumb, likely to be in the 3.0 to 3.5 magnitude range. Obviously, a signal must be relatively stronger in case of classification as compared to detection analysis. The high quality data now at hand from modern arrays and 3-component stations (also USSR deployment) have again triggered interest in seismic discrimination problems (Baumgardt and Young, 1990). Also new concepts have been introduced, namely, the so-called artificial or trained neural networks technique (e.g. see Dowla et al, 1990; Dysart and Pulli, 1990).

In this study we will address the problem of teleseismic source discrimination and explore the potential of the spectral ratio and complexity discriminants. This may seemingly be a step backward, but it is easy to argue that it is not so. We use data from the NORESS array, which has an excellent detectability for events in parts of Eurasia (Ringdal, 1990), and besides many regions are still lacking adequate seismograph network coverage. Also, use of coda waves may prove instructive for similar discriminants at local and regional distances which presently are tied to the spectral content of crustal phases like Pg, Pn, Sn, Sg (Lg). We add here that the recent Taylor and Marshall (1991) discrimination study was based on UK-type array recordings (YKA, EKA, GBA, WRA) of Eurasian events also in the teleseismic window.

EVENT SELECTION AND NORESS RECORD PREPROCESSING

The presumed earthquakes (PDE and ISC listings) and presumed underground nuclear explosions (NO. 'SAR listings) used in this study are given in Tables 1 and 2. According to P. Richards (pers. comm.) such event listings are not always foolproof, hence we have used the word "presumed" here. The latter comprises all Soviet explosions recorded at the NORESS array which became operational in late fall 1984 except for 5 presumed explosions for which no data were available to

us (details in Table 1 caption). Likewise, data were lacking for 14 presumed earthquakes for which the epicenters were within the "framed" area in Fig. 1. The event epicenters are depicted in Fig. 1 as well. Most of the explosions (32 out of 44) stem from the E. Kazakh (Semipalatinsk) test site and hence the earthquakes in the m_b range 4.0 to 6.0 were confined to the same general area. The reason was that the record differences should mainly be attributable to source parameters and no. reflect significant differences in propagation paths. The other test sites are in aseismic areas for which sufficient earthquake recordings are not available. However, the outlaying explosions were included for a check on discriminant robustness. The "choice" of our explosion and earthquake populations reflects source identification outcomes as reported by the ISC or PDE (NEIC/USGS) agencies. There is hardly any other way for "event" selections; in case of gross errors here we aim to identify possible spurious events. Also, the explosions are presumed to be nuclear ones for the simple reason that besides being located in well-established test site areas, chemical explosions on land are hardly ever recorded at teleseismic ranges. The small NORESS array of aperture 3 km has an excellent event detectability for parts of Eurasia. With a 40 Hz sampling the array's bandwidth is 20 Hz. A simple and efficient scheme for SNR enhancement is delay-and-sum processing or beamforming which is most efficient in the 2-8 Hz band (e.g. see Birtill and Whiteway, 1965; Ingate et al, 1985; and Husebye and Ruud, 1989). At lower frequencies (below say 2 Hz) the wavelengths of microseisms are of the same order as the array aperture, and hence strong correlation in the noise across the array is often observed. In such cases maximum likelihood schemes are very efficient in suppressing correlated noise, as demonstrated by Ingate et al (1985). Recently, even more advanced methods have been introduced by Kushnir et al (1990), which are extensively used here for suppressing low frequency propagating noise. The efficiency of the this scheme, commonly denoted the Optimal Group Filtering (OGF) technique is demonstrated in Fig. 2 and also in Fig. 9. Naturally, removal of low frequency noise is important as both theoretical and observational studies demonstrate that part of the discrimination power is vested in the low/high frequency bands of the P-signal (Evernden et al, 1986; Taylor and Marshall, 1991). In the Tjøstheim and Husebye (1976) and Sandvin and Tjøstheim (1978) studies, the noise suppression was by beamforming, which for the large-aperture NORSAR array was efficient due to the much larger sensor spacing here. In addition, noise spectral estimates based on the preceding noise were subtracted from the P-signal spectral estimates but with marginal improvements. We also tried this kind of noise subtraction and with a similar outcome.

Evernden (1977) advocates the use of P-signal frequencies up to 9 Hz in teleseismic discrimination studies, while we restricted the analysis to 5 Hz. Our rationale being that there is not much signal

energy above 5 Hz and besides cultural sources like local quarry blasting, mining explosions and fast running machinery (saw mills) could easily bias the observational data. Also, our discriminant parameters were extracted both from single P-beam traces and from OGF traces in order to have observations for judging the relative importance of the latter.

SIGNAL ATTRIBUTES - CLASS OF WAVEFIELD PARAMETERS FOR DISCRIMINATION

As mentioned, the most powerful discrimination parameters are related to differential signal excitation in different frequency bands for earthquakes and explosions respectively. P-wave parameters are an obvious choice here, because this phase is most easily detected. P-coda waves are intesting as they not only reflect the source but also the source location within the crust/upper mantle. For example, coda excitation and duration are far less efficient for surface explosions and deep earthquakes relative to shallow and intermediate depth earthquakes (Dainty, 1990). Rayleigh waves are not considered simply because they become embedded in background noise for event m_b magnitudes at 4.5 - 5.0 or below. Another disadvantage is that of extensive interference of surface waves from other events are likely to occur (Marshall and Douglas, 1985). The essence of the above discussion is that our class of discrimination parameters is tied to the P-signal and its coda as illustrated in Figs. 2, 3 and 4. The choice of window lengths of 6 sec and 30 sec reflects that most of the desirable information from teleseismic, but also regional events are accumulated in the first 3 - 6 sec of the P-wave and then the subsequent 10 - 30 sec coda waves where scattering contributions are still significant (e.g., see Tjøstheim, 1981; Dainty and Toksöz, 1990; Bannister et al, 1990).

Processing details were as follows. For each event 5 minutes of recordings for all 25 vertical NORESS sensors were extracted. The first 2 minutes of pure noise were used for estimating OGF-filter coefficients for the slowness and azimuth of the individual events. After the filtering was performed, amplitude spectra (FFT) were calculated for the P-signal (6 sec) and the P coda (30 sec). The power spectra for the non-overlapping 8 bands specified in Figs. 2 and 3 were obtained by simple averaging of spectral squared amplitudes. Since the events used in analysis have widely different magnitudes, all power spectra were normalized by their maximums. Physically, this means that potential spectral shape differences are exploited for event discrimination purposes. The final feature parameter values were obtained by taking the logarithm of the normalized spectral values. As shown in Fig. 3 we have 8 feature parameters for both the P signal and the P coda for the same

123

set of frequency bands. Additional parameters introduced (nos. 17 and 18) are peak spectral frequencies and finally the 19th parameter being the ratio of P/P coda spectral maxima. Note that the last parameter is close to the classical complexity definition. Also, from past studies the largest spectral differences between Eurasian earthquakes and explosions appear to be in the 2.6-3.2 Hz band according to Dahlman and Israelsson (1977), and 0.5-1.0 Hz and 2.0-3.0 Hz bands according to Taylor and Marshall (1991). Finally, normalized, average power spectra for the 8 frequency bands detailed in Fig. 3 are for all events analyzed shown in Fig. 4.

DISCRIMINATION APPROACH

The problem of discriminating between earthquakes (EQ) and underground nuclear explosions (NE) is of a general nature. Hence, there are many, often complex classification algorithms which are of potential relevance in this context. Here, we may differentiate between non-statistical approaches like those of "neural networks" (e.g., see Dowla et al, 1990) and the "Kora-algorithms" of Gelfand et al (1976), which contrast with a statistical approach to pattern recognition (Tjøstheim, 1981). Also, the seismic discrimination undertaking is a two-stage process: firstly, relevant discrimination parameters must be defined and extracted from the records, and secondly, descision rules (discriminators) must be introduced to ensure proper event classification.

At the outset of this study, we discussed rather extensively among ourselves which discrimination approach would be best for classification of Eurasian events as recorded by NORESS. The importance of the physical aspect of the problem at hand was duly recognized, that is, the extracted discrimination parameters must be seismologically relevant. For example, Tjøstheim and Sandvin (1978) found that P-wave and coda autoregressive spectral parameters were efficient discriminants, although their seismological relevance is not obvious. Furthermore, the persistence of the seismic source identification problem is that a unique set of discriminants for weak events apparently does not exist, so we wanted to have the ability to decide statistically which ones of such parameters would be most informative for a given area or region. It is here natural to use the probability of misclassification (PMC) as a measure for discrimination power and on this basis to select most significant feature parameters. In short, we decided to use a statistical pattern recognition approach which is well suited for PMC estimation when the number of observations is small and the number of classification parameters is relatively large.

The recognition problem in our case may be formulated as follows. The data set consists of three sets. The first two are the sets R_1 of explosions (NE) spectral parameters vectors $r_i^{(1)}$, and R_2 earthquake (EQ) spectral parameters vectors $r_i^{(2)}$:

$$R_j = \{r_1^{(j)},...,r_{N_j}^{(j)}\} \quad ; \quad r_i^{(j)} = (p_1,...,p_n) \; ; \; j=1,2 \tag{1}$$

N_j -   number of observations in the j-th learning set (earthquakes or explosions), j=1,2

p_k -   values of classification features (spectral parameters P and P-coda), k=1,n

n   -   number of classification features.

R_1 and R_2 form the learning material for the NE and EQ classification features. The third set is the vector X containing discrimination parameters for an "unknown" event, i.e., the vector being classified with no prior knowledge as to its source identification. On the basis of the learning samples R_1 and R_2, we must make a decision on whether X belongs to the first or the second class. This is done by using a decision (discriminator) function $g(X, R_1, R_2)$. The equivalent Bayesian rules are: If $g(X, R_1, R_2) < C$, the hypothesis H1 is correct and X belongs to the first class; if $g(X, R_1, R_2) > C$, the hypothesis H2 is correct and X belongs to the second class. Here C is a constant, that is, a threshold value. Using this decision rule, there are errors of two kinds: the vector X belongs to the second class (the hypothesis H2 is correct), while it is assigned to the first class. Errors of the second kind represent the reverse situation. Errors occur because the observations R_1, R_2 and X are random, measurement errors and the random nature of the discrimination features themselves. The classification errors of the first and second kind are described by the probabilities P1 and P2. It is also assumed that a priori probabilities q_j; j=1,2 of the vector X belonging to the j-th class are known, and the total error probability $P_{err} = q_1 P1 + q_2 P2$ can then be evaluated. In our case the sizes of the learning samples (35 EQ and 44 NE) are comparable to the dimension n of the features space (19 spectral parameters). In such cases, it is difficult to resolve the basic classification problem -- to select the optimum decision rule and evaluate its corresponding error probabilities. Since the distribution patterns corresponding to the first and second class are unknown, it is theoretically impossible to construct a uniformly optimum decision rule, which in all cases will yield the least probability P_{err} of missclassification (Kushnir et al, 1986). For this reason a large number of different rules with different "good" properties is used in practice. The criterion for choosing a particular rule is the requirement of minimizing the PMC. Other aspects, such as computational efficiency and the possibility of analytical evaluation of the PMC associated with a particular rule should also be considered.

From this point of view, when the R_1 and R_2 distributions are norma', the linear discriminant function (LDF) is optimal in some statistical sense (Anderson, 1958).

$$L(X, R_1, R_2) = (X - 0.5(r_1 + r_2))^* \ S^{-1}(r_1 - r_2) < C \quad , \tag{2}$$

where

$$r_j = 1/N \sum_{i=1}^{N_j} r_i^{(j)} \quad ; j=1,2$$

$$S = [(1/(N_1 + N_2 - 1)] \ (A_1 + A_2)$$

$$A_j = 1/(N_j - 1) \sum_{i=1}^{N_j} (r_i^{(j)} - r_j)(r_i^{(j)} - r_j)^*$$

X   - vector being classified,

S   - covariance matrix of learning sets,

r_j - average vector of j-th learning set,

C   - threshold; above is EQ, below is NE

N_j - number of observations in the j-th learning set

*   - matrix transpose.

Note, the LDF expression in eq. (2) is often denoted the Fischer discriminant (Anderson, 1958). When the covariance matrices of learning samples are unequal and the distributions are normal the quadratic discriminator (QDF) may be used:

$$Q(X, R_1, R_2) = (X - r_1)^* \ S_1^{-1}(X - r_1) - (X - r_2)^* \ S_2^{-1}(X - r_2) - \ln(q_1 / q_2) > C \quad , \tag{3}$$

where

S_j - covariance matrix of j-th learning set, j=1,2,

q_j - a priori probability of j-th learning set.

126

Error probability estimation

In the case of fixed learning samples R_1 and R_2 the decision rule $g(X, R_1, R_2)$ is a function of only one vector -- the vector being classified X. The PMC's occurring upon fixing R_1 and R_2 are called conditional probabilities. These probabilities determine the power of the rule "trained" once and then used repeatedly afterwards. Conditional probabilities are random and on changing the learning samples they can, in principle, vary within wide limits. The mean values of conditional probabilities with respect to the distribution of the learning samples are called the expected probabilities of misclassification (EPMC). Estimating the EPMC which takes into account both the random nature of the learning samples R_1 and R_2 and the vector examined X is problematic, even under the simple assumptions that the classes have normal distributions. For LDF an exact expression of EPMC is too complex for practical purposes. However, an approximate expression of the EPMC provides sufficient accuracy for the parameter values used in practice. The principal method of deriving these approximate expressions for error probabilities is that of assymptotic representations of the distributions of discriminator statistics. Of major interest in seismic discrimination analysis is the case when N (number of events in learning sets) and n (number of features) are of the same order and have double digit values. For LDF (Linear Discriminant Function) the asymptotic equation suggested by Kolmogorov, where the error probabilities are investigated when both n and N approach infinity and n/N is constant, remains approximately valid. Deev (1970) has shown that in Kolmogorov's asymptotic, the distribution of the LDF linear discriminator (L in eq. (2)) is asymptotically normal with mean M and variance V:

$$M_j = [2(N-1)/(2N-1-n)] \, [(-1)^j \, D^2/2], \; j = 1,2$$

$$V^2 = [(N-1)(2N-1)(2N+1) \, / \, (2N-n-1)(2N-n)n] \, [D^2 + 2n/N], \tag{4}$$

if $N = N_1 = N_2$,

where $D^2 = (r_1 - r_2)^* \, S^{-1}(r_1 - r_2)$.

From (4), the following approximate expression for the EPMC of the LDF can be written:

$$P1 = P \{g \le C \mid H2\} = G((C-M_1)/V)$$
$$P2 = P \{g \ge C \mid H1\} = G((M_2-C)/V), \tag{5}$$

where

$$G(y) = 1/\sqrt{2\pi} \int_{-\infty}^{y} e^{-x^2/2} \, dx$$

Raudis and Pikyalis (1975) have shown that the relative error in evaluating the probability of misclassification yielded by asymptotic expression (5), as compared with the error computed from an exact expression, is not greater then few per cent in the common observations ranges of N and n. The event classification strategy as adopted in this study is visualized in Fig. 5.

The LDF is used for cases when the covariance matrices of the learning sets being classified are the same. The underlying assumption here is not always valid, so we also considered the more complex quadratic discriminator (QDF - eq. (3)), which is useful when the R_1 and R_2 matrices are different. An expression for the EPMC for QDF has been obtained by Levin and Troitskii (1970), and will not be given here. Anyway, in terms of the data used in analysis in this study, we found that the linear discriminator gave fewer misclassification errors than the QDF. We note that even under more adverse conditions with non-equal covariance matrices and the sample size N comparable to the number of features n, the LDF is still preferable to the quadratic discriminator (e.g., see Pisarenko et al, 1983). This is mainly due to a greater number of unknown QDF parameters in comparison to the corresponding LDF parameters for small learning sets.

Broad applications of LDF in various classification problems have confirmed its efficiency for small sizes N1 and N2 of learning samples and for distributions that differ from normal (Azen et al, 1975; Weber et al, 1986; Tsvang et al, 1986). In essence, the advantage of LDF is its simplicity, and the existence of a method for calculating EPMC.

Selection of most informative features

As mentioned above, the linear discriminant function has a good perfomance when the sizes of learning sets are small. LDF can be applied not only to the total number of discriminant features ($r_i^{(i)}$ in eq. (1)), but also to vectors made up of a subset of the discriminants. Various values of the expected probability of misclassification (eq. (5)) will be obtained. For a certain optimum subset of features, the EPMCs for a small size of the learning set may be much smaller than for the total system of features. This unexpected "multidimensional effect" is explained as follows: the EPMC

128

for LDF are expressed by (eqs. (4) and (5)), which depends on the dimensionality of the space of features n, the sizes of learning sets N_1 and N_2, and the Mahalonobis distance D (eq. (4)). The latter is a non-decreasing function of the number of features n. In practice, this function will for increasing n always tends to a limit, because the information value of features is exhaustible (usually, there are few informative parameters!). Correspondingly, the EPMC should pass through a minimum, because less and less information is being added, while the noise is being increased. Formally, the existence of such a minimum follows from expressions (4) and (5). The natural strategy would be to take only the set of features which represents the minimum of the EPMC. In order to make use of this idea, one must be able to arrange the available features in a sequence such that increasing the set of features by one feature at a time would produce the maximum rate of growth of the function $D^2(n)$. One possible way of ranking the features is the following: at each iteration step K the optimum subset of K-1 features previously selected is increased by adding the one feature from among the remaining set, which yields the largest difference $D^2(K)-D^2(K-1)$. The features are thus ranked in significance and in relation to the Mahalonobis distance D as a function of features n. Then the EPMC are computed and plotted versus ranked features. The optimal subset of features corresponds to the minimum of EPMC, as illustrated in Fig. 6.

This optimal parameters algorithm in combination with the LDF (linear discriminator) exhibits good perfomance in many geophysical applications when the sample sizes are small (Weber et al, 1986; Tsvang, 1986; Tsvang et al, 1986; Avsjuk et al, 1988). That is why the LDF for optimal parameters subset was chosen in our case (35 EQ and 44 NE). In practice, when the distributions of the classes (the learning set observations) are unknown, the results of discrimination are usually obtained using so-called non-parametric methods. Such an approach is very common in seismic event discrimination analysis and is illustrated in Fig. 7.

When the data set is large enough, the simplest way of checking reliability of a chosen discriminator is by using part of the set for learning and the remainder for testing. Usually when the sample size is small, one uses for the classification test the learning set. It is so called the Reclassification method. Here, training of the discriminator is carried out with respect to the entire size of the learning samples. Then all events of these samples are sequentially classified. It provides usually too optimistic discrimination results (Pisarenko et al, 1981) because learning and testing just coincide (see also Table 3). To provide more confident decision we used also the so-called Jack-knife method, which allows the creation of an independent data set for testing the discriminator without decreasing the learning data set. Here learning and testing are carried out

repeatedly: during each learning sequence one element is omitted from the entire sample and in turn used for testing. The total number of errors is then summarized. In essence, all elements of the sample are used both for learning and testing, but the element being used for recognition are statistically independent of the learning set. Finally, it should be noted that Jack-Knife method may also be used for estimating the conditional probability of misclassification (not the EPMC, see section "Error probability estimation").

RESULTS

Perhaps the most important aspect of the seismic source identification problem is that of finding proper discriminant parameters. In practice, this has proved rather difficult since source locations within the crust and the propagation path to the receiver(s) are of significance in this context. In our case we selected 19 discriminant candidates (Fig. 3) and have used the EPMC measure for ranking the relative importance of these parameters as illustrated in Figs. 6 and 7. In these figures we differentiate between two populations, namely, all events (44 NE and 35 EQ) and only Semipalatinsk explosions and all earthquakes (32 NE + 35 EQ) for OGF and BEAM traces, respectively. Parameter no. 19 (Fig. 3) are clearly the most dominant for all cases, and thus demonstrate the relevance of the classical complexity discriminant. There appear to be some differences between the OGF and BEAM trace derived parameters, as in the former case the optimum performance (EPMC minimum) is tied exclusively to the coda parameters. For BEAM traces, the classical spectral parameters are of some importance as weight is given to relative signal power in the low frequency bands (parameters 1 and 3 in Fig. 3). Another way of illustrating discriminant performance is shown in Fig. 8, where the separation between the presumed explosion (NE) and earthquake (EQ) is very good using only the most informative discrimination features, namely, no. 10 and no. 19.

The results of P and P-coda parameter discrimination obtained for the group filter (OGF) and beam traces respectively are shown in Table 3. For example, for Eastern Kazakh explosions only there were no event classification errors when using optimum OGF discriminant parameters (Case 6, Table 3), while in contrast the corresponding BEAM discriminant erred for 3 events (Case 3, Table 3). Including the explosions from the 7 other test sites (Case 5, Table 3) gave that 100% of the Semipalatinsk and 75% of NE from the other test sites were correctly classified. We take this to imply that the chosen discriminant parameters retained their source-type sensitivity despite

130

considerable differences in source environments and propagation paths. Likewise, the two S. Sinkiang explosions (test site no. 6; event nos. 17 and 18 in Table 1) have similar propagation paths as many of the EQ used in our analysis.

The EPMC measure is not linearly related to the number of misclassifications and the same applies to those events which correct classifications are at best marginally significant. This is seen from Figs. 6 and 8 and with further details in Table 3. The parameters no 10 and 19 derived from OGF traces have clearly the best performance without any misclassification when the NE populations are limited to the E. Kazakh test site (Case 6: Table 3). The BEAM parameters produce relatively many misclassified explosions, which with one exception (event 26) do not stem from the E. Kazkh test site. Event 26 remains misclassified even when the explosion population is limited to the Semipalatinsk test site. Note that the difference in the classification errors between EPMC and Jack-Knife is because the latter estimates the misclassification probability for fixed learning sets (conditional probability), while EPMC takes account of randomness in the learning populations. We further remark that the Jack-Knife error estimation is most often used in similar studies.

Among the earthquakes, no. 30 in Table 2 appears to be the most problematic, since it is consistently misclassified both by BEAM and OGF parameters, except for one marginal rating in the latter case (Case 6: Table 3). For other earthquakes being misclassified or given a marginal rating, there is little overlap between the respective OGF and BEAM discriminators. In Fig. 9 a number of events are displayed for which the discriminators were less effective or failed. We would specifically comment on these events in the next section.

DISCUSSION

Firstly, we would comment briefly on travel path and receiver-end structural features which may affect the performance of the discriminators used. The P travel time curve has several branches in the 15-38 deg distance range caused by the so-called 400 km and 650 km velocity discontinuities. Some of the corresponding secondary arrivals may occasionally be very prominent as demonstrated by King and Calcagnile (1974) on the basis of NORSAR recordings of USSR nuclear explosions. For the E. Kazakh (Semipalatinsk) explosions such secondary phases would not affect the coda due to a distance around 38 deg. Some of the explosions are fired in basin areas and the large impedance contrasts between sedimentary strata and the crystalline basement may cause strong reverberations and thus affect the P coda. A typical example here is the Novaya Zemlya test site.

Destructive P-pP interference may affect the relative spectral power below 1 Hz, but according to Vergino (1989a,b) some of the USSR explosions are shallow, that is, have focal depths in the range 150-250 m only. Finally, ripple firing or sequential detonations with 5 to 10 sec intervals cannot always be ruled out. In the latter case, coda based discriminators are likely to fail.

From Table 3 we have that the poorest performance takes place for the combination of all events and all discrimination parameters either derived from OGF or BEAM traces. Rather surprisingly, the number of marginal events seemingly is independent of event population and discrimination parameters used. Regarding the misclassified NE populations, most of the events here are non-Semipalatinsk (E. Kazakh), the exception being event 26 (BEAM) and events 22 and 5 (OGF - Case 4: Table 3). Under optimum conditions (Case 6: Table 3), event 5 is labelled marginal. From the visual inspections of traces (Fig. 9), some of the failures are rather obvious, but this is not the case for NE 26 (BEAM - Cases 1-3: Table 3). We note that the two problematic E. Kazakh events, no 26 and 5, are assigned the smallest m_b values (Table 1).

Also some of the presumed earthquakes are problematic, in particular EQ 17, 22 and 32 (Cases 3 and 5: Table 3). The BEAM and OGF displays in Fig. 9 give the visual impressions that EQ 17 and 32 exhibit P waves rather typical for explosions. A common feature of the 3 events is their northernmost latitude of 47° N, while corresponding longitudes are around 83.3°, 89.7° and 73.6° E (Table 2). Also, EQ 32 is weak ($m_b \sim 4.3$) and besides took place in an area with no previous seismic activity. The ISC bulletins give a normal focal depth of 33 km, and that Garm is the only USSR reporting station.

Note, most discrimination procedures tend to favor a relatively better classification performance for earthquakes as also seen in Table 3. The reason is that explosion discriminants are tied to relatively weak coda excitation and/or P-signal power deficiency in low frequency bands. For decreasing SNR the noise contribution would be more relatively important for explosions and the net effect is that all weak events would "look" like earthquakes. In the latter case it seems reasonable to select for learning sets weak events only and then take advantage of the OGF-technique for noise suppression.

From the above we have that the performance is best when the two learning populations are drawn from roughly the same area. It is also clear that the discriminators derived from the OGF-traces not surprisingly outperform the corresponding BEAM parameters. This is not surprising for

132

the simple reason that the signal-to-noise ratio is significantly better on the OGF traces (e.g., see EQ 32 in Fig. 9). Not easily explainable is the fact that the BEAM parameters are weighted in favor of the low frequency part of the P signal, slightly in contrast to that for the OGF parameters.

Our discrimination results compare favorably with those of Tjøstheim (1978, 1981) and Sandvin and Tjøstheim (1978), who also found that the dominant discrimination power was embedded in the P-wave coda. Their discriminator parameters were tied to autoregressive spectral coefficients, which in turn are related to our prominent parameter no 19 (Fig. 3). On the other hand, the mentioned third moment discriminant weights most heavily the presence of high frequency energy in the recorded P signal and was reported to work very well for USSR explosions recorded at the Hagfors (Sweden) array (Dahlman and Israelson, 1973). This contrasts partly with our findings and also with the results of Tjøstheim (1981), Evernden (1977) and others. The rationale here is that potential high frequency discrimination power is lost (attenuated) for propagation paths exceeding a few hundred kilometers. As also demonstrated here, some low frequency P-signal discriminants are important, as recently reported by Taylor and Marshall (1991) as well.

Discriminators developed for seismic source identifications at local/regional distances are mainly tied to spectral ratios between phases like Pn, Pg and Lg (e.g., see Dysart and Pulli, 1990; and Dowla et al, 1990; see also Su et al, 1991). In the latter study, the Pg phase was associated with a time window tied to the group velocities of 6.0 and 5.0 km/sec - to us this is very close to a Pn coda definition. At these distance ranges, the Lg parameters have proved to be important. However, a potential problem with the Lg phase is its potential blockage for propagation paths across sedimentary basins and similar kinds of crustal heterogeneities (Baumgardt, 1990). The physical explanation for the reported successes in source identifications at local and regional distances is attributed to stronger shear wave excitation for EQ-type sources (strong Lg), which also would imply stronger P coda at any distance.

Finally, we want to comment on various discrimination techniques in use. At the outset of this study the "neural network" approach was not contemplated, and besides Dysart and Pulli (1990) and Dowla et al (1990) reported that the Fisher discriminant had equivalent performances. The reason for this is that the EQ and NE populations are essentially linearly separated. It is here meant that the feature parameters derived from the respective event populations are separated by a straight line in the two parameter case (Fig. 7). We would here add that our approach is relatively robust

133

for small-sized event populations and furthermore that the probability of misclassification introduced here is helpful in judging discrimination performances.

Both the "neural network" and the Fisher discriminators are constructed for multidimensional classification problems, in our case a priori known NE and EQ event populations. Strictly speaking, this is not the case for the non-Semipalatinsk areas, so not unexpectedly the discrimination performances were poorer for the other USSR test sites. An alternative strategy for such cases, which could be highly relevant in many contexts, is to consider singular learning samples of either explosions or earthquakes (e.g., see Tsvang et al, 1986). The problem is related to the task of finding the most powerful discrimination parameters which clearly would affect to some extent the source-receiver wavepath and the local structure in the source area. Our approach, tied to testing an initial large class of discriminators and then estimating which ones are most powerful, appears to be highly efficient in practice.

CONCLUSION

In this study we have presented a comprehensive seismic source discrimination scheme for teleseismic events. The observational data were based on USSR events as recorded by the NORESS (Norway) array.

The learning population comprised 44 nuclear explosions (NE) and 35 earthquakes (EQ) from the general E. Kazakh area. An explosion subset comprised 32 events from Semipalatinsk. The discriminant features used in analysis were extracted both from the conventional array beam traces and from beam traces derived by OGF, where low-frequency (below 2 Hz) coherent noise is suppressed. Major results were as follows:

1. A total of 19 potential discrimination features were considered. These were mainly tied to normalized spectral power in 8 frequency bands for both P- and P-coda waves of durations 6 sec and 30 sec, respectively. Also, the classical P-complexity discriminant was incorporated.

2. The most effective discrimination features were the complexity one, and relatively low P-signal frequencies. The best classification performance was obtained by using 2 to 4 features which in turn were selected on the basis of the extracted measure of maximum misclassification probability.

3.   The features extracted from the OGF event traces had a slightly better performance than those derived from the conventional event beam traces. The corresponding optimum feature subsets were somewhat different.

4.   When the explosion population was restricted to the Semipalatinsk area, a complete event classification was obtained using OGF-derived features. However, 3 events here were rated of marginal significance.

5.   Inclusion of all the NE from the other 7 test sites resulted in a slight increase of 6.5 per cent in the classification error. This implies that the chosen discriminant parameters retain their source-type sensitivity despite considerable differences in source environments and propagation paths. Likewise, our discriminants were able to separate S. Sinkiang explosions from nearby earthquakes having similar propagation paths.

6.   A remaining problem is that of designing discriminants for areas where available events are essentially limited to either earthquake or explosion populations.

REFERENCES

Anderson, T. W. (1958). Introduction to multivariate statistical analysis, Wiley, New York.

Avsjuk Yu. N., S. I. Alexandrov, A. G. Gamburtsev and S. L. Tsvang (1988). Seismic Monitoring of the Earth's crust, Journal of Geodynamics, 10, 345-354.

Azen, S. P., L. Breiman and W. S. Meisel (1975). Modern approaches to data analysis. Course Notes. Technology Service Corporation, Santa Monica, CA.

Bannister, S. C., E. S. Husebye and B. O. Ruud (1990). Location of topographic P-to-Rg Scattering near the NORESS array. Bull. Seis. Soc. Am. vol. 80, No 6, 1969-1986.

Baumgardt, D. R. (1990). Investigation of teleseismic Lg blockage and scattering using regional arrays, Bull. Seism. Soc. Am., 80, 2261-2281.

Baumgardt, D. R. and G. B. Young (1990). Regional seismic waveform discriminants and case-based identification using regional arrays, Bull. Seism. Soc. Am. 80, 1874-1892.

Birtill, J.W. and F.E. Whiteway (1965). The application of phased arrays to the analysis of seismic body waves, Phil. Trans. Roy. Soc., Series A, 258, 421-493.

Blandford, R. R. (1982). Seismic event discrimination, Bull. Seism. Soc. Am., 72, S69-S88.

Bolt, B. A. (1976). Nuclear Explosions and Earthquakes; The Parted Veil. W. H. Freeman, San Francisco, 309 pp.

Dahlman, O. and H. Israelson (1977). Monitoring of Underground Nuclear Explosions. Elsevier, New York, 440 pp.

Dainty, A. M. (1990). Studies of coda using array and three-component processing, PAGEOPH, 132, 221-244.

Dainty A. M. and M. N. Toksoz (1990). Array analysis of seismic scattering. Bull.Seis.Soc.Am. 80, 2242-2260.

136

Deev, A. D. (1970). Representation of statistics of discrete analysis and asymptotic expansion for space dimension comparable with sample size, Dokl. Akad. Nauk , v.195, N 4, USSR, 759-762.

Douglas, A. (1981). Seismic source identification: A review of past and present research efforts. E.S. Husebye & S. Mykkeltveit (eds.), D. Reidel Publ. Co., The Netherlands.

Dowla, F., S. Taylor and R. Anderson (1990). Seismic discrimination with artifical neural networks preliminary results with regional spectral data, Bull. Seism. Soc. Am. 80, 1346-1373.

Dysart, P. S. and J. J. Pulli (1990). Regional seismic event classification at the NORESS array: seismological measurements and the use of trained neural networks, Bull. Seism. Soc. Am. 80, 1910-1933.

Evernden, J. F. (1977). Spectral characteristics of the P codas of Eurasian earthquakes and explosions, Bull. Seism. Soc. Am., 67, 1153-1171.

Evernden, J. F. and W. M. Kohler (1979). Further study of spectral composition of P codas of earthquakes and explosions, Bull. Seism. Soc. Am., 69, 483-511.

Evernden, J. F., C. B. Archambeau and E. Cranswick (1986). An evaluation of seismic decoupling and underground nuclear test monitoring using high-frequency data, Rev. Geophys., 24, 143-215.

Gel'fand, I. M., Sh. A. Guberman, V. I. Keilis-Borok et al. (1976). Source conditions of strong earthquakes (California and other regions). In Studies of seismicity and models of the Earth, Moscow, Nayka, 3-91.

Husebye, E. S. and S. Mykkeltveit, eds. (1981). Identification of Seismic Sources -- Earthquakes or Underground Explosions, NATO ASI Series, D. Reidel Publ. Co., Dordrecht, The Netherlands, 876 pp.

137

Husebye, E.S. and B.O. Ruud (1989). Array seismology -- Past, present and future developments, in: Observatory Seismology, J.J. Liteheiser (ed)., Berkeley Univ. Press, Berkeley, California, 123-153.

Ingate, S. F., E. S. Husebye and A. Christoffersson (1985). Regional arrays and optimum data processing schemes, Bull. Seism. Soc. Am., 75, 1155-1177.

Kerr, A. U., ed. (1985). The VELA Program. Twenty-five Years of Basic Research. Executive Graphic Services. Defense Advanced Research Projects Agency (DARPA), Rosslyn, VA, 964 pp.

King, D. W. and G. Calcagnile (1976). P-wave velocities in the upper mantle beneath Fennoscandia and western Russia. Geophys. J., 46, 407-432.

Kushnir, A. F., E. V. Troitskiy and S. L. Tsvang (1986). Dependence of the probability of recognition errors of the size of the sample being classified, Computational Seismology, Allerton Press, Inc., 19, 77-82.

Kushnir, A. F., V. M. Lapshin, V. I. Pinsky, and J. Fyen (1990). Statistically optimal event detection using small array data, Bull. Seism. Soc. Am. 80, 1934-1950.

Levin, B. R. and E. V. Troitskii (1970). Total probability of error in classification of normal populations differing in vectors of the means, Avtomatika and Telemekhanika N 1, 54-56.

Marshall, P. D. and A. Douglas (1985). Earthquakes and explosions: Teleseismic Monitoring. Where are we now?, 633-657, in The VELA Program. Twenty-five year review of basic research. Ann U. Kerr editor, DARPA.

Pisarenko, V. I., A. F. Kushnir, F. M. Pruchkina and S. L. Tsvang (1981). Linear discrimination for samples of limited size, In E. S. Husebye and S. Mykkeltveit, eds., Identification of Seismic Sources-Earthquakes or Underground Explosions, D. Reidel, Dodrecht, the Netherlands, 741-745.

Pisarenko, V. F., A. F. Kushnir, F. M. Pruchkina, E. V. Troitskiy and S. L. Tsvang (1983). Estimation of the probability of errors in problems of classifying geophysical observations, Computational Seismology, Allerton Press,Inc., 15, 143-154.

Pomeroy, P. W., W. J. Best and T. V. McEvilly (1982). Test ban treaty verification with regional data-a review, Bull. Seism. Soc. Am. 72, S89-S129.

Press, F., ed. (1985). Nuclear Arms Control: Background and Issues, National Academy Press, Washington, D.C., 378 pp.

Raudis, Sh. Yu. and V. S. Pikyalis (1975). Tabulation of the expected classification error of a linear discriminant function as afunction of the training sample, In: Statistical problems of control, Institute Fiziki i Matematiki AN LitSSR, Vilnnius, N 11, 81-120 (in Russian).

Ringdal, F. (1990). Teleseismic event detection using the NORESS array, with special reference to low-yield Semipalatinsk explosions, Bull. Seism. Soc. Am. 80, 2127-2142.

Sandvin, O. and D. Tjøstheim (1978). Multivariate autoregressive representation of seismic P-wave signals with application to short-period discrimination, Bull. Seism. Soc. Am. 68, N3, 735-756.

Sereno, T. J. (1991). Simulation of the detection and location capability of regional seismic networks in the Soviet Union, SAIC Rep. 91/1061.

Su, F., K. Aki and N. N. Biswas (1991). Discriminating quarry blasts from earthquakes using coda waves, Bull. Seism. Soc. Am. 81, 162-168.

Taylor, S. R. and P. D. Marshall (1991). Spectral discrimination between Soviet explosions and earthquakes using short-period array data, Geophys. J. Int., 106, 265-273.

Tjøstheim, D. (1975). Autoregressive representation of seismic P-wave signals with an application to the problem of short-period discriminants, Geophys. J. R. astr. Soc. 43, 269-291.

139

Tjøstheim, D. (1978). Improved seismic discrimination using pattern recognition, Phys. Earth Planet. Int., 16, 85-108.

Tjøstheim, D. (1981). Multidimensional discrimination techniques -- theory and application. In E.S. Husebye and S. Mykkeltveit, eds., Identification of Seismic Sources-Earthquakes or Underground Explosions, D. Reidel, Dodrecht, the Netherlands, 663-694.

Tjøstheim, D. and E. S. Husebye (1976). An improved discriminant for Test ban verification using short and long period spectral parameters, Geophys. Research Letters 3, N 8, 499-502.

Tsipis, K., D. W. Hafemeister and P. Janeway, eds. (1986). Arms Control Verification, Pergamon Brassey's, Washington, 416 pp.

Tsvang, S. L. (1986). Seismic monitoring wave field parameters statistical classifications algorithms, in Earth Crust Seismic Monitoring, 262-266, Moscow, USSR (in russian), 262-266.

Tsvang, S. L., A. F. Kushnir, S. P. Starodubrovskaya, N. G. Gamburtseva, I. A. Ravich (1986). Statistical Analysis of Wave Tails in Seismic Sounding, Izvestia,Earth Physics, 22, 7, 540-552.

Vergino, E S. (1989a). Soviet test yields, EOS 70, No. 48, 1511.

Vergino, E. S. (1989b). Soviet test yields, Corrections and additions, EOS 70, No. 52, 1569.

Weber K., A. D. Gvishiani, P. Gaudefrois, A. I. Gorshkov, A. F. Kushnir, V. F. Pisarenko, A, V, V. Trusov, M. L. Tsvang and S. L. Tsvang (1986). Classification of high-seismicity Zones in the Western Alps, Izvestia,Earth Physics, 22, 12, 965-976.

TABLE 1

Presumed Explosions

No	Date	Region	Lat.	Lon.	Mb	Ms
1	1984 12 28	East.Kaz. (5)	49.86	78.75	6.0	4.1
2	1985 02 10	East.Kaz. (5)	49.87	78.81	5.9	4.4
3	1985 04 25	East.Kaz. (5)	49.92	78.97	5.9	5.2
4	1985 06 30	East.Kaz. (5)	49.86	78.69	6.0	4.2
5	1985 07 11	East.Kaz. (5)	49.90	78.80	3.5	---
6	1985 07 18	West.Russia (7)	65.97	40.86	5.0	3.7
7	1985 07 25	East.Kaz. (5)	49.89	78.15	5.0	4.0
8	1988 09 14	East.Kaz. (5)	49.82	78.79	6.1	4.6
9	1988 11 12	East.Kaz. (5)	50.05	78.99	5.2	---
10	1988 11 23	East.Kaz. (5)	49.78	78.14	5.3	---
11	1987 02 26	East.Kaz. (5)	49.81	78.16	5.4	---
12	1987 03 12	East.Kaz. (5)	49.93	78.78	5.4	3.9
13	1987 04 03	East.Kaz. (5)	49.90	78.80	6.2	4.7
14	1987 04 17	East.Kaz. (5)	49.85	78.69	6.0	4.3
15	1987 04 19	Ural.Mount. (8)	60.78	56.22	4.5	---
16	1987 05 06	East.Kaz. (5)	49.77	78.09	5.5	---
17	1987 06 05	S.Sinkiang (6)	41.58	88.75	6.3	4.4
18	1987 06 06	East.Kaz. (5)	49.86	78.14	5.4	---
19	1987 07 06	Cent.Siberia (3)	61.49	112.78	5.2	---
20	1987 07 17	East.Kaz. (5)	49.78	78.12	5.8	4.5
21	1987 07 24	Cent.Siberia (3)	61.46	112.72	5.1	---
22	1987 08 02	East.Kaz. (5)	49.84	78.88	5.9	3.8
23	1987 08 02	N.Zealya (1)	73.31	54.71	5.8	3.4
24	1987 08 12	Cent.Siberia (3)	61.42	112.71	5.0	---
25	1987 10 03	West.Kaz. (4)	47.63	56.21	5.2	---
26	1987 10 16	East.Kaz. (5)	49.78	78.24	4.6	---
27	1987 11 15	East.Kaz. (5)	49.87	78.79	6.0	4.8
28	1987 12 13	East.Kaz. (5)	49.95	78.85	6.1	4.5
29	1987 12 20	East.Kaz. (5)	49.75	78.02	4.8	---
30	1987 12 27	East.Kaz. (5)	49.83	78.74	6.1	4.5
31	1988 02 06	East.Kaz. (5)	49.86	77.96	4.8	---
32	1988 02 13	East.Kaz. (5)	49.92	78.90	6.0	4.5
33	1988 04 03	East.Kaz. (5)	49.88	78.96	5.9	---
34	1988 05 04	East.Kaz. (5)	49.91	78.72	6.2	---
35	1988 05 07	N.Zealya (1)	73.35	54.26	5.5	3.8
36	1988 06 14	East.Kaz. (5)	50.02	78.98	4.9	4.1
37	1988 08 22	West.Siberia (2)	66.28	78.55	5.3	---
38	1988 09 29	S.Sinkiang (6)	41.82	88.25	4.8	---
39	1988 10 18	East.Kaz. (5)	49.86	78.12	4.9	---
40	1998 12 04	N.Zealya (1)	73.36	55.07	5.9	---
41	1989 12 17	East.Kaz. (5)	49.88	78.92	5.9	4.5
42	1989 02 12	East.Kaz. (5)	49.89	78.75	5.9	4.4
43	1989 02 17	East.Kaz. (5)	49.87	78.12	5.0	---
44	1989 22 03	East.Kaz. (5)	49.91	78.86	6.0	4.5

Table 1. Listing of the presumed underground nuclear explosions (NE) recorded at NORESS and used in our analysis. The region numbers (in brackets) refer to the specific USSR test sites shown in Fig 1. The focal parameters are taken from the PDE and ISC bulletins. Note, Event 11 (Ural Mountains) is the second explosion on 19 April with origin time at 04.04.55.6. The list is incomplete as NORESS data from 5 presumed NEs for various technical reasons were not available to us. The events are: 15 Jun 1985 (48.89N, 78.88E), 7 Nov 1985 (49.95N, 78.83E), 19 Apr 1987 (60.67N, 56.30E), 20 Jun 1987 (49.90N, 78.73E) and 6 Sep 1988 (61.22N, 48.04E). Another "lost" event, possibly an NE, is that of 18 Sep 1987 (50.18N, 78.02E).

TABLE 2

Presumed Earthquakes.

No	Date	Lat.	Lon.	Depth	Mb	Ms
1	1984 11 02	42.00	84.06	33	4.5	---
2	1985 02 03	42.06	84.34	-	4.5	---
3	1985 03 24	42.06	77.62	3	4.3	---
4	1985 04 16	42.26	82.24	33(3)	4.5	---
5	1985 06 02	43.80	85.65	21(45)	4.9	4.2
6	1985 07 16	42.22	82.36	45(22)	4.9	4.2
7	1985 08 14	42.13	82.44	33	4.1	---
8	1985 08 23	42.65	74.50	3	4.3	---
9	1986 05 30	43.23	87.82	33	4.6	---
10	1986 06 12	43.67	87.33	33	4.8	---
11	1986 07 03	43.91	84.69	33	4.4	---
12	1986 07 17	43.32	77.85	33	4.5	---
13	1986 07 21	44.66	79.50	33	4.6	---
14	1986 07 24	43.79	87.25	33	4.5	---
15	1986 10 04	42.39	84.63	33	4.0	---
16	1986 11 20	42.04	84.39	50	4.6	---
17	1986 12 14	47.31	83.31	33	5.0	---
18	1987 04 04	42.45	79.95	33	4.1	4.1
19	1987 05 10	44.28	79.74	33	4.5	---
20	1987 05 26	42.92	78.06	20	4.6	---
21	1987 08 22	43.81	85.29	58	4.4	---
22	1987 09 18	47.01	89.65	33	5.3	4.8
23	1987 09 20	42.91	77.61	41	4.6	4.2
24	1987 10 06	43.43	98.54	32	4.8	4.0
25	1987 10 16	44.20	82.84	56	4.7	---
26	1988 02 08	43.73	83.76	10	4.3	---
27	1988 03 13	42.18	75.44	33	4.5	---
28	1988 03 15	42.21	75.50	33	4.5	---
29	1988 03 25	44.70	79.60	33	4.5	---
30	1988 05 25	42.01	85.69	22	5.2	---
31	1988 06 17	42.97	77.50	24	5.3	5.3
32	1988 09 27	46.80	73.59	5	4.3	---
33	1988 11 15	42.01	89.29	33	5.0	4.3
34	1989 03 05	42.51	74.63	33	5.3	4.1
35	1989 05 08	44.83	79.92	33	4.7	---

Table 2. Listing of presumed earthquakes recorded at NORESS and used in analysis. Focal parameters are taken from ISC and PDE. The numbers in brackets correspond to PDE depths when different from ISC. The choice of this EQ region (insert in Fig. 1) reflects the fact that only 2 test sites in Eurasia, that is, Semipalatinsk and S. Sinkiang, are reasonably close to areas of high seismicity. The list is incomplete as NORESS recordings from 14 presumed earthquakes were not available to us for various technical reasons.

TABLE 3.

DISCRIMINATION RESULTS

Case	Data	Populations	Class. errors Reclass. J.knife		Class. features	Misclass. events	Marginal events
1	BEAM	All events	7	9	All	NE:6,25,26,35, 37,38; EQ:5,13,18;	NE:15; EQ:22,23,35;
2	BEAM	All events	3	7	1,19,3,13	NE:6,23,26,35, 37,38; EQ:23;	NE:5,40; EQ:13,31;
3	BEAM	All EQ Kazakh NE	1	3	19,13	NE:26; EQ:22,32;	EQ:23;
4	OGF	All events	5	8	All	NE:5,6,22,23 37,38; EQ:17,32;	NE:25; EQ:13,22,23;
5	OGF	All events	3	5	19,10,15, 13	NE:6,26,28 EQ:17,32	NE:23;
6	OGF	All EQ Kazakh NE	0	0	19,10	--	NE:5,29,34; EQ:13,32;

Table 3. Discrimination results for the Eurasian events listed in Tables 1 and 2, and recorded at the NORESS array. Classification features are extracted from ordinary beam (BEAM) traces and optimum group filtered (OGF) traces, where coherent noise has been suppressed. The explosion (NE) population was divided in two parts: all explosions or only those at the E. Kazakh test site (see Fig. 1). Classification (class.) errors are given for two cases: Reclassification where the event tested was part of the learning population and Jack-knife, where test event and learning population were independent. The "Reclass." results are always somewhat optimistic. Classification features are detailed in Fig. 3. Misclassified events and Marginal events refer to the numbering in Table 1 and 2. The most problematic event is EQ 32, that is, a presumed earthquake of 27 Sep 1988 (46.80N, 783.59E), which also has a visual appearance of being an explosion. Waveforms for a representative number of events being either misclassified or rated marginal are shown in Fig. 9.
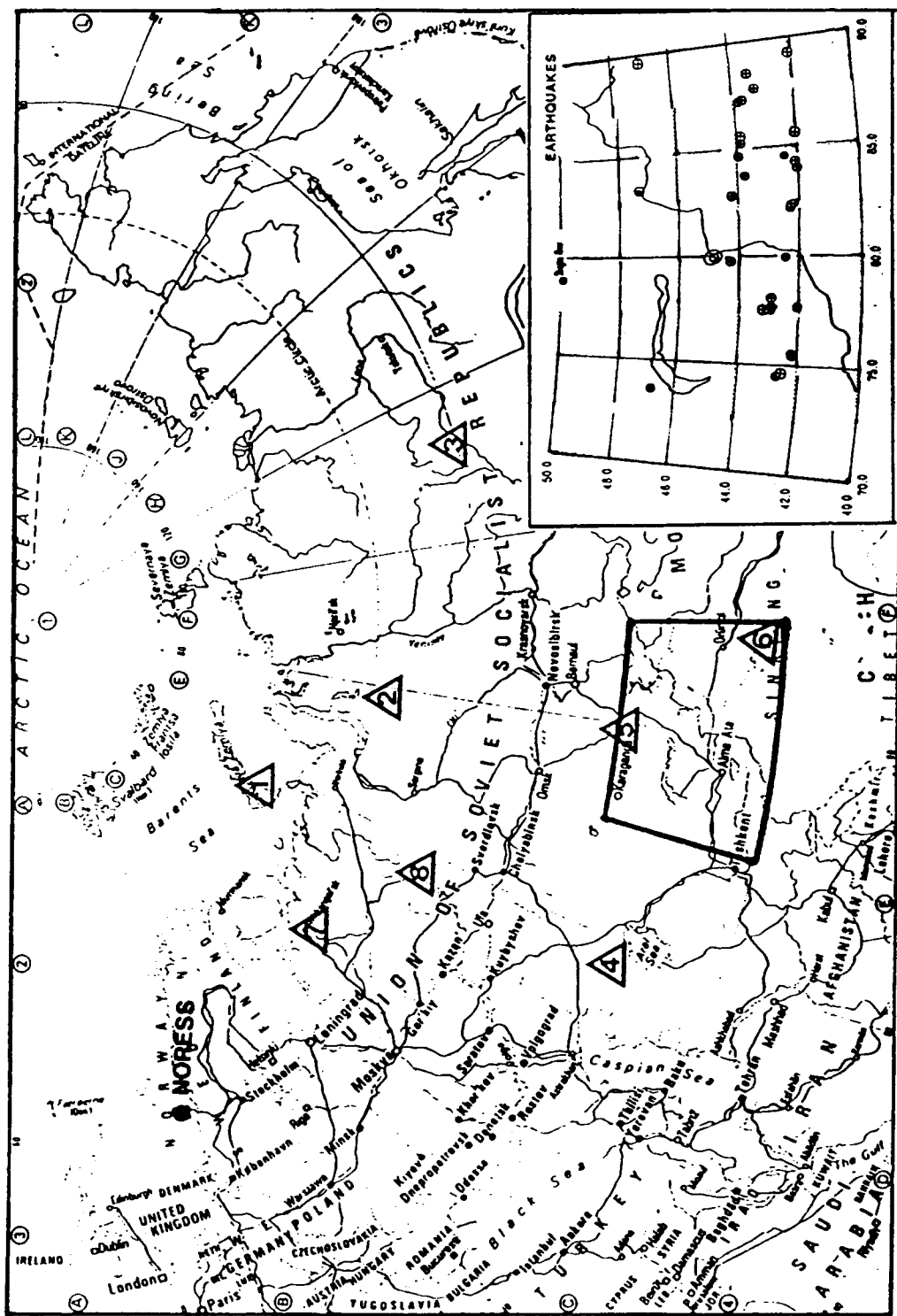
Fig. 1. Map outlining presumed explosion sites and presumed earthquake epicenters used in this classification study. The test sites arc N. Zemlya (1); W. Siberia (2); Cent. Siberia (3); W. Kazakh (4); E. Kazakh (5); S. Sinkiang (6); W. Russia (7); and Ural Mountains (8). Focal parameter details in Tables 1 and 2.
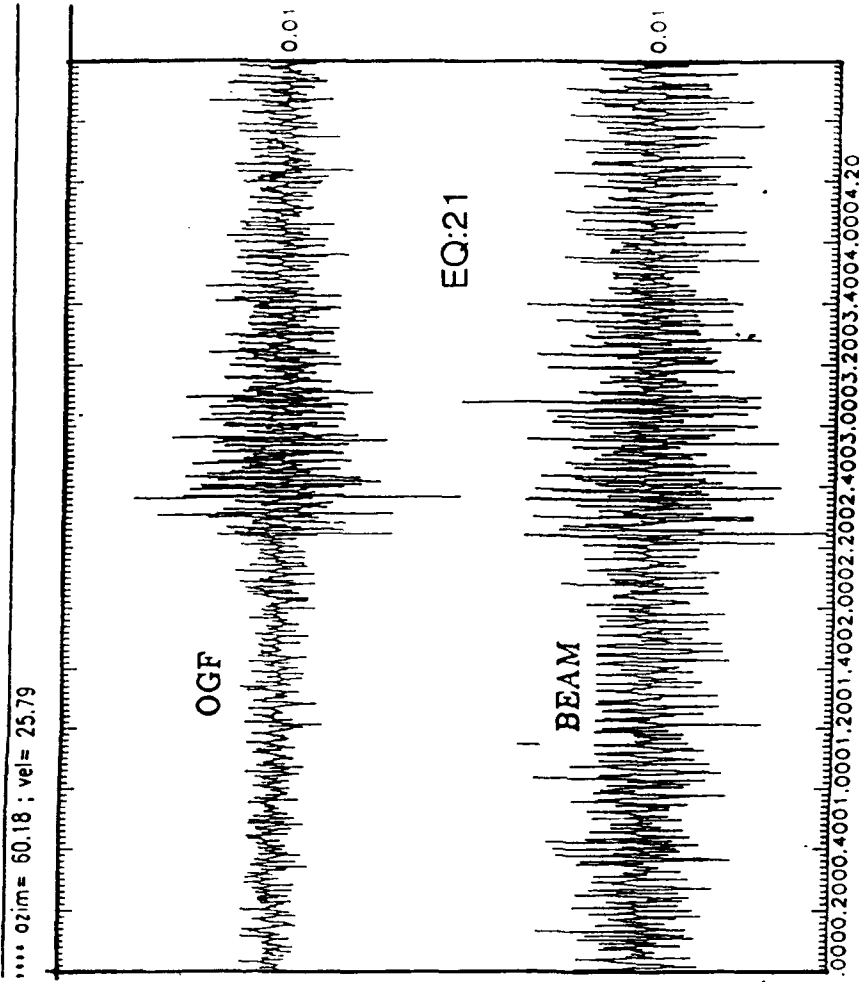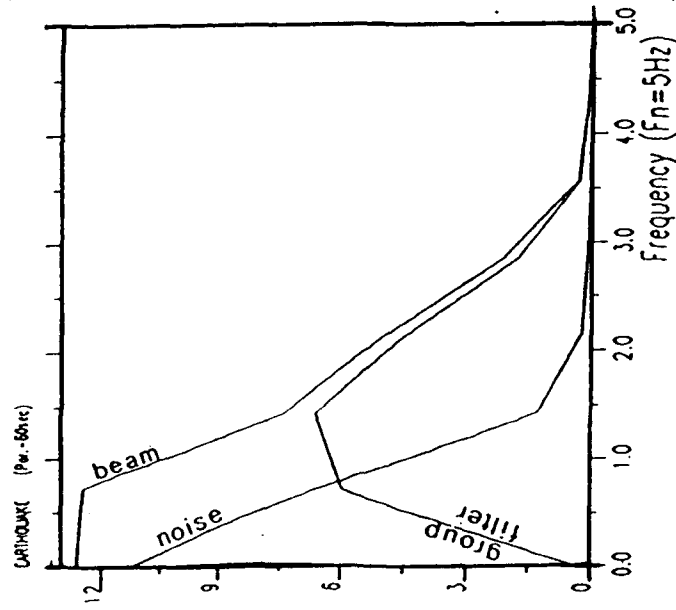
144

Fig. 2. Example of the relative efficiency of the Optimum Group Filtering (OGF) scheme of Kushnir et al (1990) relative to conventional array beamforming. The OGF filter suppresses most of the low frequency coherent noise as clearly seen in the OGF and BEAM traces to the left. The event analyzed here is an earthquake -- no. 21 in Table 2.

PARAMETERS

P-phase (6 sec.)

parameters number	1	2	3	4	5	6	7	8
parameters value(Hz)	0.2-0.8	0.8-1.4	1.4-2.0	2.0-2.6	2.6-3.2	3.2-3.8	3.8-4.4	4.4-5.0
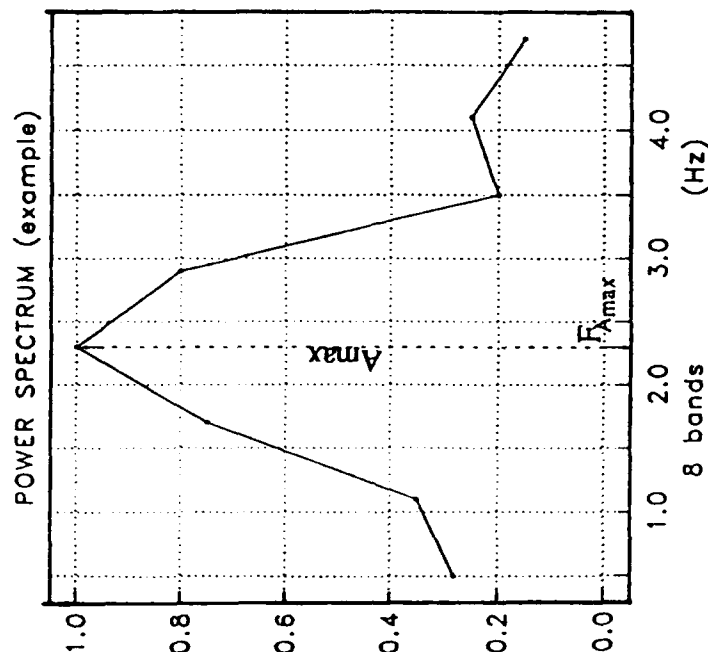
P-coda (30 sec.)

9	10	11	12	13	14	15	16
0.2-0.8	0.8-1.4	1.4-2.0	2.0-2.6	2.6-3.2	3.2-3.8	3.8-4.4	4.4-5.0

17	18	19
F_{Amax} (P-phase)	F_{Amax} (P-coda)	Amax(P)/Amax(coda)

POWER SPECTRUM (example)

Fig. 3. The 19 feature parameters used in this classification study. Center frequencies of the spectral bands used are shown to the left. Note, all spectral band values were normalized for each event with respect to Amax. In the calculation, the logarithmic feaure values were used.

146

P-spectra

44 explosions
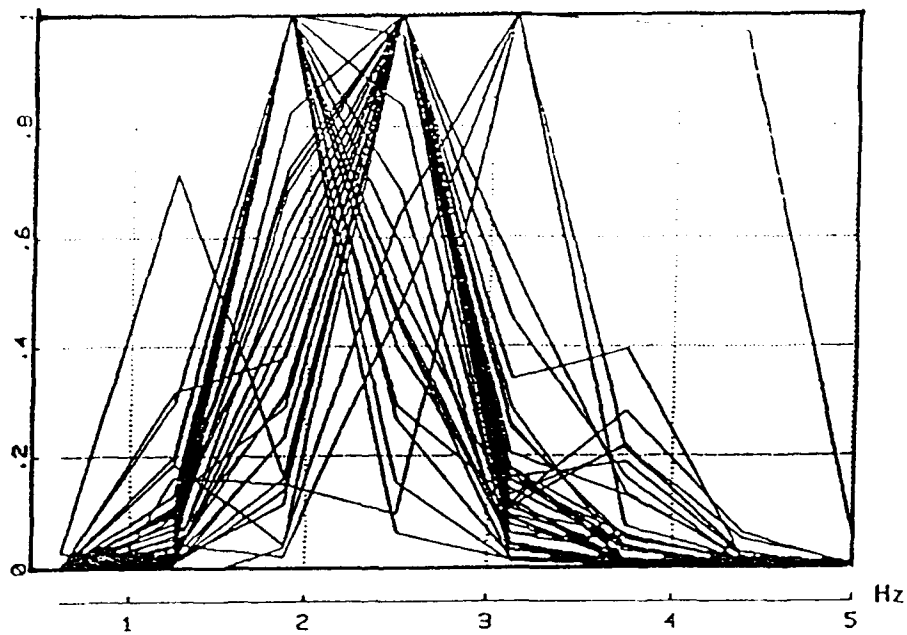
35 earthquakes
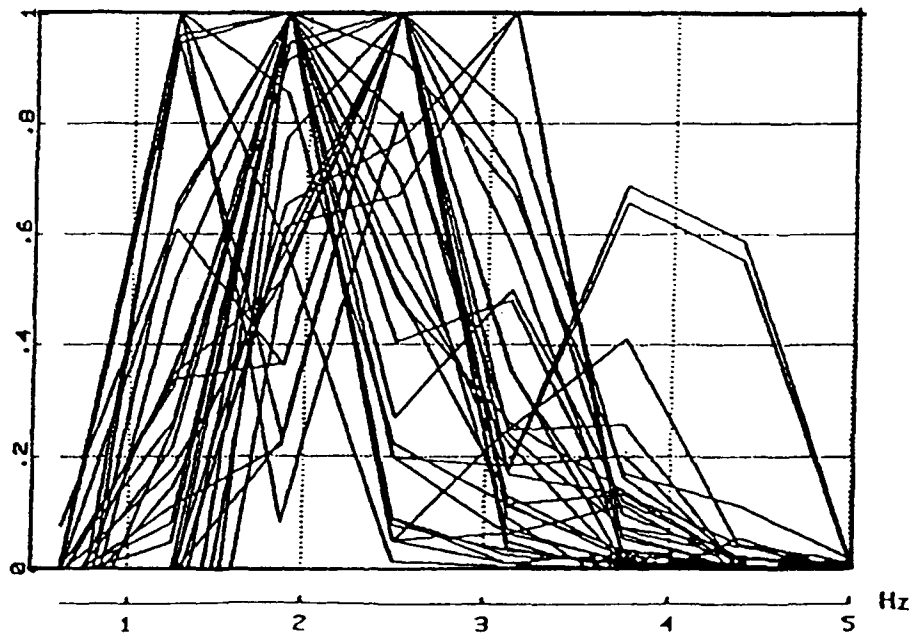
Fig. 4. Normalize power spectra (signal-noise) for all events used in analysis (Table 1 and 2). "Peaks" correspond to the center frequency of the eight spectral bands shown in Fig. 2. Seemingly, the largest spectral differences between the explosion and earthquake populations are in the range 0.5 - 1.5 Hz.
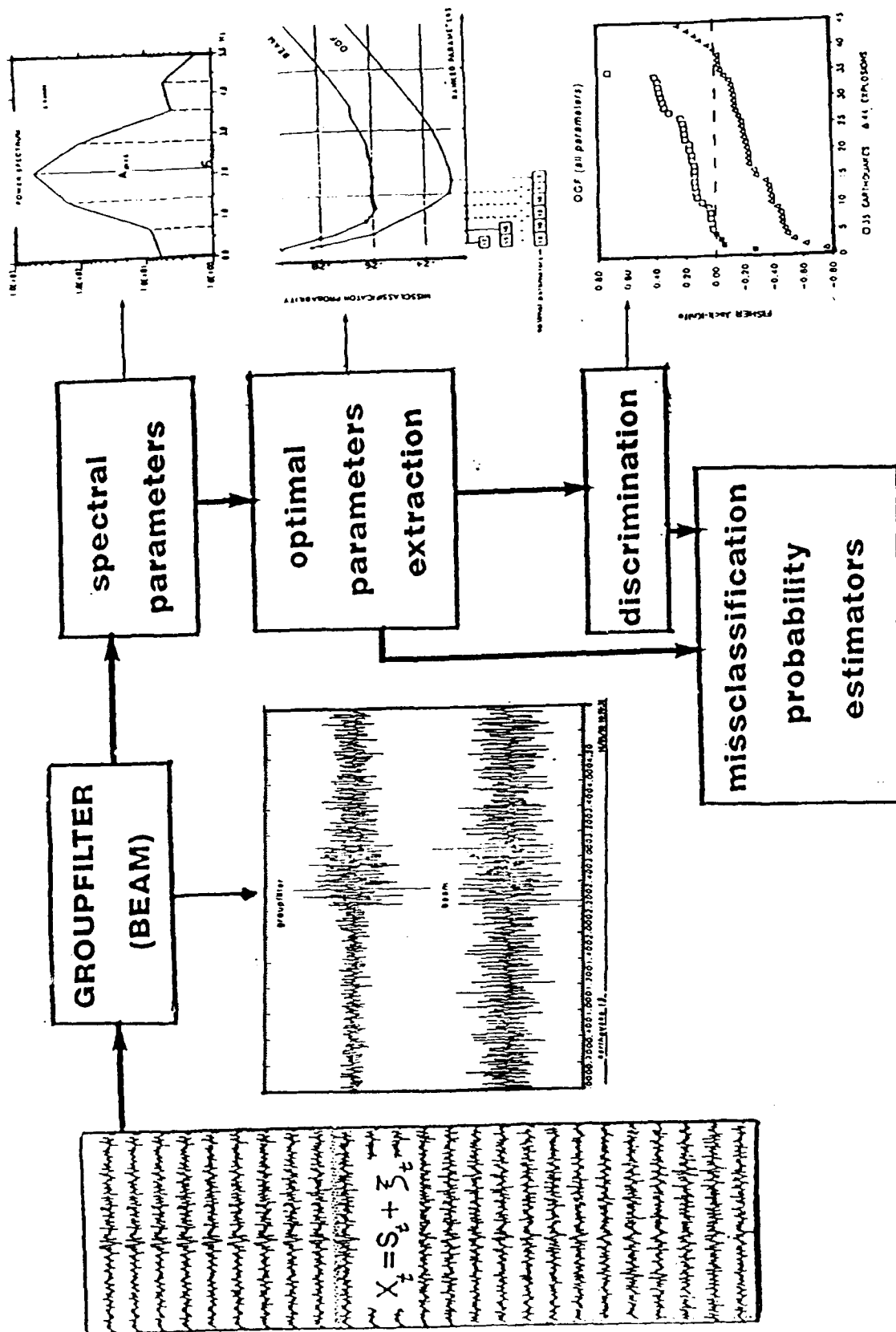
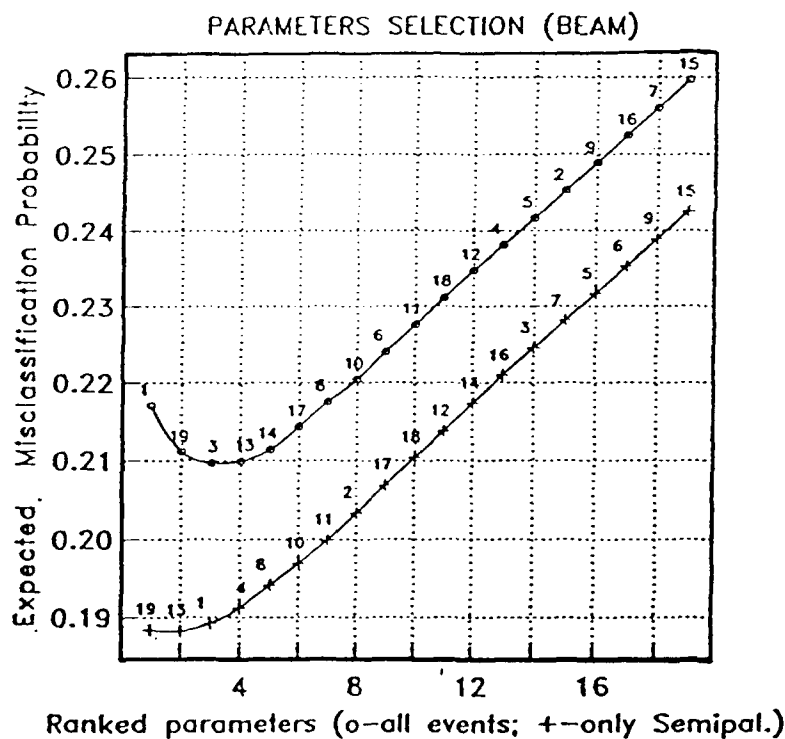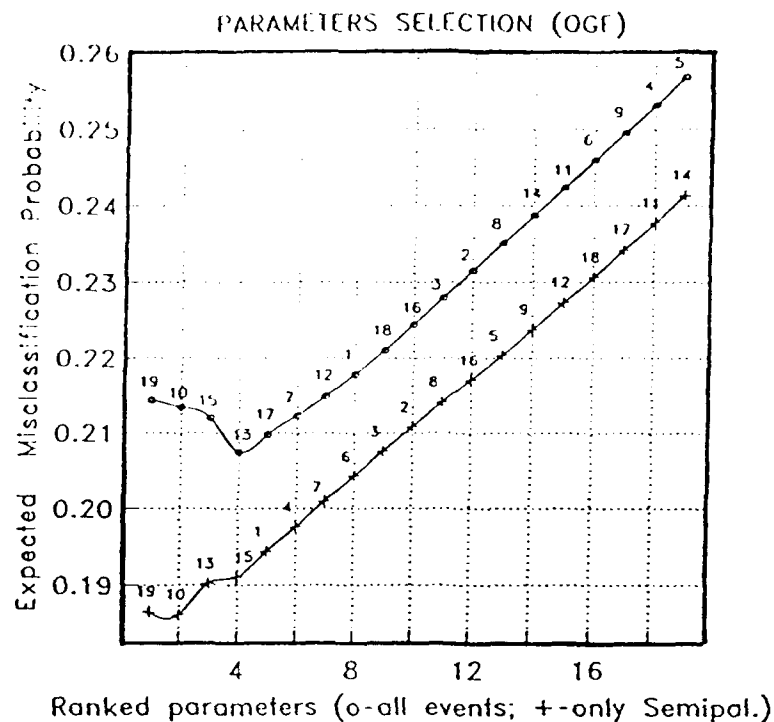Fig. 5. Schematic illustration of the event classification procedure used. Further details in the text.

Fig. 6. The relative performance of feature parameters and combinations hereof as a function of the Expected Probability of Misclassification (EPMC) as defined in the text. OGF refers to optimum group filtered traces (removal of coherent noise), while BEAM refers to ordinary beam traces. Also, the upper curves refer to all events, while the lower ones refer to the subset of the Semipalatinsk or E. Kazakh test site explosions (Fig. 1). The minimum in the EPMC parameter implies that a combination of 2 or 4 classification features is optimum, as inclusion of additional feature parameters actually decreases the performance as discussed in the text.
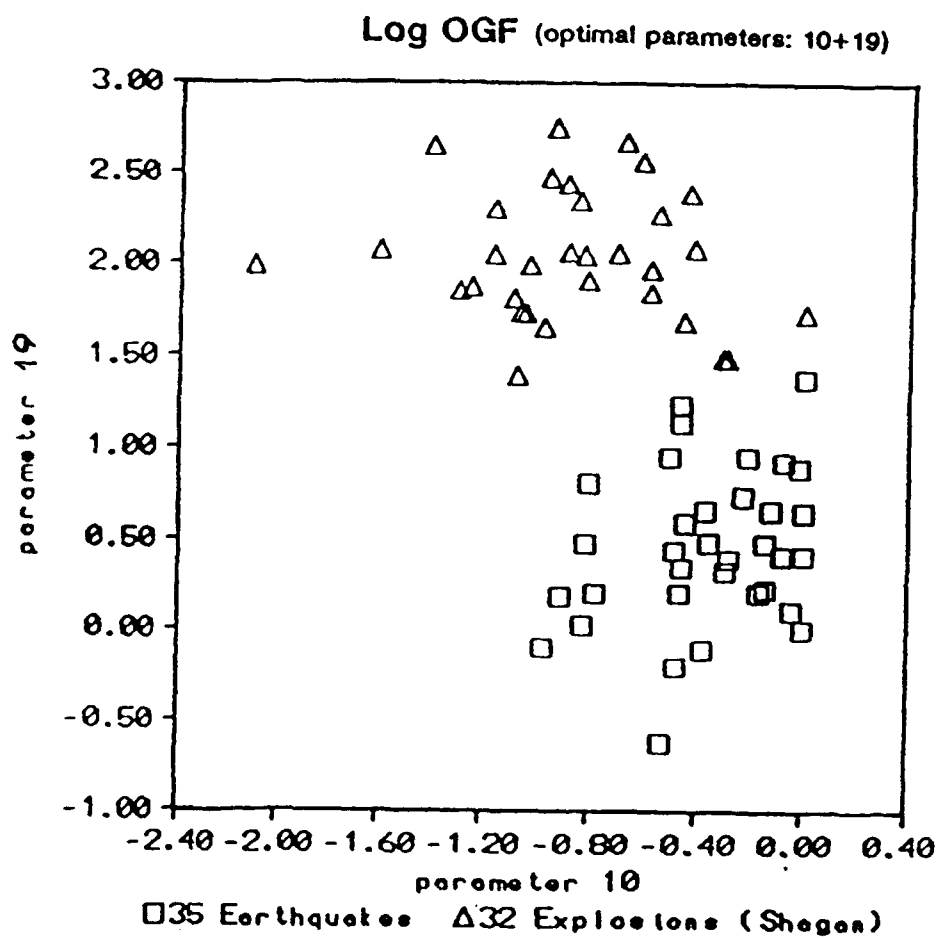
Fig. 7. Diagram for the feature parameters 10 and 19 as calculated from OGF traces for all earthquakes (Table 2), but the explosion population was limited to the E. Kazakh test site (Table 1). The two event populations are well separated, but a better display is given in Fig. 8b, while Case 6 in Table 3 actually details marginal events.

BEAM DISCRIMINATION

35EQ+44NE, all parameters

35EQ+44NE, optimal parameters (1,19,3,13)

Only E.Kazach (32NE+35EQ), optimal parameters (19,13)

Events number ranked due to LDF values

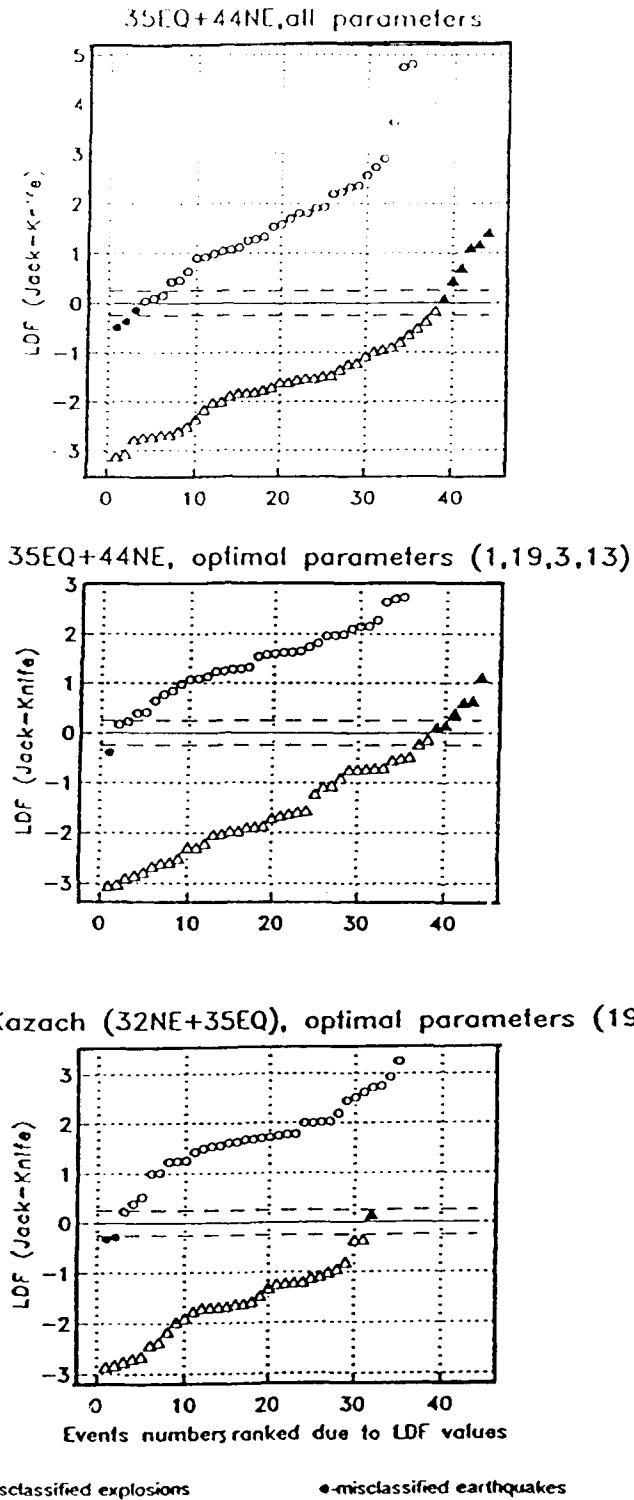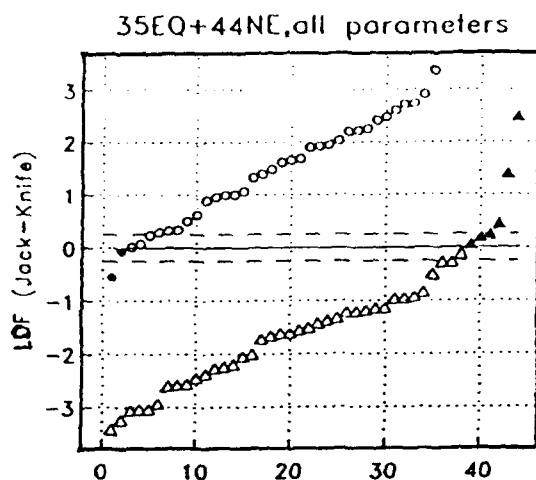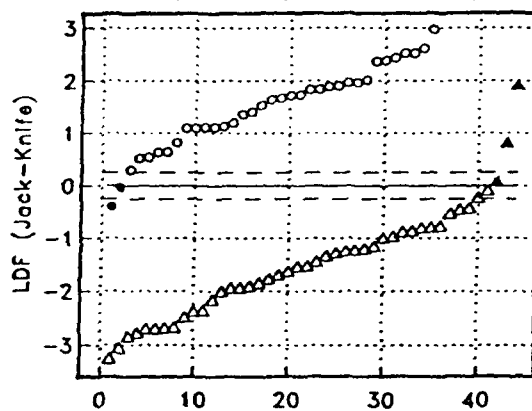▲ -misclassified explosions   ● -misclassified earthquakes

Fig. 8a. Event discrimination with feature parameters extracted from the conventional beam traces. The LDF (linear discrimination function) is defined in the text and Jack-Knife refers to the specific way of testing individual events independently against the learning population. The events are ranked relative to their LDF values, and thus not the way done in Tables 1 and 2. Events with LDF values within ± 0.2 units (stippled lines) are somewhat arbitrarily defined as marginal events. The 3 combinations of event populations and optimum parameter combinations coincide with Case 1-3 in Table 3.
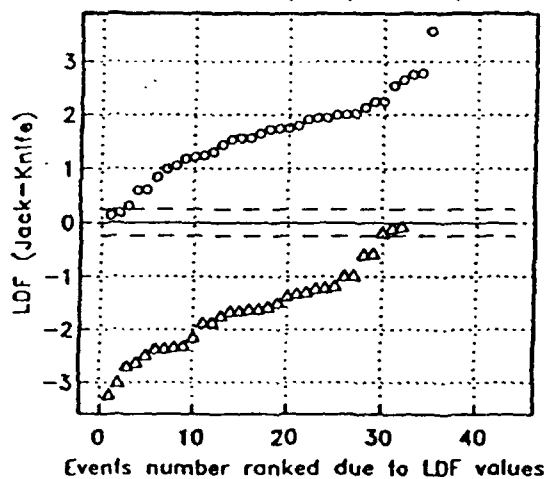
OGF DISCRIMINATION

Fig. 8b. Event discrimination with feature parameters extracted from the OGF traces (optimum group filtered). Caption otherwise as for Fig. 8a.
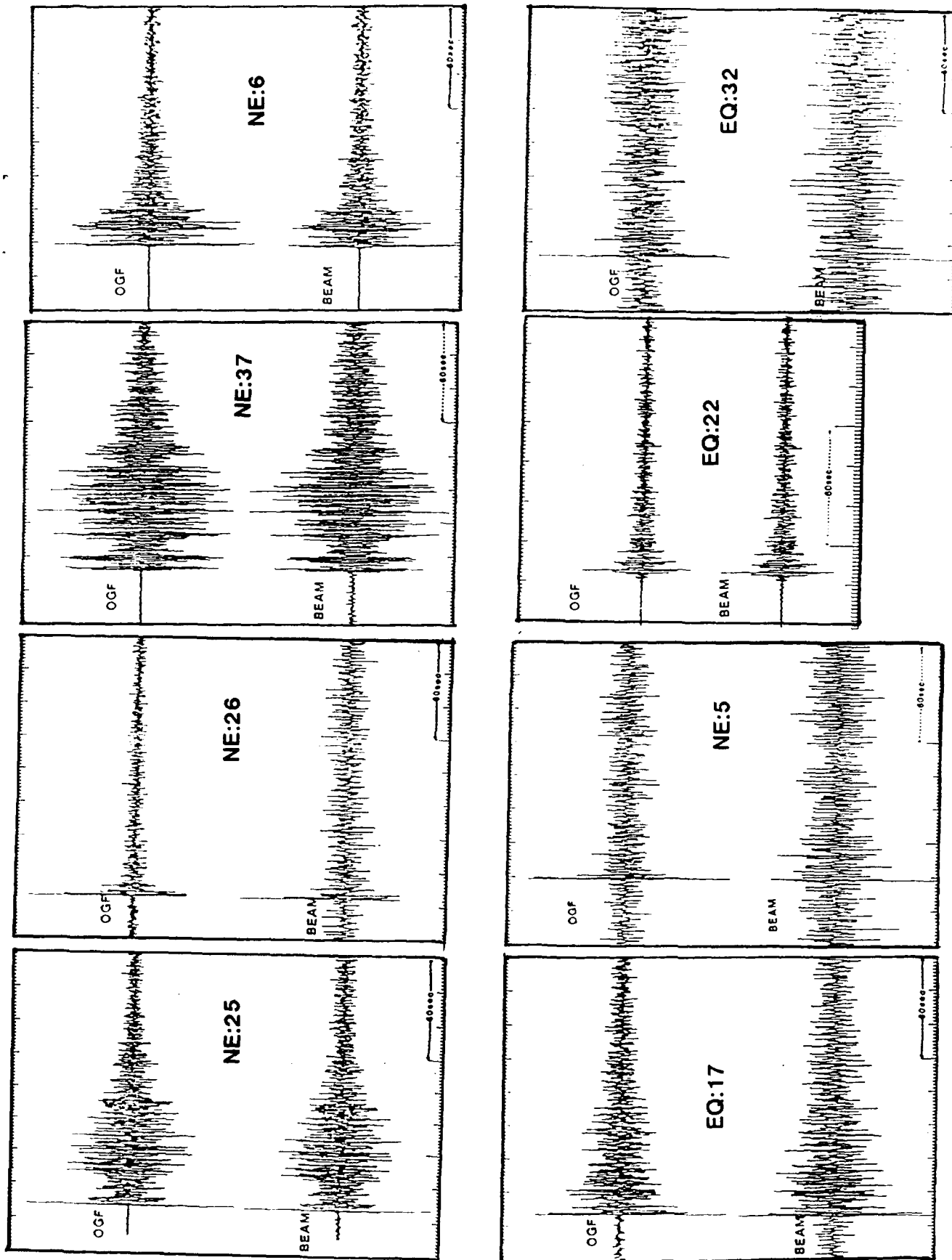
152

Fig. 9. Plot of OGF and conventional beam traces for misclassified and marginal events as listed in Table 3. The focal parameters of the EQ and NE events are shown. Most noticeable here is EQ32 which exhibits the basic feature of an explosion P wave.

153

Prof. Thomas Ahrens
Seismological Lab, 252-21
Division of Geological & Planetary Sciences
California Institute of Technology
Pasadena, CA 91125

Dr. T.J. Bennett
S-CUBED
A Division of Maxwell Laboratories
11800 Sunrise Valley Drive, Suite 1212
Reston, VA 22091

Prof. Keiiti Aki
Center for Earth Sciences
University of Southern California
University Park
Los Angeles, CA 90089-0741

Dr. Robert Blandford
AFTAC/TT, Center for Seismic Studies
1300 North 17th Street
Suite 1450
Arlington, VA 22209-2308

Prof. Shelton Alexander
Geosciences Department
403 Deike Building
The Pennsylvania State University
University Park, PA 16802

Dr. G.A. Bollinger
Department of Geological Sciences
Virginia Polytechnical Institute
21044 Derring Hall
Blacksburg, VA 24061

Dr. Ralph Alewine, III
DARPA/NMRO
3701 North Fairfax Drive
Arlington, VA 22203-1714

Dr. Stephen Bratt
Center for Seismic Studies
1300 North 17th Street
Suite 1450
Arlington, VA 22209-2308

Prof. Charles B. Archambeau
CIRES
University of Colorado
Boulder, CO 80309

Dr. Lawrence Burdick
Woodward-Clyde Consultants
566 El Dorado Street
Pasadena, CA 91109-3245

Dr. Thomas C. Bache, Jr.
Science Applications Int'l Corp.
10260 Campus Point Drive
San Diego, CA 92121 (2 copies)

Dr. Robert Burridge
Schlumberger-Doll Research Center
Old Quarry Road
Ridgefield, CT 06877

Prof. Muawia Barazangi
Institute for the Study of the Continent
Cornell University
Ithaca, NY 14853

Dr. Jerry Carter
Center for Seismic Studies
1300 North 17th Street
Suite 1450
Arlington, VA 22209-2308

Dr. Jeff Barker
Department of Geological Sciences
State University of New York
 at Binghamton
Vestal, NY 13901

Dr. Eric Chael
Division 9241
Sandia Laboratory
Albuquerque, NM 87185

Dr. Douglas R. Baumgardt
ENSCO, Inc
5400 Port Royal Road
Springfield, VA 22151-2388

Prof. Vernon F. Cormier
Department of Geology & Geophysics
U-45, Room 207
University of Connecticut
Storrs, CT 06268

Dr. Susan Beck
Department of Geosciences
Building #77
University of Arizona
Tuscon, AZ 85721

Prof. Steven Day
Department of Geological Sciences
San Diego State University
San Diego, CA 92182

Marvin Denny
U.S. Department of Energy
Office of Arms Control
Washington, DC 20585

Dr. Zoltan Der
ENSCO, Inc.
5400 Port Royal Road
Springfield, VA 22151-2388

Prof. Adam Dziewonski
Hoffman Laboratory, Harvard University
Dept. of Earth Atmos. & Planetary Sciences
20 Oxford Street
Cambridge, MA 02138

Prof. John Ebel
Department of Geology & Geophysics
Boston College
Chestnut Hill, MA 02167

Eric Fielding
SNEE Hall
INSTOC
Cornell University
Ithaca, NY 14853

Dr. Mark D. Fisk
Mission Research Corporation
735 State Street
P.O. Drawer 719
Santa Barbara, CA 93102

Prof Stanley Flatte
Applied Sciences F iilding
University of Calif rnia, Santa Cruz
Santa Cruz, CA 95064

Dr. John Foley
NER-Geo Sciences
1100 Crown Colony Drive
Quincy, MA 02169

Prof. Donald Forsyth
Department of Geological Sciences
Brown University
Providence, RI 02912

Dr. Art Frankel
U.S. Geological Survey
922 National Center
Reston, VA 22092

Dr. Cliff Frolich
Institute of Geophysics
8701 North Mopac
Austin, TX 78759

Dr. Holly Given
IGPP, A-025
Scripps Institute of Oceanography
University of California, San Diego
La Jolla, CA 92093

Dr. Jeffrey W. Given
SAIC
10260 Campus Point Drive
San Diego, CA 92121

Dr. Dale Glover
Defense Intelligence Agency
ATTN: ODT-1B
Washington, DC 20301

Dr. Indra Gupta
Teledyne Geotech
314 Montgomery Street
Alexanderia, VA 22314

Dan N. Hagedon
Pacific Northwest Laboratories
Battelle Boulevard
Richland, WA 99352

Dr. James Hannon
Lawrence Livermore National Laboratory
P.O. Box 808
L-205
Livermore, CA 94550

Dr. Roger Hansen
HQ AFTAC/TTR
Patrick AFB, FL 32925-6001

Prof. David G. Harkrider
Seismological Laboratory
Division of Geological & Planetary Sciences
California Institute of Technology
Pasadena, CA 91125

Prof. Danny Harvey
CIRES
University of Colorado
Boulder, CO 80309

Prof. Donald V. Helmberger
Seismological Laboratory
Division of Geological & Planetary Sciences
California Institute of Technology
Pasadena, CA 91125

Prof. Eugene Herrin
Institute for the Study of Earth and Man
Geophysical Laboratory
Southern Methodist University
Dallas, TX 75275

Prof. Robert B. Herrmann
Department of Earth & Atmospheric Sciences
St. Louis University
St. Louis, MO 63156

Prof. Lane R. Johnson
Seismographic Station
University of California
Berkeley, CA 94720

Prof. Thomas H. Jordan
Department of Earth, Atmospheric &
  Planetary Sciences
Massachusetts Institute of Technology
Cambridge, MA 02139

Prof. Alan Kafka
Department of Geology & Geophysics
Boston College
Chestnut Hill, MA 02167

Robert C. Kemerait
ENSCO, Inc.
445 Pineda Court
Melbourne, FL 32940

Dr. Max Koontz
U.S. Dept. of Energy/DP 5
Forrestal Building
1000 Independence Avenue
Washington, DC 20585

Dr. Richard LaCoss
MIT Lincoln Laboratory, M-200B
P.O. Box 73
Lexington, MA 02173-0073

Dr. Fred K. Lamb
University of Illinois at Urbana-Champaign
Department of Physics
1110 West Green Street
Urbana, IL 61801

Prof. Charles A. Langston
Geosciences Department
403 Deike Building
The Pennsylvania State University
University Park, PA 16802

Jim Lawson, Chief Geophysicist
Oklahoma Geological Survey
Oklahoma Geophysical Observatory
P.O. Box 8
Leonard, OK 74043-0008

Prof. Thorne Lay
Institute of Tectonics
Earth Science Board
University of California, Santa Cruz
Santa Cruz, CA 95064

Dr. William Leith
U.S. Geological Survey
Mail Stop 928
Reston, VA 22092

Mr. James F. Lewkowicz
Phillips Laboratory/GPEH
Hanscom AFB, MA 01731-5000(2 copies)

Mr. Alfred Lieberman
ACDA/VI-OA State Department Building
Room 5726
320-21st Street, NW
Washington, DC 20451

Prof. L. Timothy Long
School of Geophysical Sciences
Georgia Institute of Technology
Atlanta, GA 30332

Dr. Randolph Martin, III
New England Research, Inc.
76 Olcott Drive
White River Junction, VT 05001

Dr. Robert Masse
Denver Federal Building
Box 25046, Mail Stop 967
Denver, CO 80225

Dr. Gary McCartor
Department of Physics
Southern Methodist University
Dallas, TX 75275

Prof. Thomas V. McEvilly
Seismographic Station
University of California
Berkeley, CA 94720

Prof. John A. Orcutt
IGPP, A-025
Scripps Institute of Oceanography
University of California, San Diego
La Jolla, CA 92093

Dr. Art McGarr
U.S. Geological Survey
Mail Stop 977
U.S. Geological Survey
Menlo Park, CA 94025

Prof. Jeffrey Park
Kline Geology Laboratory
P.O. Box 6666
New Haven, CT 06511-8130

Dr. Keith L. McLaughlin
S-CUBED
A Division of Maxwell Laboratory
P.O. Box 1620
La Jolla, CA 92038-1620

Dr. Howard Patton
Lawrence Livermore National Laboratory
L-025
P.O. Box 808
Livermore, CA 94550

Stephen Miller & Dr. Alexander Florence
SRI International
333 Ravenswood Avenue
Box AF 116
Menlo Park, CA 94025-3493

Dr. Frank Pilotte
HQ AFTAC/TT
Patrick AFB, FL 32925-6001

Prof. Bernard Minster
IGPP, A-025
Scripps Institute of Oceanography
University of California, San Diego
La Jolla, CA 92093

Dr. Jay J. Pulli
Radix Systems, Inc.
2 Taft Court, Suite 203
Rockville, MD 20850

Prof. Brian J. Mitchell
Department of Earth & Atmospheric Sciences
St. Louis University
St. Louis, MO 63156

Dr. Robert Reinke
ATTN: FCTVTD
Field Command
Defense Nuclear Agency
Kirtland AFB, NM 87115

Mr. Jack Murphy
S-CUBED
A Division of Maxwell Laboratory
11800 Sunrise Valley Drive, Suite 1212
Reston, VA 22091 (2 Copies)

Prof. Paul G. Richards
Lamont-Doherty Geological Observatory
  of Columbia University
Palisades, NY 10964

Dr. Keith K. Nakanishi
Lawrence Livermore National Laboratory
L-025
P.O. Box 808
Livermore, CA 94550

Mr. Wilmer Rivers
Teledyne Geotech
314 Montgomery Street
Alexandria, VA 22314

Dr. Carl Newton
Los Alamos National Laboratory
P.O. Box 1663
Mail Stop C335, Group ESS-3
Los Alamos, NM 87545

Dr. George Rothe
HQ AFTAC/TTR
Patrick AFB, FL 32925-6001

Dr. Bao Nguyen
HQ AFTAC/TTR
Patrick AFB, FL 32925-6001

Dr. Alan S. Ryall, Jr.
DARPA/NMRO
3701 North Fairfax Drive
Arlington, VA 22209-1714

Dr. Richard Sailor
TASC, Inc.
55 Walkers Brook Drive
Reading, MA 01867

Prof. Charles G. Sammis
Center for Earth Sciences
University of Southern California
University Park
Los Angeles, CA 90089-0741

Prof. Christopher H. Scholz
Lamont-Doherty Geological Observatory
  of Columbia University
Palisades, CA 10964

Dr. Susan Schwartz
Institute of Tectonics
1156 High Street
Santa Cruz, CA 95064

Secretary of the Air Force
(SAFRD)
Washington, DC 20330

Office of the Secretary of Defense
DDR&E
Washington, DC 20330

Thomas J. Sereno, Jr.
Science Application Int'l Corp.
10260 Campus Point Drive
San Diego, CA 92121

Dr. Michael Shore
Defense Nuclear Agency/SPSS
6801 Telegraph Road
Alexandria, VA 22310

Dr. Matthew Sibol
Virginia Tech
Seismological Observatory
4044 Derring Hall
Blacksburg, VA 24061-0420

Prof. David G. Simpson
IRIS, Inc.
1616 North Fort Myer Drive
Suite 1440
Arlington, VA 22209

Donald L. Springer
Lawrence Livermore National Laboratory
L-025
P.O. Box 808
Livermore, CA 94550

Dr. Jeffrey Stevens
S-CUBED
A Division of Maxwell Laboratory
P.O. Box 1620
La Jolla, CA 92038-1620

Lt. Col. Jim Stobie
ATTN: AFOSR/NL
Bolling AFB
Washington, DC 20332-6448

Prof. Brian Stump
Institute for the Study of Earth & Man
Geophysical Laboratory
Southern Methodist University
Dallas, TX 75275

Prof. Jeremiah Sullivan
University of Illinois at Urbana-Champaign
Department of Physics
1110 West Green Street
Urbana, IL 61801

Prof. L. Sykes
Lamont-Doherty Geological Observatory
  of Columbia University
Palisades, NY 10964

Dr. David Taylor
ENSCO, Inc.
445 Pineda Court
Melbourne, FL 32940

Dr. Steven R. Taylor
Los Alamos National Laboratory
P.O. Box 1663
Mail Stop C335
Los Alamos, NM 87545

Prof. Clifford Thurber
University of Wisconsin-Madison
Department of Geology & Geophysics
1215 West Dayton Street
Madison, WS 53706

Prof. M. Nafi Toksoz
Earth Resources Lab
Massachusetts Institute of Technology
42 Carleton Street
Cambridge, MA 02142

5

Dr. Larry Turnbull
CIA-OSWR/NED
Washington, DC 20505

DARPA/RMO/SECURITY OFFICE
3701 North Fairfax Drive
Arlington, VA 22203-1714

Dr. Gregory van der Vink
IRIS, Inc.
1616 North Fort Myer Drive
Suite 1440
Arlington, VA 22209

HQ DNA
ATTN: Technical Library
Washington, DC 20305

Dr. Karl Veith
EG&G
5211 Auth Road
Suite 240
Suitland, MD 20746

Defense Intelligence Agency
Directorate for Scientific & Technical Intelligence
ATTN: DTIB
Washington, DC 20340-6158

Prof. Terry C. Wallace
Department of Geosciences
Building #77
University of Arizona
Tuscon, AZ 85721

Defense Technical Information Center
Cameron Station
Alexandria, VA 22314 (2 Copies)

Dr. Thomas Weaver
Los Alamos National Laboratory
P.O. Box 1663
Mail Stop C335
Los Alamos, NM 87545

TACTEC
Battelle Memorial Institute
505 King Avenue
Columbus, OH 43201 (Final Report)

Dr. William Wortman
Mission Research Corporation
8560 Cinderbed Road
Suite 700
Newington, VA 22122

Phillips Laboratory
ATTN: XPG
Hanscom AFB, MA 01731-5000

Prof. Francis T. Wu
Department of Geological Sciences
State University of New York
 at Binghamton
Vestal, NY 13901

Phillips Laboratory
ATTN: GPE
Hanscom AFB, MA 01731-5000

AFTAC/CA
(STINFO)
Patrick AFB, FL 32925-6001

Phillips Laboratory
ATTN: TSML
Hanscom AFB, MA 01731-5000

DARPA/PM
3701 North Fairfax Drive
Arlington, VA 22203-1714

Phillips Laboratory
ATTN: SUL
Kirtland, NM 87117 (2 copies)

DARPA/RMO/RETRIEVAL
3701 North Fairfax Drive
Arlington, VA 22203-1714

Dr. Michel Bouchon
I.R.I.G.M.-B.P. 68
38402 St. Martin D'Heres
Cedex, FRANCE

Dr. Michel Campillo
Observatoire de Grenoble
I.R.I.G.M.-B.P. 53
38041 Grenoble, FRANCE

Dr. Kin Yip Chun
Geophysics Division
Physics Department
University of Toronto
Ontario, CANADA

Prof. Hans-Peter Harjes
Institute for Geophysic
Ruhr University/Bochum
P.O. Box 102148
4630 Bochum 1, GERMANY

Prof. Eystein Husebye
NTNF/NORSAR
P.O. Box 51
N-2007 Kjeller, NORWAY

David Jepsen
Acting Head, Nuclear Monitoring Section
Bureau of Mineral Resources
Geology and Geophysics
G.P.O. Box 378, Canberra, AUSTRALIA

Ms. Eva Johannisson
Senior Research Officer
National Defense Research Inst.
P.O. Box 27322
S-102 54 Stockholm, SWEDEN

Dr. Peter Marshall
Procurement Executive
Ministry of Defense
Blacknest, Brimpton
Reading FG7-FRS, UNITED KINGDOM

Dr. Bernard Massinon, Dr. Pierre Mechler
Societe Radiomana
27 rue Claude Bernard
75005 Paris, FRANCE (2 Copies)

Dr. Svein Mykkeltveit
NTNT/NORSAR
P.O. Box 51
N-2007 Kjeller, NORWAY (3 Copies)

Prof. Keith Priestley
University of Cambridge
Bullard Labs, Dept. of Earth Sciences
Madingley Rise, Madingley Road
Cambridge CB3 OEZ, ENGLAND

Dr. Jorg Schlittenhardt
Federal Institute for Geosciences & Nat'l Res.
Postfach 510153
D-3000 Hannover 51, GERMANY

Dr. Johannes Schweitzer
Institute of Geophysics
Ruhr University/Bochum
P.O. Box 1102148
4360 Bochum 1, GERMANY